Transitions in Axisymmetric Turbulence

Zecong Qin

To cite this version:

Zecong Qin. Transitions in Axisymmetric Turbulence. Other. Université de Lyon, 2019. English. NNT : 2019LYSEC023 . tel-02421953

Numéro d'ordre NNT : **2019LYSEC23** Année : 2019

THÈSE de DOCTORAT DE L'UNIVERSITÉ DE LYON
OPÉRÉE AU SEIN DE L'ÉCOLE CENTRALE DE LYON

ÉCOLE DOCTORALE No.162 MEGA
Mécanique, Energétique, Génie civil et Acoustique

Spécialité : Mécanique des Fluides

Soutenue publiquement le 19/09/2019 par :

Zecong QIN

Transitions and Structures in Axisymmetric Turbulence

Devant le jury composé de :

ALEXAKIS Alexandros	Chargé de Recherche CNRS	Rapporteur
BOS Wouter	Chargé de Recherche CNRS	Directeur de Thèse
FLÓR Jan-Bert	Directeur de Recherche CNRS	Examinateur
LAVAL Jean-Philippe	Directeur de Recherche CNRS	Rapporteur
LÉVÊQUE Emmanuel	Directeur de Recherche CNRS	Examinateur
NASO Aurore	Chargé de Recherche CNRS	Co-encadrante de Thèse

Acknowledgement

Time passes as happily as a stream glides, and as sadly as a tear slides.
Sadly without any sound, like an autumn leaf falling to kiss the ground.
Kissing the ground for whispers of goodbye, and missing the past at sunsets of sigh.
But sighing does not heal that much, the sorrow that no one else can touch.
Only by you, one touch would suffice, and brightly to me, your smiles are so nice.

—— May I sing these words to all my dear acquaintances in Ecully.

Ancient Chinese philosophy proposes that one does his/her best and let the Heavenly God decide whether he/she should succeed. In this logic, people should work hard first, looking forward to an award from God. There are even famous lyrics of a popular song that go : "Only 30% for God to tell, but up to 70% you should prepare well. Winners are those who dare sail." Regretfully, I always reverse this logic : let God show me first the direction, and then I persuade myself to pack up for this journey. By this trick, I successfully turn the 30 : 70 mechanism into an all-or-nothing story : either someone guides me and then I gain something through hard working, or no one cares about me such that my life remains worthless. Fortunately, I have been kindly treated ever since the beginning of this story.

The story unfolded itself on the afternoon of November 5th, 2015, a common day of my internship before graduating. I was worrying about my future then, right at the moment when my phone rang and wrote that it was my master tutor Mr. FANG Le. By this call, he informed me, in a gentle and friendly tone as always : "There is a chance, should you choose to accept it, to accomplish a Ph.D thesis in Ecole Centrale de Lyon. This chance will not self-destruct in five seconds." "Of course not in five seconds, Sir. But this would be a big event and I need five days to make the decision." answered I, pretending to be cool. And within less than 24 hours I replied : "I'm in, Sir." The rule in this game is quite simple and fair : although it sounded like a mission impossible, once he trusted me, I trusted him. Apart from his trust and promotion for this chance, I am still grateful to him today, even after 6 years, for his earlier patience and guidance during my master thesis, which has turned me from nothing into something. I, something not good at all but was then hoping to be something slightly better, headed to the Laboratoire de Mécanique des Fluides et d'Acoustique in Lyon, France.

It was in LMFA that I have met Mr. QU Bo who regarded me as a little brother. I didn't need to cover my feelings during conversations, and I was used to telling him my confusions varying from scientific topics to daily life issues. He would always give me his points of view and suggestions with no reservation. He suggested me to do two hours' lecture of scientific articles every day, but I failed to carry on ; he suggested that one could be considered to be mentally stable when something or someone quitted his life and he could keep debugging his codes with a cup of coffee the next morning, and I think I have met this criterion : when he finally finished defending his thesis and was about to leave, I accompanied him till the railway station : best wishes, a big hug and the farewell ; then the next morning I continued coding my program with a cup of coffee. Such coffee mornings have been repeated over and over again when my friends graduated one by one. Me and Bo keep in touch until nowadays, and he is still refreshing my knowledge with his.

Of course, more knowledge is given by my PhD directors Mr. Wouter BOS and Mme. Aurore NASO, who have been my reinforcement ever since. Always, they encouraged me when I reported something to them, motivated me when I was down, gave me a hand when something was urgent, *etc.* I will not forget the afternoon of November 22nd, 2018. I was sitting before my desk as if my body had been drained, and Aurore came to me saying : "Ne t'inquiète pas. On a plein d'idées pour interprêter les resultats." She then wrote several statistical quantities to calculate, which really signified something and will be discussed in this thesis. I will also remember the afternoon of December 20th, 2018. I was sitting at my desk and feeling myself like a salted fish, and Wouter came to me with a pen and pieces of papers as usual : "J'ai des idées.". He first wrote some equations that I knew by heart but had no idea to deal with ; then he made some hypotheses that I doubted whether they made sense ; and here came the initial version of our dynamic model. Although I'm not Christian, but I think that I owe a lot to the goodness of God. Yes, God is fair. When he closes one window of yours, he will send you two directors. And I'd like to say : "LMFA, where amazing happens."

Another amazing experience in LMFA should be attributed to the friendship with Miss ZHU Ying. Today, if she still achieves or discovers something by her excellence, I would clap hands with no excitement, because this is what has happened routinely since the day that I knew her : she never stops evolving for seeking the truth. As commented by a professor, she is strong. It was by her generous instruction that I began to learn touch-typing, to do e-readings, to overcome my weakness, and to accept me myself as an ordinary person. Meanwhile, I have turned myself from something into someone, such that I am not only mentally stable, but have also mentally grown up. To me, she is an almighty elder sister.

However, I have another two fake family members in this story — Mr. CUI Xiaopeng and Mr. WU Jianzhao, the alleged "uncle CUI" and "big brother" — with whom I could share my deep-dark-fantastic cuisine, tricky ironies, trash talks, negative emotions, *etc.* They were the guys such that we wouldn't feel embarrassed even if we just sat there for hours without a single word. They did have been the medicine to my delicate emotion. And they were the first that I would turn to when I was in need of help. I hope that this fake familyhood can be maintained such that someday that I can do something for them in return. Of course, the best wishes should be that they would never be in trouble and need help from no one. Brotherhood is also shared between me and Mr. LUO Haining, who has kept running besides me both in the thesis realm and in the sport field, and who has been surprising me by his self-discipline.

But I should say a big "thank you" to my real dear elder brother and elder sister, who worked so hard to provide a good living of our family, and liberated me from extra worries. Thank you for cheering me up when I felt depressed, and thank you for sharing with me the daily happiness about my loveliest nephew and niece. I'm proud of being part of you.

Also, I should be thankful for Dan-Gabriel CALUGARU and Laurent POUILLOUX who generously gave me technical backups with humorous jokes when my computer was telling serious jokes. And pleasures are mine to have known GU Baiyang, a wonderful classmate of middle school, who generously kept an eye on possible job offers for me, and encouraged me to seek better choices.

For sure, there are still a lot of people such that I can never exhaust the list and to whom I owe grateful and heartful expressions. You are the treasure of my life.

What happens in Vegas, stays in Vegas. But what happens in Lyon, especially the beautiful coffee moments with dear *Miss Nespresso*, goes with me to any possible place.

Cependant, la vie sépare les gens tout doucement sans aucun bruit. On ne saurait jamais s'il y a le moment de se revoir, mais on dit comme d'habitude : “Au revoir.” Un départ ne signifie lui-même jamais la fin d'une histoire, mais plutôt le début d'une autre qui est toute neuve. Or qu'est-ce qui est merveilleux là-dedans ? Avoir pu passer un temps avec vous, c'est ce qui est merveilleux là-dedans.

P.S.

Special thanks are given to the jury of my thesis defense, who have come to examine my presentation after a long journey and have inspired me by their original questions and opinions.

At the end of the end, may I express my highest gratitude to the China Scholarship Council that have entirely financed my thesis during the past 3 years. Whenever the duty is called, I will be ready to contribute to the properity of my motherland.

—— Written right before the 70th anniversary of the People's Republic of China.

Abstract

Axisymmetric turbulence is a two-dimensional three-component flow. The investigation of this type of turbulence is motivated by the fact that it represents an asymptotic limit of anisotropic flows and that it has been the subject of theoretical investigations in the past. In the present manuscript, such a flow is investigated in wall-bounded cylindrical geometry using spectral and pseudo-spectral numerical simulations.

Previous results on the generation of coherent structures, obtained for freely decaying flows, are here assessed in the context of statistically steady flows, where the energy is supplied by either a spectrally localized forcing, or by moving top and bottom plates of the cylinder. The mean flow displays coherent structures whose properties are compatible with theoretical predictions.

When an anisotropic forcing protocol is used, a bifurcation is observed from a non-swirling (two-dimensional two-component, 2D2C) to a swirling (two-dimensional three-component 2D3C) turbulent flow. This transition is modelled by a system of two ordinary differential equations (ODE). It is shown that this model is able to reproduce the essential physics of the transition.

The transition of the axisymmetric (2D3C) to three-dimensional (3D3C) flow is then investigated using a non-integer dimension, by smoothly introducing azimuthal variations into the system. It is shown that the 2D2C limit is singular and that small azimuthal variations allow a redistribution of energy over the different energy components. The ODE model is adapted for this system by modelling the pressure-strain correlation. It is shown how the swirl level depends on the non-integer dimension. Large-Eddy Simulations are carried out to assess the robustness of these results at higher Reynolds number.

Key words :
turbulence, coherent structures, turbulence modelling, transition, numerical simulation.

Résumé

La turbulence axisymétrique est un écoulement bidimensionnel trois-composantes. L'étude de ce type de turbulence est motivée par le fait que celle-ci représente la limite asymptotique des écoulements anisotropes, et qu'elle a été le sujet des investigations théoriques dans le passé. Dans ce manuscrit, la turbulence axisymétrique a étudié en géométrie fermée en utilisant des simulations numériques spectrales et pseudo-spectrales.

Les études antérieures concernant la génération des structures cohérentes, obtenues dans les écoulements en déclin libre, sont considérées ici dans le contexte des écoulements statistiquement stationnaires, où l'énergie est injectée soit par un forçage spectralement localisé ou par une rotation des disques en haut et en bas du cylindre. On montre que les structures observées sont conformes aux prédictions théoriques.

Lorsqu'un protocole de forçage anisotrope est utilisé, une bifurcation est observée entre un état non-tourbillonnant (bidimensionnel deux-composantes, 2D2C) et un écoulement tourbillonnant turbulent (bidimensionnel trois-composante, 2D3C). Cette transition est modélisée à travers un système de deux équations différentielles ordinaires (ODE), et on montre que ce modèle retient la physique essentielle de cette transition.

La transition de l'écoulement axisymétrique à un écoulement tridimensionnel (3D3C) est ensuite étudiée à l'aide d'une dimension non-entière, en introduisant de façon continue la variation azimutale dans le système. On montre que la limite 2D2C est singulière et qu'une petite variation azimutale permet une redistribution d'énergie sur les différentes composantes énergétiques. Le modèle ODE est adapté pour ce système et on montre que pour l'écoulement considéré la corrélation pression-déformation est responsable d'un niveau approximativement proportionnel à la dimension non-entière. Des Simulations des Grandes Echelles sont réalisées pour évaluer la robustesse des observations à grands nombres de Reynolds.

Mots-clé :

turbulence, structures cohérentes, modélisation de turbulence, transition, simulation numérique.

Table des matières

Nomenclature

Theoretical

$\{,\}$	Poisson brackets
$\langle\rangle$	volume average
$\langle,\rangle$	inner product
Δ_*	generalized Laplacian operator
δ_{ij}	Kronecker symbol
E, E_P, E_T	kinetic energy and its poloidal and toroidal components
Γ_n	nth-order Casimir in 2D turbulence
$\mathcal{H}$	Hamiltonian
H_m, I_n	mth-order and nth-order Casimirs in axisymmetric turbulence
J_0, J_1	0th- and 1st-order Bessel functions of the first kind
k	wave-number
L_P, L_T	typical length scales in poloidal and toroidal directions
ν	kinematic viscosity
ω, $\boldsymbol{\omega}$	vorticity scalar and vector
p, p_t	pressure and total pressure
ψ	stream function
r, θ, z	cylindrical coordinates
$\mathbf{r}$	spatial position vector
$\mathcal{R}_r$, $\mathcal{R}_\theta$, $\mathcal{R}_z$	derivative ratios between toroidal and poloidal directions
ρ	probability density function
S	Boltzmann entropy
σ	angular momentum
t, τ	time and typical time scale
$\mathbf{u}$, u_r, u_θ, u_z	velocity field and its components in cylindrical coordinates
U	typical velocity scale
x, y	Cartesian coordinates
ξ	pseudo-vorticity
Z	enstrophy

Numerical methods

α	control parameter of axisymmetry level
β	linear forcing parameter in radial and axial directions
$\mathbf{B}_{qn}$	vectorial basis for decomposing the axisymmetric velocity field
C_{qn}	decomposition coefficients prefixed to $\mathbf{B}_{qn}$
C_P, C_T	spectral energy injection parameters
D	computational domain
G	cylinder aspect ratio
k_n, γ_q	wave-numbers of the axial and radial directions
λ_{qn}	effective wave-number of the poloidal plane
k_E, k_Z, k_{I_1}, k_{H1}	dissipation scales
ε_E, ε_Z, ε_{I_1}, ε_{H_1}	dissipation rates
ν^-	negative viscosity
Ω	angular velocity of counter-rotating discs
P_n	nth-order Legendre polynomial
$\Pi(k,t)$	energy flux spectrum function
R, H, V	cylinder radius, height and volume
T_k	kth-order Chebyshev polynomials
Δt	time step
x_i	collocation point set

Modelling

c_Π	first constant in the Π model
d_P, d_T	dissipation coefficients in poloidal and toroidal dissipation rate models
ε_P, ε_T	poloidal and toroidal dissipation rates
F_P, F_T	forcing powers in poloidal and toroidal directions
γ	swirl indicator
λ	second constant in the Π model
Π	pressure-strain correlation
τ	typical time scale
T	toroidal-to-poloidal energy transfer
ζ	dimensionless coefficient in the T model

Abbreviations

2D	two-dimensional
2D2C	two-dimensional two-component
2D3C	two-dimensional three-component
3D	three-dimensional
3D3C	three-dimensional three-component
CK	Chandrasekhar-Kendall, two authors
c.g.	coarse-grained
DNS	direct numerical simulation
f.g.	fine-grained
FSM	fully spectral method
LES	large-eddy simulation
ODE	ordinary differential equation
OpenMP	Open Multi-Processing
PDF	probability distribution function
PSM	pseudo-spectral method
RANS	Reynolds-averaged Navier-Stokes
Re	Reynolds number

Chapitre 1

Introduction & Outline

Turbulence is related to human lives in many aspects, since it appears widely in domains ranging from natural science to industrial engineering. It is also one of the most difficult problems in fluid mechanics due to its chaotic nature. It is difficult to fully describe turbulent flows even as “simple” as smoke going out of a chimney. But the attempts to improve our understanding of the phenomenon have never stopped. During the 20th century, efforts have been made by physicists and engineers multiplying the angles of attack to understand and model turbulence. By using different hypotheses, from the simplest to more and more complicated, many theories as well as modelling methods have been put forward to explain and predict some general phenomena and macroscopic properties. Simultaneously, experiments and numerical approaches are designed to validate results obtained from theories and models. There are famous and classic subjects such as the Kolmogorov 1941 theory for homogeneous isotropic turbulence, the eddy viscosity models as well as Reynolds stress models for Reynolds-averaged Navier-Stokes simulations, the eddy-damping quasi-normal Markovian theory for spectral equation closure, *etc.*

In this thesis, we discuss statistical mechanics methods for Euler flows ; we investigate turbulence behavior under dimensionality transition, and model the observations. These features will be briefly presented in the following sections of this chapter.

1.1 Statistical mechanics applied to turbulence (Chapters 2 & 4)

During the last decades, the statistical physics of out-of-equilibrium systems has become a particularly active field of research and has seen the blooming of various theoretical results that are often difficult to be experimentally tested. However, turbulence offers an appropriate investigation framework for such theories due to the large number of degrees of freedom that it develops over a wide range of spatio-temporal scales, and indeed, an approach attempting to better understand turbulence has been established on the basis of statistical mechanics. Historically, this approach started with the conjecture of Onsager [1] who came up with the idea to describe the clustering of like-sign point-wise (thus discrete field) vortices as a result of entropy increase in the context of inviscid two-dimensional turbulence. This work explains somehow the emergence of long lasting large-scale structures in turbulence that can be regarded as two-dimensional, and ushers people to treat two-dimensional turbulence in the way of statistical physics. Tools were then borrowed from statistical mechanics to try to investigate the continuum inviscid two-dimensional case, and independently in the early 90s, Miller [2] and Robert and Sommeria [3] use the Boltzmann entropy S, which is one of the fundamental concepts in statistical physics, and they succeed in applying the statistical mechanics method to the Euler equations. This tool is later extended to study more concrete cases, such as the spontaneous geostrophic ocean jets/rings (the Kuroshio and the Gulf-Stream for example) [4], and the persisting banded structures and the Great Red Spot on Jupiter

[5], *etc.* Because these flows all have two dimensions which are much bigger than the third one, they are regarded in the context of two-dimensionality and can be explained as a consequence of statistical equilibria.

The extension of this tool towards three-dimensionality was initiated by Leprovost *et al.* [6] by considering the case of the axisymmetric Euler equations. An axisymmetric system is a system such that, when its evolution equation is written in cylindrical coordinates (r, θ, z), all azimuthal derivatives are set to zero : $\partial_\theta X = 0$, meaning that the system can have motions in all three dimensions but depends only on the two coordinates r and z. Thus, an axisymmetric case is termed as "2-dimensional 3-component" (denoted as 2D3C henceforth) or sometimes "2.5-dimensional" : an intermediate situation between two-dimensionality and three-dimensionality. Such ideal flows do not exist in practice but are worth investigating from an academic point of view. Furthermore, tokamaks *i.e.* fusion plasmas confined by a strong toroidal magnetic field, display close to axisymmetric behavior. In the absence of forcing and viscous dissipation, an infinite number of quantities (such as kinetic energy and helicity) are conserved. Similarly as in the 2D case, a Boltzmann entropy S can be defined, and maximization problems of S (as well as their equivalent variants) under different selected conservation constraints can be written. Again, without solving the Navier-Stokes equations, the solutions of such optimization problems predict the existence of long-lasting and large-scale poloidal structures. Qu *et al.* [7, 8, 9] were the first to carry out numerical simulations of axisymmetric flows, with periodic axial boundary condition. By using a fully spectral method, both large-scale structures and relevant functional relationships were observed.

In this thesis, we build upon the investigation by Qu *et al.* [7, 8, 9]. Sections 2.1.1 and 2.1.2 are reserved for a more detailed presentation of statistical mechanics applied to turbulent flows, and in Chapter 4 these theoretical considerations are assessed using numerical simulations.

1.2 Numerical methods (Chapter 3)

In the current thesis, two different existing codes are adapted for our purposes. Both codes are written in Fortran programming language.

Our first code is transformed from the fully spectral method adapted by Qu [8] in order to simulate axisymmetric turbulence. The code was initially designed by Chen *et al.* [10] for numerical studies in magnetohydrodynamics within a cylindrical computation domain. The method in [10] consists in applying the Chandrasekhar-Kendall (denoted as "CK" for short in the sequel) basis which is complete and orthonormal to decompose the velocity field, mainly featured by the utilization of Bessel functions of the first kind for radial (r direction) decomposition and Fourier series for both azimuthal (θ direction) and axial (z direction) decompositions. However, the application of Fourier series in the axial direction imposes periodic boundary conditions to the two ends of z coordinates, leading to a geometry of an axially periodic cylinder. In our case, adaptation of the CK basis is carried out : the discretization in the θ direction is suppressed as is done in [8] since the flows are ideally axisymmetric, and the discretization in the z direction is performed by sine and cosine functions, in order to confine the cylinder in the axial direction. Section 3.1 is reserved for a full description of this fully spectral method. The code is restructured, converted to modern Fortran language and parallelized via the

OpenMP toolkit. Section 4.1 gives the validation of our first code by comparing our numerical results with theoretical predictions from the statistical mechanics method and with numerical findings in [8].

Our second code is based on the pseudo-spectral method designed by Serre and collaborators [11] aiming at simulating three-dimensional turbulent flows in a cylindrical cavity. Similarly, Fourier series are used to decompose the velocity field in the azimuthal direction. But at difference with the fully spectral method, Chebyshev polynomials of the first kind are applied to discretize the radial and axial directions, avoiding a singularity point at $r = 0$. Derivatives are accurately calculated in spectral space while multiplications are conducted in physical space. In our case, a control parameter of the axisymmetry level α is inserted into the codes to allow for a dimensionality between axisymmetric and general three-dimensional spaces. A restructuring and a parallelization via OpenMP are done. Moreover, the code is also adapted into a strictly axisymmetric version. Section 3.2 is devoted to the description of this method, and Section 4.2 offers the validation of the axisymmetric version as a complementary confirmation of theoretical and numerical results known in axisymmetric turbulence by the statistical mechanics method.

1.3 Dimensionality transitions (Chapters 5 & 6)

The behavior of turbulent flows depends on the configuration of the system, and can greatly deviate from ones to others. The dimensionality (two- or three-dimensional) is clearly a crucial control parameter. For example, by changing the aspect ratio of a flow, its behavior can be drastically modified. Both forward and inverse, and even split energy cascades can be observed (meaning that energy is transferred simultaneously to large and small scales).

One should remark that strictly speaking, the space dimension d should be integer of either 1 or 2 or 3. In theoretical research, however, it is not a rare procedure to extent results from integer space dimensions to non-integer space dimensions or even to $d > 3$.

In this thesis, we will numerically study the dimensionality transition from different points of view without explicitly engaging the dimension d. Two kinds of transitions will be focused on :

- the transition from non-swirling (two-dimensional two-component, denoted as "2D2C" henceforth) to swirling flow (2D3C or 2.5-dimensional as explained in Section 1.1). Chapter 5 is reserved for the presentation of this aspect ;
- the transition from axisymmetric flows (2.5-dimensional) to general cylindrical three-dimensional flows. Results obtained with the second code (equipped with the axisymmetry controlling parameter α) are presented in Chapter 6.

Analyses of these two kinds of transition behavior will be carried out in these two chapters, by proposing corresponding models that describe the system dynamics.

To the best of our knowledge, these are the first models concerning dimensional transitions of cylindrical flows. As a starting point, we propose the simplest models, considering global, volume averaged quantities, using techniques reminiscent of early modelling efforts. Thus a brief introduction on models solving Reynolds-averaged

Navier-Stokes (called “RANS” hereafter) equations for the mean velocity field is given in Chapter 2, based on the presentation done by Pope in [12]. In particular, we focus on turbulent-viscosity models.

1.4 Main contributions and results in this thesis

- Chapters 3 & 4.
  A fully spectral code of axisymmetric turbulence is adapted with confinement of the numerical domain. Theoretical predictions of statistical mechanics methods concerning axisymmetric turbulence are validated at higher Reynolds numbers than in the previous investigations [7, 9]. A pseudo-spectral code in cylindrical geometry is adapted for axisymmetric turbulence with more realistic boundary conditions and the allowance of higher Reynolds numbers than the spectral code. Theoretical results (cascade direction, functional relationships) of statistical mechanics methods are reconsidered.

- Chapter 5.
  Investigation of the transition phenomena of axisymmetric turbulence from non-swirling to swirling regimes through simulations. A model based on large-scale motions is established to reproduce the transition.

- Chapter 6.
  The pseudo-spectral code is further developed to allow the study of flow transitions from the axisymmetric to the general three-dimensional regime. The nature of the transition observed in simulations is discussed. The extension of the model derived in Chapter 5 to match this second kind of dimensionality transition is attempted.

The main text is concluded by a chapter including the conclusions and perspectives, and some mathematical and technical details are given in the appendices.

CHAPITRE 2

Theoretical Details

Axisymmetric turbulence is invariant with respect to the azimuthal direction in cylindrical coordinates, and is thus a sort of 2D3C turbulence. Indeed, it shares many similarities with two-dimensional turbulence, and the statistical mechanics method for axisymmetric turbulence can therefore be transposed from that for two-dimensional turbulence by analogy. Also the transitions that we will study in this thesis have been explored for the case of 2D turbulence. In this chapter, for pedagogical reasons we start therefore by discussing 2D turbulence in order to better present axisymmetric turbulence thereafter and to illustrate the relationship between the two. The statistical mechanics used to predict stationary states of both 2D and axisymmetric turbulence will be first detailed (Section 2.1). Then the state of the art concerning the dimensionality transition in hydrodynamics will be presented in Section 2.2. A brief discussion of RANS models will be appended to the end of this chapter (Section 2.3).

2.1 Statistical mechanics

2.1.1 Two-dimensional flows

Navier-Stokes equations in two dimensions

The dynamics of unforced incompressible flows is characterized by the Navier-Stokes equations

$$\nabla \cdot \mathbf{u} = 0, \tag{2.1}$$

$$\frac{\partial \mathbf{u}}{\partial t} + (\mathbf{u} \cdot \nabla)\mathbf{u} = -\frac{1}{\rho}\nabla p + \nu \Delta \mathbf{u}, \tag{2.2}$$

where $\mathbf{u}$ is the velocity field, ρ the density, p the pressure and ν the kinematic viscosity. Though movements evolve in only two dimensions, the velocity can still be written in a three-dimensional form as $\mathbf{u} = (u, v, 0)$ with u and v functions of x and y (if we take Cartesian coordinates system for example). One can then find, by taking the curl of $\mathbf{u}$, that the vorticity $\boldsymbol{\omega}$ occupies only the z dimension and is always perpendicular to the velocity :

$$\omega = (\nabla \times \mathbf{u})_z. \tag{2.3}$$

Thus, by taking the curl of Eq.(2.2), one obtains a “new” equation in terms of ω,

$$\frac{\partial \omega}{\partial t} + (\mathbf{u} \cdot \nabla)\omega = \nu \Delta \omega, \tag{2.4}$$

which describes the same as Eq.(2.2). Through the incompressibility condition (2.1) and the Cauchy-Riemann theorem, the velocity $\mathbf{u}$, as well as the (scalar) vorticity ω, can be expressed by using a stream function ψ as

$$\mathbf{u} = \left(\frac{\partial \psi}{\partial y}, -\frac{\partial \psi}{\partial x}\right), \quad \omega = \nabla \times \mathbf{u} \cdot \mathbf{e_z} = -\Delta \psi. \tag{2.5}$$

This offers the possibility to combine the incompressibility condition and the dynamical equation by substituting $\mathbf{u} = (\partial_y \psi, -\partial_x \psi)$ in Eq.(2.4), giving

$$\frac{\partial \omega}{\partial t} + \left(\frac{\partial \omega}{\partial x}\frac{\partial \psi}{\partial y} - \frac{\partial \omega}{\partial y}\frac{\partial \psi}{\partial x} \right) = \nu \Delta \omega. \tag{2.6}$$

We introduce here the definition of Poisson brackets $\{a, b\} = \partial_x a \partial_y b - \partial_y a \partial_x b$, via which (2.6) turns into a simpler form

$$\frac{\partial \omega}{\partial t} + \{\omega, \psi\} = \nu \Delta \omega. \tag{2.7}$$

In Eq.(2.7), $\{\omega, \psi\}$ is the non-linear term. In particular, when a is a function of b, *i.e.*, $a = f(b)$, it can be easily proved that $\{a, b\} = 0$. Therefore, some peculiarities can be expected in a state where $\omega = f(\psi)$. Under such circumstances, the non-linear effects are absent and the dynamics are affected by viscous dissipation only. In addition to the functional relationship $\omega = f(\psi)$, if viscosity is ruled out *i.e.* $\nu = 0$, or balanced by forcing, the dynamics of the two-dimensional system turns into a stationary form $\partial_t \omega = 0$, which is extremely simple but interesting. A vorticity field that does not evolve with time is dubbed as "coherent". We thus call, in practice, the notable and long-lasting structures "coherent structures". As we will see, coherent structures coupled with $\omega = f(\psi)$ relationships are observed in several types of flows.

Quantities conserved in two dimensions

In the inviscid limit, the first conserved quantity we consider is the kinetic energy. Its conservation can be easily proved, for example, under Cartesian coordinates using the spatial homogeneity hypothesis. In fact, defined as $E = \int_D \mathbf{u}^2(\mathbf{r})/2\mathrm{d}\mathbf{r}$, the evolution equation of E over a spatial statistically homogeneous or periodic domain D in either two or three dimensions writes

$$\frac{\mathrm{d}E}{\mathrm{d}t} = -\nu Z \tag{2.8}$$

with $Z = \int_D \boldsymbol{\omega}^2(\mathbf{r})\mathrm{d}\mathbf{r}$ the enstrophy. Then in the absence of viscosity, one gets simply $\partial_t E = 0$, showing the conservation of the kinetic energy in 2D and 3D[1].

Apart from E, the statistical moments of ω of any integer order n are also invariants in 2D. Actually, if we remove the right hand side of Eq.(2.4), the two-dimensional Euler momentum equation can be obtained

$$\frac{\partial \omega}{\partial t} + (\mathbf{u} \cdot \nabla)\omega = 0. \tag{2.9}$$

Then the following equation can be derived :

$$\frac{\mathrm{d}}{\mathrm{d}t}\int_D \omega^n(\mathbf{r})\mathrm{d}\mathbf{r} = \int_D n\omega^{n-1}(\mathbf{r}) \left(\frac{\partial \omega(\mathbf{r})}{\partial t} + \mathbf{u} \cdot \nabla \omega(\mathbf{r}) \right) \mathrm{d}\mathbf{r} = 0, \tag{2.10}$$

recalling that the case of $n = 2$ corresponds to the conservation of the 2D enstrophy. The justification Eq.(2.10) is equivalent to say that integrals of any smooth function $C(\omega)$ over the domain D are conserved

$$\frac{\mathrm{d}}{\mathrm{d}t}\int_D C(\omega(\mathbf{r}))\mathrm{d}\mathbf{r} = 0. \tag{2.11}$$

---

[1] Note that this considers $\nu = 0$. The limit $\nu \to 0$ is non-trivial and only in 2D it can be shown that energy is conserved in this limit.

They form a category of invariants called Casimirs of the system [13].

Particularly, the enstrophy Z is a conserved quantity and is positive definite. Its conservation blocks the energy to cascade in a forward direction, and inversely forces the energy to cascade from smaller to larger scales, which leads to the emergence of energetic large scales. It is observed that in many cases these energetic scales are associated with well defined coherent structures. A schematic energy spectrum of 2D turbulence can be seen in Fig.2.1. However, the appearance of such large-scale long-lasting structures can also be theoretically explained from another angle, namely through statistical mechanics theories that will be introduced thereafter.

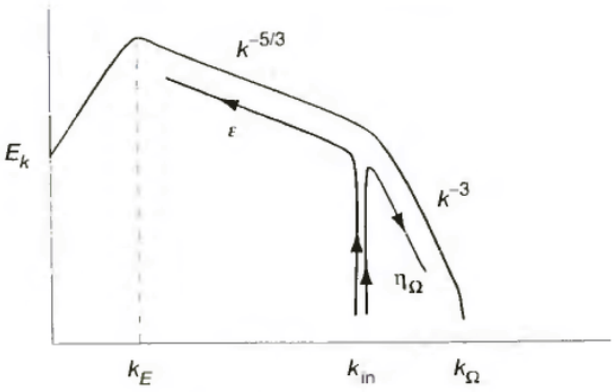

FIGURE 2.1: Picture cited from [14]. Energy spectrum of a 2D forced turbulent flow. The forcing takes place at medium scales k_{in}, and energy is largely transferred to larger scales characterized by k_E, yielding an inverse energy cascade. Scaling slopes can be obtained via dimensional analysis and are numerically as well as experimentally shown to be $-5/3$ and -3 for respectively the inverse energy cascade and the direct enstrophy (denoted as Ω in this picture) cascade. ε and η_Ω are corresponding energy and enstrophy flux rates.

Statistical mechanics for 2D turbulence

For long, turbulent flows have been decomposed into a mean flow and the fluctuations around them. This allows the mean flow and the fluctuation to be approximated by turbulence models. An effective modelling theory should then be able to provide information on both the mean flow and the fluctuations considering only a moderate number of degrees of freedom but without discarding too much of the physics. Then a tempting idea is to treat turbulent systems by approaches borrowed from statistical mechanics. The following paragraphs review the development of such approaches.

In the late years of the 19th century, Kirchoff [15] first noticed that in the case of two-dimensional incompressible inviscid fluids modelled with point-wise vortices (also called “vortex gas”), the equations of motion can be considered as a result derived from a quantity

$$\mathcal{H} = -\sum_{i \neq j} \kappa_i \kappa_j \ln |\mathbf{r}_i - \mathbf{r}_j| \tag{2.12}$$

where κ_i is the circulation of the i-th point-wise vortex and $\mathbf{r}_i = (x_i, y_i)$ designates the corresponding position vector. Then the dynamics of the system is characterized by

$$\kappa_i \frac{\mathrm{d}\mathbf{r}_i}{\mathrm{d}t} = \nabla_i \times \mathcal{H}. \tag{2.13}$$

The dynamical equation (2.13) is written in a Hamiltonian form. Indeed, if the variables (x_i, y_i) are considered conjugate coordinates (and they actually can be), the point-wise vortex system is a Hamiltonian system. Studies were then undertaken to try to explain Euler dynamics through this Hamiltonian system. In particular, with a Hamiltonian at hand, it is normal to look into the equilibrium properties of the system via methods of statistical mechanics.

Generic attempts date back to the late 1940s initiated by the conjecture of Onsager [1]. Indeed, 2D turbulence has been observed to be self-organizing into large-scale coherent structures in nature (like jets, ocean rings, cyclones, *etc.*), in laboratory experiments and in numerical simulations. Onsager put forward a theory describing the formation of coherent structures in 2D systems as a result of equilibrium statistical mechanics. He pointed out that within a bounded region and at high energies, the system with a large but finite number of point-wise vortices of which the dynamics are described by the Hamiltonian (2.12) would evolve to form large structures through the coalescence of like-sign vortices. In fact, provided a confinement of vortex positions in the physical space and the assumption of ergodicity, the volume occupied by possible states of the system in the phase space is finite. This leads to an important result argued by Onsager : beyond a certain threshold of energy, the entropy should decrease somehow when energy is still fed into the system. He gave a simpler example of only two point-wise vortices of the same sign, pointing out that the total kinetic energy becomes higher as the two vortices get closer. Then he presented his conjecture that the only possible means for the vortex gas system to contain more energy is to draw like-sign vortices closer, *i.e.*, to give rise to like-sign vortex clusters. A consequence is that when like-sign vortices are approached to each other, their positions are "better" arranged compared to the initially chaotic configuration, and the entropy is bound to decrease. In fact, when the energy of the system has already past a threshold, fewer possible states can be reached if more energy is injected in, leading to a decrease of the entropy. In particular, the temperature in traditional statistical mechanics is defined as

$$\frac{1}{T} = \frac{\partial S}{\partial E}, \tag{2.14}$$

where S designates the entropy that characterizes the number of possible states under the constraint of a fixed energy level E. Then noticeably, the above point-wise vortex system has a negative temperature since the entropy diminishes when kinetic energy increases.

Based on this discontinuous point-vortex model, Onsager then suggested a probabilistic treatment, assuming that the generation of the large-scale two-dimensional vortices could also be regarded as a result that stems from a Hamiltonian system conserving the kinetic energy and the enstrophy (in the absence of viscosity). This conjecture, based on Onsager's sharp insights and intuitions, was not proved nor developed until the work by Joyce and Montgomery almost three decades later.

In 1973, Joyce and Montgomery [16] adapted the idea of Onsager for their own system of charged rods placed in a plasma and aligned with a uniform magnetic field. In this study of two-dimensional electrostatic guiding center plasma, charged rods are analogous to point-wise vortices in Onsager's case since they force, through the combined effect of the magnetic field, the movement of plasma around them. Then the driven plasma movement is considered equivalent to the velocity field induced by parallel point-wise vortices, and the following results can be used as support for Onsager's conjecture.

In Joyce and Montgomery's study, $2N$ electric rods are taken into account. Half of them are charged with $1/N$ while the other half with $-1/N$, and the system present an overall electric neutrality. Then equivalently, this represents a point-wise vortex field whose global circulation is zero, and of which the vorticity of each vortex is equal to $1/N$ or $-1/N$. Hence if one defines $\omega_i = 1/N$ or $-1/N$, the Hamilton equations (2.13) can be involved to describe the dynamics. It is interesting that the quantity $\mathcal{H}$ in Eq.(2.13) is reminiscent of the stream function ψ (recall that in practical 2D fluid systems, $u_x = \partial_y\psi$, $u_y = -\partial_x\psi$), except that ψ characterizes a continuous fluid field while $\mathcal{H}$ here characterizes a discrete field. For convenience, the subsequent details are carried out on the basis of the equivalent point-wise vortices model.

In fact, the discrete vorticity field can be expressed as a function of the spatial position $\mathbf{r}$. To obtain this expression, the vortex density distribution function should be first defined :

$$\begin{aligned} &\rho_\pm(\mathbf{r}) = \frac{1}{N}\sum_{i=1}^{N}\delta(\mathbf{r}-\mathbf{r}_i^\pm), \\ &\delta(\mathbf{r}-\mathbf{r}_i^\pm) = \begin{cases} 1 & \text{if } \mathbf{r} = \mathbf{r}_i^\pm \\ 0 & \text{if } \mathbf{r} \neq \mathbf{r}_i^\pm \end{cases}, \end{aligned} \tag{2.15}$$

where ± labels vortices with positive and negative vorticity respectively. Then the distribution of the discrete vorticity field can be established through the density distribution :

$$\omega(\mathbf{r}) = \rho_+(\mathbf{r}) - \rho_-(\mathbf{r}). \tag{2.16}$$

Eq.(2.16) means that the normal value of ω is $1/N$, $-1/N$ or 0. After some calculation, it can be found $\omega = -\Delta\mathcal{H}$, which means that the Hamiltonian quantity $\mathcal{H}$ can really be regarded as the discrete stream function ψ. Then similarly, the kinetic energy of the system is calculated as

$$E = \int \psi\omega \mathrm{d}\mathbf{r}. \tag{2.17}$$

The generalized Boltzmann entropy of a system is defined from the distribution density function $f(\sigma, \mathbf{x})$ of the system as $S = -\int f \log f \mathrm{d}\sigma\mathrm{d}\mathbf{x}$. In Joyce and Montgomery's case, this entropy writes

$$S = -\int \rho^+(\mathbf{r})\log\rho^+(\mathbf{r})\mathrm{d}\mathbf{r} - \int \rho^-(\mathbf{r})\log\rho^-(\mathbf{r})\mathrm{d}\mathbf{r}. \tag{2.18}$$

As the vortex number and intensity are defined and by default cannot be changed, the global vorticity, known as the overall circulation Γ, is a conserved quantity :

$$\Gamma = \int \omega(\mathbf{r})\mathrm{d}\mathbf{r} = \int (\rho^+(\mathbf{r}) - \rho^-(\mathbf{r}))\mathrm{d}\mathbf{r}. \tag{2.19}$$

In order for the system to be isolated from the "environment", an additional conservation constraint with respect to the kinetic energy E is imposed, *i.e.*, neither forcing nor dissipation is included. This is indeed the case according to Onsager's analysis. Then to derive the final equilibrium state of the system, Joyce and Montgomery consider the maximization of the entropy with E and Γ fixed :

$$\max_{\rho} \{S(\rho)|E, \Gamma\}. \tag{2.20}$$

The desired equilibrium states are the solutions of the variational equation

$$\delta S - \beta\delta E - \alpha\delta\Gamma = 0, \tag{2.21}$$

where β and α are Lagrangian multipliers. A first remark is that β is associated with the “temperature” in Onsager’s conjecture. In fact, β is the inverse of the thermodynamic temperature in such kind of studies. By substituting the expressions of S, E and Γ, the variational equation becomes

$$\delta \int \left[-\rho^+ \log \rho^+ - \rho^- \log \rho^- - \beta\psi(\rho^+ - \rho^-) - \alpha(\rho^+ - \rho^-)\right] \mathrm{d}\mathbf{r} = 0. \tag{2.22}$$

As $\delta \int F(\rho) = 0$ yields $F'(\rho) = 0$, it can be deduced from Eq.(2.22)

$$\begin{aligned} &1 + \log \rho^+ + \beta\psi + \alpha = 0, \\ &1 + \log \rho^- + \beta\psi + \alpha = 0. \end{aligned} \tag{2.23}$$

One then obtains

$$\begin{aligned} \rho^+ &= \exp(-(1 + \beta\psi + \alpha)), \\ \rho^- &= \exp(-(1 - \beta\psi - \alpha)), \end{aligned} \tag{2.24}$$

which are in forms of Boltzmann distributions. Recalling that $\omega = \rho^+ - \rho^-$, the final expression of the vorticity field reads

$$\begin{aligned} \Rightarrow \omega &= \exp(-1)\left(\exp(-(\beta\psi + \alpha)) - \exp(\beta\psi + \alpha)\right) \\ &\sim \sinh(-(\beta\psi + \alpha)). \end{aligned} \tag{2.25}$$

Thus, the vorticity of the point-wise vortices system is a functional of the stream function, which implies $\{\omega, \psi\} = 0$. This means that the current result is a stationary solution of a 2D Euler system. Although the obtained dynamics (2.25) is far from being turbulent, subsequent simulations of freely decaying two dimensional turbulence within doubly periodic domains roughly evolve towards systems where the functional relation (2.25) is well verified [17].

The work of Joyce and Montgomery was a more rigorous support for the conjecture of Onsager. However, there are some scants of the current model. In fact, the point-wise vortex model makes sense only when the dilute (low density) limit is satisfied. When the system presents a higher and higher density of point-wise vortices, the dynamics tends to depart from what a continuous system should be. Even Onsager himself was uncertain how the statistics of discrete point-wise vortices could be adapted for situations where the vorticity field should be continuous. Besides, Onsager underlined that on the basis of the dilute vortex gas model, a continuous velocity field could be approximated by a certain number of different ways which led to a variety of equilibrium states. All these difficulties call the advent of a more proper theory for applying statistical mechanics approaches on continuous two-dimensional turbulence systems.

Separately but almost simultaneously, a theory suitable for continuous vorticity fields has been proposed by Miller [2] and Robert and Sommeria [3] in the early 1990s. In their work, they consider a bounded domain with bounded vorticity magnitude (by some $|\omega|_{\max}$). One crucial advance is the introduction of a probability distribution of local vorticity level $\rho(\sigma, \mathbf{r}, t)$. The presence of this distribution function is the response to the difficulty of describing the micro-structure of the local vorticity $\omega(\mathbf{r}, t)$.

In a two-dimensional Euler system, if damping and forcing effects are both ruled out, the vorticity transport equation is characterized by pure advection mixing. This results in finer and finer structures without limit *i.e.* infinitely thin filaments. When sufficiently long time is elapsed, such fine structures are no longer within the observable scope and become difficult to describe. As statistical mechanics has always a preference for macroscopic information, these extremely thin filaments are, in this sense, undesirable and should be modelled by some means that allow to predict them in a macroscopic way. The aforementioned vorticity level distribution function $\rho(\sigma, \mathbf{r}, t)$ allows in a statistical manner to measure the probability of the vorticity ω in vicinity of $\mathbf{r}$ to be evaluated between σ and $\sigma + \mathrm{d}\sigma$ at moment t. A first property of ρ is the normalization over all possible value levels of ω :

$$\int \rho(\sigma)\mathrm{d}\sigma = 1. \tag{2.26}$$

Indeed, this allows also the definition of the average and the fluctuation :

$$\begin{aligned} \overline{\omega}(\mathbf{r}, t) &= \int \rho(\sigma, \mathbf{r}, t)\sigma\mathrm{d}\sigma, \\ \omega'(\mathbf{r}, t) &= \omega(\mathbf{r}, t) - \overline{\omega}(\mathbf{r}, t). \end{aligned} \tag{2.27}$$

The averaged vorticity is the average within the local lattice of area l^2, and l can be understood as the smallest observable/concerned scale in statistical mechanics for Euler turbulence. According to this statement, $\overline{\omega}(\mathbf{r}, t)$ forms a local macroscopic vorticity field. Quantities based on $\overline{\omega}$ are called “coarse-grained” (also termed as “macroscopic”) quantities, since non-negligible fluctuation information is excluded in generic relations of $\overline{\omega}^n$ for $n > 1$ *i.e.* $\overline{\omega}^n \neq \overline{\omega^n}$. The authors consider the “fine-grained” (also termed as “microscopic”) statistical quantities :

$$\overline{E} = \frac{1}{2}\int \rho\sigma\psi\mathrm{d}\sigma\mathrm{d}\mathbf{r} = \frac{1}{2}\int \overline{\omega}\psi\mathrm{d}\mathbf{r}, \tag{2.28}$$

$$\overline{\Gamma_n} = \int \rho\sigma^n\mathrm{d}\sigma\mathrm{d}\mathbf{r} = \int \overline{\omega^n}\mathrm{d}\mathbf{r}. \tag{2.29}$$

The authors point out that under an imposed scale l, $\overline{E}$ and $\overline{\Gamma_n}$ approximate the invariants within accuracies ε_E and ε_n. Thus, accuracies get better along with l getting smaller. At a sufficiently small l, although local small-scale oscillations are erased, the $\overline{E}$ and $\overline{\Gamma_n}$ approximate rather well E and Γ_n and should be invariant in Euler conditions. But situations are different for coarse-grained quantities since (henceforth *c.g.* stands for “coarse-grained” and *f.g.* for “fine-grained”)

$$\begin{aligned} E^{c.g.} &= E^{f.g.} = \frac{1}{2}\int \overline{\omega}\psi\mathrm{d}\mathbf{r}, \\ \Gamma^{c.g.} &= \Gamma^{f.g.} = \int \overline{\omega}\mathrm{d}\mathbf{r}, \\ \Gamma_2^{c.g.} &= \int \overline{\omega}^2\mathrm{d}\mathbf{r} \neq \Gamma_2^{f.g.} = \int \overline{\omega^2}\mathrm{d}\mathbf{r} = \int \overline{\omega}^2\mathrm{d}\mathbf{r} + \int \omega_2\mathrm{d}\mathbf{r}, \end{aligned} \tag{2.30}$$

where $\omega_2 \equiv \overline{\omega^2} - \overline{\omega}^2$ is called the local centered variance of the vorticity.

Similar to the work of Joyce and Montgomery, a generalized Boltzmann entropy of the continuous system is defined using the distribution function ρ :

$$S(\rho) = -\int \rho \log \rho \mathrm{d}\sigma \mathrm{d}\mathbf{r}. \tag{2.31}$$

In fact, this entropy is proved equivalent to the logarithm of the system's disorder which represents the number of available microstates corresponding to the macrostate $\rho(\sigma, \mathbf{r})$ calculated by combinatorial analyses [18]. The authors succeed in vindicating that the statistical equilibrium state of the system verifies the maximization of S under the constraints of conserved $E^{f.g.}$ and $\Gamma_n^{f.g.}$:

$$\max_{\rho} \left\{ S(\rho) | E^{f.g.}, \Gamma_n^{f.g.} \right\}. \tag{2.32}$$

Precise mathematical justifications are presented in [3]. It is then reasonable to determine the critical points of the system by solving the variational problem

$$\begin{aligned} &\delta S - \beta \delta E^{f.g.} - \sum_n \alpha_n \delta \Gamma_n^{f.g.} = 0, \\ \Longleftrightarrow &\int \left(\delta(\rho \log \rho) - \frac{\beta}{2} \delta(\rho \sigma \psi) - \sum_n \alpha_n \delta(\rho \sigma^n) \right) \mathrm{d}\sigma \mathrm{d}\mathbf{r} = 0, \end{aligned} \tag{2.33}$$

where β and α_n are Lagrangian multipliers to relevant constraints. By taking the derivation with respect to ρ, one finds

$$\rho = \frac{1}{Z} \exp(-(1 - \frac{\beta}{2} \sigma \psi - \sum_n \alpha_n \sigma^n)) \tag{2.34}$$

with Z a normalizing factor. This is a first result of the Miller-Robert-Sommeria theory that engages all the fine-grained conserved quantities. The $\overline{\omega}$–ψ functional relationship can take diverse forms corresponding to different initial conditions. For more details, Robert and Sommeria [3] point out that the case of Joyce and Montgomery is a low density limit of the current theory. In [2] and [19], it is shown that in the strong mixing or low energy limit characterized by $\beta \sigma \psi \ll 1$, the maximization problem (2.32) is equivalent to the minimization of coarse-grained enstrophy under the constraints of conserved fine-grained energy and fine-grained circulation

$$\min_{\overline{\omega}} \left\{ \frac{1}{2} \Gamma_2^{c.g.} | E^{f.g.}, \Gamma^{f.g.} \right\}. \tag{2.35}$$

They note that to the lowest order of the expansion of $\beta \sigma \psi \ll 1$, only the circulation and the fine-grained enstrophy are relevant among the moments of averaged vorticity. Then for some specific initial conditions resulting in a Gaussian vorticity distribution at equilibrium state, a linear $\overline{\omega} - \psi$ functional relationship can be deduced. In fact, to obtain the critical points of minimization problem (2.35), one should solve the variational problem

$$\begin{aligned} &\delta(\frac{1}{2} \Gamma_2^{c.g.}) - \beta \delta E^{f.g.} - \alpha \Gamma^{f.g.} = 0, \\ \Longleftrightarrow &\int (\overline{\omega} \delta \overline{\omega} - \beta \psi \delta \overline{\omega} - \alpha \delta \overline{\omega}) \mathrm{d}\mathbf{r} = 0, \end{aligned} \tag{2.36}$$

which yields $\overline{\omega} = \beta\psi + \alpha$. Due to the equivalence of the minimization problem (2.35) to the maximization problem

$$\max_{\rho} \left\{ S(\rho) | E^{f.g.}, \Gamma^{f.g.}, \Gamma_2^{f.g.} \right\}, \tag{2.37}$$

a Gaussian distribution, also called the Gibbs state, can be obtained :

$$\rho(\sigma, \mathbf{r}) = \frac{1}{Z(\mathbf{r})} \exp(-\frac{1}{2}(\sigma + \beta\psi + \alpha)^2) \tag{2.38}$$

with $Z(\mathbf{r})$ ensuring the normalization of the integral of ρ against σ. When the inequality of $\beta\sigma\psi \ll 1$ no longer holds, higher moments $\Gamma_n^{f.g.}$ get involved, and the $\overline{\omega} - \psi$ relationship becomes non-linear and recovers the sinh functional when all constraints of $\Gamma_n^{f.g.}$ are taken into account. However, except the cases where extreme values of vorticity show up, a good approximation can be expected when only the conservation of the first invariants is retained.

2.1.2 Axisymmetric flows

General invariants in a three-dimensional Euler flow consist of the kinetic energy and the helicity only. The difference with respect to 2D is the presence of the vortex stretching term in the vorticity equation which leads to an increase of enstrophy. Furthermore, there is a crucial difference between two-dimensional and three-dimensional turbulence : in two dimensions, a system can be characterized by scalar fields like ψ and ω, which are key variables in the statistical mechanics approach ; due to the complexity, however, such a characterization manner cannot be easily fitted into a case of general three-dimensional turbulence unless additional symmetry is present in the system. Axisymmetric turbulence is such a 3D system with additional symmetry. As will be introduced in the sequel, the axisymmetric Euler equations are susceptible to be represented by scalar fields, and have an infinite number of conserved quantities in the inviscid case, which possibly allows the application of the Miller-Robert-Sommeria theory.

An axisymmetric turbulence is characterized by the condition $\partial_\theta = 0$, signifying azimuthal invariance with respect to a fixed axis. Therefore, it is considered as intermediary between 2D and 3D, and sometimes termed as “2.5-dimensional”. Such kind of systems are generally described under cylindrical coordinates, and one adopts usually a cylindrical geometry in both experiments and numerical simulations. On the experimental side, a von Kármán flow being axisymmetric in the average sense [20], Monchaux *et al.* [21] shows the presence of coherent structures within the poloidal plane of the cylindrical device, and functional relationships between scalars that will be presented in the following subsections are measured in the averaged flow. On the numerical simulation side, Qu *et al.* [8, 7, 9] consider a cylinder with a solid lateral wall but periodic top and bottom boundaries. Under this configuration, functional relationships are also observed in simulations of freely decaying flows. The cascades of energy, helicity, circulation, and angular momentum are also studied in stationary out-of-equilibrium cases where forcing and dissipation balance each other. To date, the theoretical predictions are in satisfactory qualitative agreement with experimental and numerical results. This motivates further researches on this 2.5-dimensional regime. Theoretical details, experimental observations and numerical results will be discussed in this subsection.

Axisymmetric 3D Euler equations

To apply statistical mechanics to an axisymmetric system, we begin with the incompressible axisymmetric Euler equations written in cylindrical coordinates :

$$\begin{aligned}
&\frac{\partial u_r}{\partial r} + \frac{u_r}{r} + \frac{\partial u_z}{\partial z} = 0,\\
&\frac{\partial u_r}{\partial t} + u_r\frac{\partial u_r}{\partial r} + u_z\frac{\partial u_r}{\partial z} - \frac{u_\theta^2}{r} = -\frac{1}{\rho}\frac{\partial p}{\partial r},\\
&\frac{\partial u_\theta}{\partial t} + u_r\frac{\partial u_\theta}{\partial r} + u_z\frac{\partial u_\theta}{\partial z} + \frac{u_\theta u_r}{r} = 0,\\
&\frac{\partial u_z}{\partial t} + u_r\frac{\partial u_z}{\partial r} + u_z\frac{\partial u_z}{\partial z} = -\frac{1}{\rho}\frac{\partial p}{\partial z}.
\end{aligned} \tag{2.39}$$

u_r, u_θ, u_z are the three components of the velocity field, p is the static pressure, and ρ is the fluid density. A first remark is that all derivative terms with respect to the **toroidal** coordinate θ disappear due to the axisymmetry, and that the velocity and pressure fields therefore depend only on **poloidal** coordinates r and z. As a result, the system can be studied on one poloidal plane, which offers some convenience when extending the statistical method (as well as when post-processing data). Furthermore, the incompressible equation relates u_r and u_z, and is independent from u_θ. This equation can be rewritten as

$$\frac{1}{r}\frac{\partial (ru_r)}{\partial r} + \frac{\partial u_z}{\partial z} = 0. \tag{2.40}$$

Then like in the two-dimensional situation, there exists a scalar function $\psi(r, z)$ such that

$$\begin{aligned}
u_r &= -\frac{1}{r}\frac{\partial \psi}{\partial z},\\
u_z &= \frac{1}{r}\frac{\partial \psi}{\partial r},
\end{aligned} \tag{2.41}$$

which is the stream function characterizing the poloidal movements. It then becomes obvious that the dynamics of an axisymmetric system can be characterized by the couple of scalar fields (ψ, u_θ). Further, Leprovost [6] points out that the radial and axial components in Eqs.(2.39) can be combined by considering the equation for a new variable ξ, the alleged "potential vorticity" or "pseudo-vorticity", which is defined as

$$\xi = \frac{\omega_\theta}{r} = \frac{1}{r}\left(\frac{\partial u_r}{\partial z} - \frac{\partial u_z}{\partial r}\right), \tag{2.42}$$

where ω_θ is the azimuthal component of the vorticity field $\boldsymbol{\omega} = \nabla \times \mathbf{u}$. This combines the two equations into

$$\frac{\partial \xi}{\partial t} + \frac{\xi}{r^2}\frac{\partial \psi}{\partial z} - \frac{1}{r}\frac{\partial \psi}{\partial z}\frac{\partial \xi}{\partial r} + \frac{1}{r}\frac{\partial \psi}{\partial r}\frac{\partial \xi}{\partial z} - \frac{1}{r^2}\frac{\partial u_\theta^2}{\partial z} = 0. \tag{2.43}$$

ψ can also be fitted into the azimuthal equation by introducing the angular momentum $\sigma = ru_\theta$, leading to

$$\frac{\partial \sigma}{\partial t} - \frac{1}{r}\frac{\partial \psi}{\partial z}\frac{\partial \sigma}{\partial r} + \frac{1}{r}\frac{\partial \psi}{\partial r}\frac{\partial \sigma}{\partial z} = 0. \tag{2.44}$$

To simplify the expressions, one defines a new variable $y = r^2/2$ and a generalized Laplacian operator, denoted as Δ_*, giving first a simple expression of Eq.(2.42) :

$$\Delta_* \psi \equiv \frac{1}{2y}\frac{\partial^2 \psi}{\partial z^2} + \frac{\partial^2 \psi}{\partial y^2} = -\xi. \tag{2.45}$$

Meanwhile, a Poisson brackets that corresponds to the new coordinates (y, z) can also be defined as

$$\{a, b\} = \frac{\partial a}{\partial y}\frac{\partial b}{\partial z} - \frac{\partial a}{\partial z}\frac{\partial b}{\partial y}. \tag{2.46}$$

Then after some algebraic manipulations, Eqs.(2.39) are finally reduced into

$$\begin{aligned} &\frac{\partial \sigma}{\partial t} + \{\psi, \sigma\} = 0, \\ &\frac{\partial \xi}{\partial t} + \{\psi, \xi\} = \frac{\partial}{\partial z}\left(\frac{\sigma^2}{4y^2}\right). \end{aligned} \tag{2.47}$$

It can be recognized from Eqs.(2.47) that σ presents a pure mixing dynamics, reminiscent of the vorticity in two-dimensional Euler systems. After some algebra using the Poisson brackets (2.46), the equations of axisymmetric steady states write

$$\begin{aligned} &\{\psi, \sigma\} = 0, \\ &\{\psi, \xi\} + \{\frac{\sigma}{2y}, \sigma\} = 0, \end{aligned} \tag{2.48}$$

which then reveals that when steady states are attained, σ, ξ and ψ satisfy the following functional relationships :

$$\begin{aligned} &\sigma = F(\psi), \\ &\xi = \frac{F(\psi)}{2y}F'(\psi) + G(\psi). \end{aligned} \tag{2.49}$$

In Eqs.(2.49), F and G are arbitrary functions and depend on detailed information of the steady state. They are determined by initial and boundary conditions which lead to the current steady state.

Statistical mechanics of axisymmetric turbulence

To apply statistical mechanics, one should start by finding out all the conserved quantities. The first conserved quantity in an inviscid flow is the kinetic energy, which can be written as

$$\begin{aligned} E &= \frac{1}{2}\int (u_r^2 + u_z^2)\mathrm{d}\mathbf{r} + \frac{1}{2}\int u_\theta^2 \mathrm{d}\mathbf{r} \\ &= \frac{1}{2}\int \xi\psi \mathrm{d}\mathbf{r} + \frac{1}{2}\int \frac{\sigma^2}{r^2}\mathrm{d}\mathbf{r}. \end{aligned} \tag{2.50}$$

Otherwise, it is proved in [6] that in an axisymmetric Euler system, the only remaining conserved quantities are the Casimirs

$$I_f = \int f(\sigma)\mathrm{d}\mathbf{r} \quad \text{and} \quad H_g = \int \xi g(\sigma)\mathrm{d}\mathbf{r}, \tag{2.51}$$

where f and g are arbitrary functions. This is equivalent to the conservation of any moments of the angular momentum and the generalized helicities

$$I_n = \int \sigma^n \mathrm{d}\mathbf{r} \quad \text{and} \quad H_m = \int \xi\sigma^m \mathrm{d}\mathbf{r}. \tag{2.52}$$

One can remark that the dynamics of angular momentum σ is described by a pure advection mixing equation. For a similar reason as that for the vorticity filamentation in

2D, σ structures of smaller and smaller scales are developed along with the evolution of the flow due to the pure mixing process. This means that a similar coarse-graining procedure is needed to define a resolvable scale limit below which the information is less interesting. Therefore, it is convenient to have again at our disposal the concept of local probability density function $\rho(\mathbf{r},\eta)$ which shows the probability of the value of σ at position $\mathbf{r}$ to be between the levels η and $\eta+\mathrm{d}\eta$. The coarse-grained angular momentum is thus defined as

$$\overline{\sigma}(\mathbf{r},t)=\int\rho(\mathbf{r},\eta,t)\eta\mathrm{d}\eta. \tag{2.53}$$

Like in two dimensions, the theory consists in finding solutions of the maximization problem of a mixing entropy under some conservation constraints. In the current case, the mixing entropy is defined as

$$S=-\int\rho\log\rho\mathrm{d}\eta\mathrm{d}\mathbf{r}, \tag{2.54}$$

while the conversed quantities are naturally the coarse-grained energy, angular momentum moments, generalized helicities and the integral of ρ (normalization principle of probability density functions) with $\bar{\xi}=\xi$ hypothesis :

$$\begin{aligned}\overline{E}&=\frac{1}{2}\int\bar{\xi}\psi\mathrm{d}\mathbf{r}+\frac{1}{2}\int\frac{\bar{\sigma}^2}{r^2}\mathrm{d}\mathbf{r},\\ \overline{I}_n&=\int\bar{\sigma}^n\mathrm{d}\mathbf{r},\\ \overline{H}_m&=\int\bar{\xi}\bar{\sigma}^m\mathrm{d}\mathbf{r},\\ \int\rho\mathrm{d}\eta&=1.\end{aligned} \tag{2.55}$$

As a result, the maximization problem writes

$$\max\left\{S|\overline{E},\overline{I}_n,\overline{H}_m,\int\rho\mathrm{d}\eta=1\right\}. \tag{2.56}$$

A similar problem arises : an infinity of invariants come into play, which makes solutions not analytically solvable. This problem can be solved analytically if only a few constraints are accounted for. For instance, if I_1 and H_1 are considered exclusively, the maximization problem turns into

$$\max\left\{S|\overline{E},\overline{I}_1,\overline{H}_1,\int\rho\mathrm{d}\eta=1\right\}, \tag{2.57}$$

giving rise to the variational equation

$$\int\delta\left(-\rho\log\rho-\frac{\beta\rho}{2}\left(\bar{\xi}\psi+\frac{\eta^2}{r^2}\right)-\mu\bar{\xi}\rho\eta-\alpha\rho\eta-\zeta(\mathbf{r})(\rho-1)\right)\mathrm{d}\eta\mathrm{d}\mathbf{r}=0 \tag{2.58}$$

with β, μ, α and ζ Lagrangian multipliers. Taking the variation of Eq.(2.58) against ρ yields

$$-1-\log\rho-\frac{\beta}{2}\frac{\eta^2}{r^2}-\mu\bar{\xi}\eta-\alpha\eta-\zeta=0. \tag{2.59}$$

This leads then to the Gibbs state in axisymmetric turbulence :

$$\rho(\eta, \mathbf{r}) = \frac{1}{Z(\mathbf{r})} \exp\left(-\frac{\beta}{2}\frac{\eta^2}{r^2} - (\mu\overline{\xi} + \alpha)\eta\right), \tag{2.60}$$

where $Z(\mathbf{r})$ ensures the normalization of the integral of ρ against η. Equations connecting $\overline{\xi}$, ψ and $\overline{\sigma}$ can also be obtained : taking the variation of Eq.(2.58) against $\overline{\xi}$ yields

$$-\beta\psi - \mu\overline{\sigma} = 0 \Longleftrightarrow F(\psi) = -\frac{\beta}{\mu}\psi; \tag{2.61}$$

since Eq.(2.60) corresponds to a Gaussian distribution of σ, one can derive the expression of $\overline{\sigma}$:

$$\overline{\sigma} = -\frac{r^2}{\beta}(\mu\overline{\xi} + \alpha) \Longleftrightarrow G(\psi) = -\frac{\alpha}{\mu}. \tag{2.62}$$

Eq.(2.62) is considered, up to a Lagrangian multiplier α, as a Beltramized solution of the system meaning that there is an alignment between the velocity $\mathbf{u}$ and the vorticity $\boldsymbol{\omega}$.

However, it is theoretically proved in [22] that the critical solutions (2.61) and (2.62) are essentially saddle points of the system, and are linearly unstable facing some "optimal" perturbations consisting of special spectral modes. In practical scenarii, such perturbations can probably occur due to forcing or dissipation effects. Thus the stationary states predicted by Eqs.(2.61) and (2.62) might not survive after a sufficiently long period. But in reverse, these stationary states can be expected to exist during a certain length of time [22]. This expectation can be proved valid by the presence of big structures and the underlying functional relationships in numerical and experimental results discussed in the sequel.

Experimental and numerical results

In experiments of "axisymmetric" turbulence, the most important device is the "French washing machine" generating a von Kármán flow. Equipped with two counter-rotating impellers on top and bottom of the vessel, the device is essentially a cylindrical vessel with radius and a tunable height (distance between the impellers) to modify the aspect ratio. Each impeller is composed of a disc containing highly curved blades. Readers are suggested to refer to [20] for complementary details about the experimental setup. Under different rotation frequencies of the impellers, various flow regimes, with axisymmetric mean flows, are established with a Reynolds number varying from 10^2 to 3×10^5. Such a turbulent flow is only **statistically axisymmetric**.

Herbert *et al.* [23] carried out such experiments to clarify the energy cascade direction in axisymmetric flows. They find the scaling laws of the energy spectra were compatible with the fact that kinetic energy is mainly transferred to and concentrated in large scales of the order of the cylinder radius, revealing the existence of coherent structures. Monchaux *et al.* [21] performed von Kármán experiments with the purpose of seeing whether stationary out-of-equilibrium systems share any resemblance with classical equilibrium systems. In a test case at $\mathrm{Re} = 2.5 \times 10^5$, big circulating structures are observed in the poloidal plane, represented by either the time averaged velocity field or the most probable velocity field, showing that a stationary state is attained during the selected period. In their sequential experiments, the authors exclude 50% of the flow volume in the vicinity to the impellers and the lateral wall, and show that functional relashions similar to Eq.(2.49) are satisfied.

Surprisingly, the mean flow is therefore a solution of the (inviscid and unforced) Euler equations. They obtained cubic forms of the F function

$$F(\psi) = p_1\psi + p_3\psi^3 \tag{2.63}$$

for both mean and most probable fields, where p_1 and p_3 are prefixes depending on the Reynolds number. In each case, the corresponding F expression is used to deduce the G function which is then shown to be linear and around zero.

Direct numerical simulations of **strictly axisymmetric** turbulence are performed by Qu *et al.* [8, 7, 9]. By developing a fully spectral numerical method initially designed by Li *et al.* [24] for magnetohydrodynamics, the authors study both freely decaying and spectrally forced flows. One striking fact is that energy condensation and functional relationships are observed in decaying cases. In forced flows, a dual cascade where energy goes inversely to small wave-numbers and helicity goes forward to large wave-numbers is observed. However, the flows turn out to be less coherent in the presence of energy injection, probably due to the optimal perturbations induced by the applied spectral forcing.

Theoretical results of statistical mechanics of the Euler equations being verified by experiments of statistically axisymmetric turbulence, one of the goals of the current thesis is to try to reproduce the predictions of direct numerical simulations of strictly axisymmetric turbulence with higher Reynolds number. Two different numerical methods with confined boundaries will be used (see Chapter 3). Moreover, as stated in the beginning of this section, axisymmetric turbulence is a rich subject that is worth deeply looking into. Since it is an intermediate situation between two- and three-dimensional regimes, transition behaviors crossing from two-dimensionality to three-dimensionality, where the axisymmetric regime plays the role of a bridge, are of interest and deserve investigations. Concerning the dimensionality transition in hydrodynamics, theoretical results are summarized in the next section.

2.2 Transition behavior

Most phenomena in nature are three-dimensional. But sometimes when one dimension is contracted and becomes much less prominent than the other two, the geometry can be considered as two-dimensional, whereas some typical three-dimensional features may still survive at the same time. Atmospheric flows such as cyclones and ocean currents are good examples where two-dimensional properties can be recognized at large scales and three-dimensional properties can be observed at small scales. They are largely forced by gradients of solar heating simultaneously at scales smaller and larger than the layer thickness : vertical gradients cause three-dimensional convection whereas horizontal gradients drive planetary scale flows [25].

Under ideal circumstances — such as in theoretical deduction or numerical simulations — flows can be strictly two-dimensional, and it is also possible and interesting to inquire the flow behaviors by going from the two-dimensional to the three-dimensional limit. This is the purpose of the current section : we first succinctly revisit researches on the two-to-three dimensionality transitions in hydrodynamics (detailed reviews can be referred to Alexakis and Biferale [26] andPPouquet *et al.* [27]), and then shed light on two other kinds of dimensionality transitions which are the sujects of this thesis.

2.2.1 Dimensionality transition caused by thickness tuning in layer flows

Celani *et al.* [28] consider the three-dimensional Navier-Stokes system with periodic boundary conditions in all three directions. They impose a square geometry to x and y dimensions with a length of L_x, and at the same time a tunable length L_z to the z dimension. By continuously changing the thickness of L_z, a transition between two- and three-dimensionality can be reached. A stochastic Gaussian forcing is activated spatially only in the x and y directions and spectrally in a narrow band around wave-number k_f. Then, the authors find that even with a thin planar layer geometry of $L_z/L_x = 1/32$, a split cascade that conveys energy simultaneously to smaller and larger wave-numbers than k_f is established, and both the inverse and direct cascades are characterized by a scaling power law proportional to $-5/3$. This is intuitively comparable to atmospheric or oceanic flows : eddies whose scales are much larger than the layer thickness behave like a two-dimensional flow, while eddies much smaller than the layer thickness act in a three-dimensional manner. Further, their numerical data also reveal a tendency that when L_z is increased and gets close to the injection scale l_f, the inverse energy flux becomes negligible, leading to a conjecture for a critical aspect ratio above which the system yields a typical cascade of three-dimensional homogeneous isotropic turbulence.

The reliability of this conjecture is numerically reinforced by Benavides and Alexakis [29]. Coincidentally, Benavides and Alexakis consider also a thin layer flow with a tunable length in the z direction. In their study, the flow is modelled by a horizontal two-dimensional field in the x and y dimensions coupled to one single Fourier mode in the z dimension, corresponding to a drastic truncation in the vertical direction :

$$\mathbf{u}_{2\mathrm{D}}(t,x,y) = \begin{pmatrix} \dfrac{\partial \psi}{\partial y} \\ -\dfrac{\partial \psi}{\partial x} \\ 0 \end{pmatrix}, \quad \mathbf{u}_q(t,x,y,z) = \begin{pmatrix} v_x(x,y,t)\sin(qz) \\ v_y(x,y,t)\sin(qz) \\ v_z(x,y,t)\cos(qz) \end{pmatrix}. \tag{2.64}$$

In this model, $\mathbf{u}_{2\mathrm{D}}$ is the two-dimensional part of the system and $\mathbf{u}_q$ is the three-dimensional counterpart. $\psi(t,x,y)$ is the stream function that characterizes $\mathbf{u}_{2\mathrm{D}}$ in the (x,y) plane, meaning that $\mathbf{u}_{2\mathrm{D}}$ is incompressible since it is not difficult to find $\nabla\cdot\mathbf{u}_{2\mathrm{D}} = 0$. The parameter q determines the thickness H of the vertical direction : $H = \pi/q$. The incompressibility condition of $\mathbf{u}_q$ and the dynamic equations of the system are

$$\begin{aligned} &\frac{\partial \mathbf{u}_{2\mathrm{D}}}{\partial t} + \mathbf{u}_{2\mathrm{D}}\cdot\nabla\mathbf{u}_{2\mathrm{D}} = -\overline{\mathbf{u}_q\cdot\nabla\mathbf{u}_q} - \overline{\nabla P} + \nu\Delta\mathbf{u}_{2\mathrm{D}} - \mu\Delta^{-2}\mathbf{u}_{2\mathrm{D}} + \mathbf{F}, \\ &\frac{\partial \mathbf{u}_q}{\partial t} + \mathbf{u}_{2\mathrm{D}}\cdot\nabla\mathbf{u}_q = -\mathbf{u}_q\cdot\nabla\mathbf{u}_{2\mathrm{D}} - \nabla p_q + \nu\Delta\mathbf{u}_q, \end{aligned} \tag{2.65}$$

with overlines standing for averaging in the z direction, and P and p_q pressures for respectively the two- and three-dimensional parts. $\mathbf{F}$ is a two-dimensional forcing on (x,y) and is switched on at a scale of order l_f. By varying the height H from big to small values, the authors observe the energy cascade transition discovered by Celani *et al.* [28] : a transition that connects a unidirectional forward cascade and a bidirectional (simultaneously forward and inverse) cascade. As the layer thickness diminishes even more, a second transition that connects the bidirectional cascade and a unidirectional inverse cascade also appears. Therefore, two critical thicknesses of definite regime changes — $H_{3\mathrm{D}}$ and $H_{2\mathrm{D}}$ — are obtained. For $H > H_{3\mathrm{D}}$, the flow geometry consists of small scale vortex tubes in physical space, and the cascade is presented by a typical Kolmogorov energy spectrum at large wave-numbers. When H is smaller than but close to $H_{3\mathrm{D}}$, a slight inverse energy transfer begins to appear, and as H goes smaller but still larger than $H_{2\mathrm{D}}$, a more obvious inverse cascade is observed and a $k^{-5/3}$ scaling is recognized in both forward and backward inertial ranges. Large scale 2D coherent structures and small scale 3D vortex tubes coexist in physical space. These results largely conform with the findings in [28]. The only difference is that in this model, $H_{3\mathrm{D}}$ is not equivalent to the forcing scale l_f, but is about one-order smaller than l_f. For $H < H_{2\mathrm{D}}$, all three-dimensional contributions suffer an exponential decay as time advances, yielding a purely two-dimensional system along with an inverse energy cascade. For H larger than but close to $H_{2\mathrm{D}}$, the three-dimensional behavior is strongly intermittent. Last but not least, it is reported in their work that the changes of dimensionality taking place when H passes across $H_{3\mathrm{D}}$ and $H_{2\mathrm{D}}$ are rather continuous instead of an expected discontinuous way.

Similarly, experimental studies of the connection between dimensionality and cascade properties are performed in thin layer experiments. Such experiments were initially designed to reproduce almost two-dimensional strongly stratified flows (*e.g.* Sommeria [30], Flór and van Heijst [31]). More recently these experiments were used to investigate the transition from 2D to 3D flows. For example, Shats *et al.* [32] consider an electromagnetically driven layer flow, and present the dimensionality as the deviation of the viscous damping rate α compared to that predicted by quasi-two-dimensional model α_L. They find that in single electrolyte layers, the anomalous damping ratio of $a_D = \alpha/\alpha_L$ departs from 1 when the layer thickness-forcing scale ratio h/l_f is greater than 0.2, and that in the presence of a large-scale vortex, the departure of a_D from 1 takes place at $h/l_f = 0.04$, showing that the two-dimensionality seems to be easily broken as the layer gets slightly thicker. The authors suggest that as a_D becomes larger, the layer flow displays higher three-dimensionality. Further, they determine the energy cascade direction by measuring the third-order structure function S_3. They find that for small damping deviations, S_3 is positive and therefore indicates an inverse energy cascade expected in two dimensions; for larger damping deviations S_3 is negative, revealing a direct energy cascade associated with 3D dynamics. Thus, a relation between dimensionality and energy cascade direction is made. In the electromagnetically driven layer experiments conducted by Xia *et al.* [25], an even thicker layer of $h/l_f > 0.5$ exhibits a robust inverse energy cascade.

While the above investigations focus on the transition caused by continuously changing the geometry of thin layer flows, other investigations, which are more theoretical, aim at a more basic control of the dimensionality, as will be presented in the next subsection.

2.2.2 Dimensionality transition controlled by explicit parameters

One can notice that in the previous subsection, although sometimes the cases correspond to very thin layers, they are three-dimensional flows in a strict sense. It is interesting to see whether one can straightforwardly operate on the dimensionality of a flow, although this may appear abstract when the dimensionality is not an integer. Such ideas of non-integer dimensions originate in statistical mechanics and quantum field theory in parallel with the adaptation of non-integer dimensional mathematical tools.

There exist various theoretical examples such as the non-integer space-time dimension $d = 4 - \varepsilon$ [33] and the ε-expansion [34] in critical phenomena by Wilson *et al.*, the dimensional renormalization in quantum electrodynamics by Bollini and Giambiagi [35], the dimensional regularization method in quantum field theory [36] by 't Hooft and Veltman, *etc.* Regarding mathematical tools, the integration in non-integer dimensional space is proposed by Wilson [37], the generalization of scalar Laplacian operators (by Palmer and Stavrinou in [38]) as well as of other vector calculus (by Tarasov in [39]) to non-integer dimensions are suggested, in favor of theoretical studies on fractal media problems. The same idea is then inherited in theoretical investigations on hydrodynamics.

In fluid mechanics, one intuitive proposition is to directly embed the dimension d as a control parameter somehow into the governing equations of the system. The dimensionality is no more measured by the aspect ratio of geometries, but by the dimension parameter d instead. To achieve this, Frisch *et al.* [40] extend a second-order closure model of homogeneous isotropic turbulence, namely the eddy-damped quasi-normal Markovian approximation, into its arbitrary-dimension version where d is thus extended to non-integer values. The feasibility relies on related mathematical tools that allow, for example, the integration over "spherical" surface of non-integer dimension, the derivation of non-integer order, *etc.* The derivation of this model is out of the scope of this presentation. Readers interested in more details are recommended to refer to [41]. As a result, d appears explicitly in the final governing equations as a tunable parameter. Again, the energy cascade direction serves as a criterion to judge the dimensionality. Several findings can be cited from their work. First, a critical crossover dimension $d_c = 2.03$ at which the cascade direction reverses is given in [40]. Although in [41] d_c is declared to be 2.05, it is clear that using this adapted model, the dimensionality transition takes place at a point very close to the two-dimensionality limit. Second, by ruling out the viscous dissipation and energy injection and by assuming a $E(k) \propto k^{-m}$ scaling at the initial moment, they find that the solution with $m = 5/3$, corresponding to a Kolmogorov scaling, is stable for any $d \geqslant 2$. Third, situations with $d < 2$ are not realizable with this model. Indeed, the authors find that when $d < 2$, even when the energy spectrum is initially imposed to be positive, it usually (but not necessarily) drops to negative values after arbitrarily short time. Therefore, a methodology other than the EDQNM model is needed to consider non-integer dimensions smaller than 2.

For $d < 2$ and still in the context of homogeneous isotropic turbulence, Frisch *et al.* [42] conduct Fourier decimation operation to the velocity field, which consists in a quenched mode filtering process :

$$\mathbf{u}(\mathbf{x}) = \sum_{\mathbf{k}} \mathrm{e}^{\mathrm{i}\mathbf{k}\cdot\mathbf{x}} \theta_{\mathbf{k}} \hat{\mathbf{u}}_{\mathbf{k}}, \tag{2.66}$$

where $\theta_{\mathbf{k}}$ is a random number whose value is determined as

$$\begin{aligned} &\theta_{\mathbf{k}} = \begin{cases} 1 & \text{with probability } h_k \\ 0 & \text{with probability } 1 - h_k \end{cases}, \\ &k \equiv |\mathbf{k}|, \\ &h_k = C \left(\frac{k}{k_0} \right)^{d-2}. \end{aligned} \tag{2.67}$$

C is constant and is normally set as 1 in their study. k_0 is a reference wave-number corresponding to the largest scale of the system. The parameter d is the dimensionality and varies within the interval of $(0, 2]$. This process is inspired by the fact that in a sphere of radius k, the number of modes involved in the dynamics scales as k^d for large k [43]. When the number of triad interactions in the spectral space is decimated, the authors observe a critical dimension of $d_c = 4/3$ at which the $-5/3$ spectrum scaling begins to emerge. An inverse energy cascade is observed for $4/3 < d < 2$, and as d approaches 2, the range of the $-5/3$ scaling becomes wider. The Kolmogorov constant C_{Kol} that appears in the spectrum expression $E(k) = C_{\mathrm{Kol}} \varepsilon^{2/3} k^{-5/3}$ diverges as $(d-4/3)^{-2/3}$, revealing that $d_c = 4/3$ is in fact the cut-off dimension valid for this method.

At difference with the energy closure and Fourier decimation manners, Yakhot and Orszag [44] considered the possibility of extending the turbulence dimensionality by applying a renormalization group procedure. They also succeed in determining a critical dimensionality at which the energy flux sign changes, and find $d_c = 2.56$ for Kolmogorov flows. This shows that the value of d_c depends on what kind of models and hypotheses one adopts to approximate turbulence dynamics.

Another abstract way to control the dimensionality transition is studied by Giuliani *et al.* [45]. Instead of inserting explicitly the dimension d in equations, the authors choose to treat the problem from the angle of conserved quantities. When viscosity and forcing are not considered, the first conserved quantity is the kinetic energy, and the second one is the enstrophy in two-dimensional flows or the helicity in three-dimensional flows. They then use the Gledzer-Ohkitani-Yamada shell model [46, 47] without dissipation and energy injection :

$$\left(\frac{\partial}{\partial t} + \nu k_n^2\right) \hat{u}_n = \mathrm{i} k_n (a_n \hat{u}_{n+1}^* \hat{u}_{n+2}^* + \frac{b_n}{2} \hat{u}_{n-1}^* \hat{u}_{n+1}^* + \frac{c_n}{4} \hat{u}_{n-1}^* \hat{u}_{n-2}^*) + f_n. \tag{2.68}$$

This is a governing equation in the spectral space, assuming that each shell is coupled with the nearest and the next-nearest shells. Herein, $n = 1, \ldots, N$ is the shell number, $k_n = k_0 r^n$ is the shell wave-number, boundary conditions are set as $a_{N-1} = a_N = b_1 = b_N = c_1 = c_2 = 0$, and the superscript $*$ signifies data from the last time step. By assuming zero dissipation and forcing $\nu = f_n = 0$, the energy invariance $\sum_n |\hat{u}_n|^2 = C$ imposes $a_n + b_{n+1} + c_{n+2} = 0$. A simplified treatment is selected by letting $a_n = 1$, $b_n = \delta$ and $c_n = \delta - 1$. The second quantity can hence be expressed as

$$Q = \sum_n k_n^{\alpha} |\hat{u}_n|^2 \quad \text{with} \quad 2^{\alpha} = \frac{1}{\delta - 1}. \tag{2.69}$$

For a two-dimensional case, $\alpha = 2$ and $\delta = 5/4$, giving rise to $Q = Z = \sum_n k_n^2 |\hat{u}_n|^2$; when a three-dimensional case is desired, $\alpha = 1 + \mathrm{i}\pi/\ln 2$ and $\delta = 1/2$, yielding $Q = H = \sum_n (-1)^n k_n |\hat{u}_n|^2$. Therefore, by continuously varying δ from $1/2$ to $5/4$, the system passes from two-dimensionality to three-dimensionality. A critical value $\delta_c = 1$ is thus found at which the energy flux changes sign, but in a discontinuous way.

2.2.3 Dimensionality transition studied in the present thesis

In the present thesis, we investigate two kinds of dimensionality transitions, a concrete kind and an abstract kind. Both of them are related to axisymmetric turbulence in confined cylindrical configurations.

The concrete transition treats strictly axisymmetric flows, and considers the continuous change from non-swirling (weak toroidal energy component, thus purely 2D2C) regime to swirling (strong toroidal energy component, thus 2D3C) regime. This can be realized by controlling the energy injections in the toroidal and poloidal directions via a fully spectral method. Technical details of the numerical implementation are presented in Section 3.1.

The abstract transition focuses on passing from axisymmetric (azimuthal invariant) regimes to general three-dimensional (free azimuthal variation) regimes. Axisymmetric flows are mathematically described by the peculiarity of $\partial_\theta = 0$. However, they can also be described from another angle : for axisymmetric flows, the variation period in the azimuthal direction is $+\infty$. Similarly, general 3D flows retained in a cylinder can be considered as flows of which the azimuthal variation period is 2π. Then here comes an interesting question : What are flows with an azimuthal variation period between $+\infty$ and 2π ? If one looks into the dimensionless Navier-Stokes equations, one can find that such situations of intermediate periodicity can be fitted in a dimensionless cylinder. To illustrate this, we start from the three-dimensional Navier-Stokes equation under cylindrical coordinates. As is normally done, one can normalize the equations by using characteristic quantities of time τ, length L and velocity U. The idea is that instead of defining one universal length scales to feature structure sizes of the flow, we choose two different scales L_P and L_T to respectively characterize variation lengths for poloidal and toroidal components. By fixing $r = L_P\bar{r}$ and $z = L_P\bar{z}$ in the poloidal direction, one has $\partial_r = (1/L_P)\partial_{\bar{r}}$ and $\partial_z = (1/L_P)\partial_{\bar{z}}$. With L_T in the toroidal direction, one has : $r\theta = L_T\overline{(r\theta)} = L_T\bar{r}\bar{\theta}$. Thus, the azimuthal derivative terms are rewritten as $(1/r)\partial_\theta = (1/L_T)(1/\bar{r})\partial_{\bar{\theta}}$. In the Navier-Stokes equations with length normalized only, a ratio L_P/L_T appears in azimuthal derivative terms. It can be further reduced into one single control parameter :

$$\alpha = \frac{L_P}{L_T}. \tag{2.70}$$

This leads to the three-dimensional Navier-Stokes equations written as :

$$\begin{aligned}
&\frac{\partial u_r}{\partial r} + \frac{u_r}{r} + \frac{1}{r}\alpha\frac{\partial u_\theta}{\partial\bar{\theta}} + \frac{\partial u_z}{\partial z} = 0,\\
&\frac{\partial u_r}{\partial t} + u_r\frac{\partial u_r}{\partial r} + \frac{u_\theta}{r}\alpha\frac{\partial u_r}{\partial\bar{\theta}} + u_z\frac{\partial u_r}{\partial z} - \frac{\bar{u}_\theta^2}{r}\\
=&-\frac{1}{\rho}\frac{\partial p}{\partial r} + \nu\left(\frac{\partial^2 u_r}{\partial r^2} + \frac{1}{r}\frac{\partial u_r}{\partial r} + \frac{1}{r^2}\alpha^2\frac{\partial^2 u_r}{\partial\bar{\theta}^2} + \frac{\partial^2 u_r}{\partial z^2} - \frac{u_r}{r^2} - \frac{2}{r^2}\alpha\frac{\partial u_\theta}{\partial\bar{\theta}}\right),\\
&\frac{\partial u_\theta}{\partial t} + u_r\frac{\partial u_\theta}{\partial r} + \frac{u_\theta}{r}\alpha\frac{\partial u_\theta}{\partial\bar{\theta}} + u_z\frac{\partial u_\theta}{\partial z} + \frac{u_r u_\theta}{r}\\
=&-\frac{1}{\rho}\frac{1}{r}\frac{\partial p}{\partial\bar{\theta}} + \nu\left(\frac{\partial^2 u_\theta}{\partial r^2} + \frac{1}{r}\frac{\partial u_\theta}{\partial r} + \frac{1}{r^2}\alpha^2\frac{\partial^2 u_\theta}{\partial\bar{\theta}^2} + \frac{\partial^2 u_\theta}{\partial z^2} + \frac{2}{r^2}\alpha\frac{\partial u_r}{\partial\bar{\theta}} - \frac{u_\theta}{r^2}\right),\\
&\frac{\partial u_z}{\partial t} + u_r\frac{\partial u_z}{\partial r} + \frac{u_\theta}{r}\alpha\frac{\partial u_z}{\partial\bar{\theta}} + u_z\frac{\partial u_z}{\partial z}\\
=&-\frac{1}{\rho}\frac{\partial p}{\partial z} + \nu\left(\frac{\partial^2 u_z}{\partial r^2} + \frac{1}{r}\frac{\partial u_z}{\partial r} + \frac{1}{r^2}\alpha^2\frac{\partial^2 u_z}{\partial\bar{\theta}^2} + \frac{\partial^2 u_z}{\partial z^2}\right).
\end{aligned} \tag{2.71}$$

One notices that there is a mapping $\theta \in [0, 2\pi/\alpha] \mapsto \bar{\theta} \in [0, 2\pi]$ in Eq.(2.71). The limit $\alpha = 0$ corresponds to the situation of $L_T \to \infty$, standing for an infinitely large azimuthal period, and matches thus the strictly axisymmetric regime ; in the other limit $\alpha = 1$, one has $L_P = L_T$ and the general three-dimensional regime with a 2π azimuthal periodicity is recovered. By this means, extension can be made to situations of $\alpha > 1$, this represents some kind of vibratory regime in the azimuthal direction, but this is out of the scope of the current thesis. By continuously varying the value of α from 0 to 1, a transition from the axisymmetric to the general three-dimensional regime can be realized.

To our knowledge, this is the first time that these two kinds of transitions are investigated. Results and analyses will be presented in Chapter 5 for the transition from axisymmetric non-swirling to swirling (2D2C⟶2D3C) regime, and in Chapter 6 for the transition from axisymmetric to general three-dimensional (2D3C⟶3D3C) regime. In this thesis, some techniques reminiscent of early RANS models are used to model the transitions. A summary of principles of these models is given in the next section.

2.3 Statistical modelling of turbulence

RANS equations for the mean velocity are not directly solvable due to the unclosed Reynolds stress $\langle u_i' u_j' \rangle$ with u_i' and u_j' velocity fluctuations in the i and j directions (in a Cartesian representation). Hence a closure should be formulated somehow by modelling $\langle u_i' u_j' \rangle$. Turbulent-viscosity models of the Reynolds stress are based on the turbulent-viscosity hypothesis put forward by Boussinesq in the 19th century :

$$\langle u_i' u_j' \rangle = \frac{2}{3} k \delta_{ij} - \nu_T \left(\frac{\partial U_i}{\partial x_j} + \frac{\partial U_j}{\partial x_i} \right), \tag{2.72}$$

with k the turbulent energy, δ_{ij} the Kronecker symbol, ν_T the turbulent viscosity (or eddy viscosity), U_i and U_j mean velocity components in related directions, and x_i and x_j corresponding coordinates. The turbulent viscosity ν_T is considered to be the product of a specific velocity u^* and a specific length l^* :

$$\nu_T = u^* l^*. \tag{2.73}$$

Within the frame of the turbulent-viscosity hypothesis, we need to approximate these u^* and l^* as well as some other quantities. The logic is that once u^* and l^* specified, ν_T is obtained and $\langle u_i' u_j' \rangle$ can be calculated according to Eq.(2.72), so the RANS equations for the mean velocity field can be solved. We focus here on three kinds of models

1. **Algebraic models**, among which the mixing-length model is the most representative. The mixing-length model was devised by Prandtl for two-dimensional boundary-layer flows, who considered that the mixing-length $l^* = l_m$ is analogue to the molecular free path. Besides, it was assumed that the specific velocity is the product of the mixing length and the absolute value of averaged stream-wise velocity gradient. This gives

   $$\nu_T = u^* l^* = l_m^2 \left| \frac{\partial U}{\partial y} \right|. \tag{2.74}$$

   Later, some developments of this model to fit three-dimensional flows were suggested by Smagorinsky [48] basing u^* on the mean strain rate and by Baldwin and Lomax [49] basing u^* on the mean rotation rate, with the latter widely used in industrial applications.

2. **Turbulent-kinetic-energy model**. Still, l^* in this model was taken as the mixing length l_m, but u^* was modelled in another manner as

   $$u^* = c k^{1/2}, \quad \Longrightarrow \quad \nu_T = c k^{1/2} l_m, \tag{2.75}$$

with c a model constant. This model was separately proposed by Kolmogorov [50] and Prandtl [51], and is termed as "one-equation model" since there remains the turbulent kinetic energy k to be modelled through its transport equation. Each term (production, diffusion and dissipation) in this transport equation was modelled as a function of l_m and k, thus making the whole turbulent-viscosity model solvable. Especially, the dissipation rate ε was simply considered to scale as $k^{3/2}/l_m$. However, later extensions of turbulent-viscosity model required that apart from k, ε should be modelled by its own transport equation, giving rise to the k-ε model.

3. **k-ε model**. This is a kind of "two-equation model" : the same l_m and k modelling as above are kept in this model ; an additional modelling process is imposed for the dissipation rate ε using its transport equation. However, the exact transport equation of ε possesses eight terms to approximate. Consequently, the transport equation of ε was empirically simplified by terms representing its diffusion, production and dissipation mechanisms.

Turbulent-viscosity models assume that the Reynolds-stress depends on the local values of k, ε and $\partial U_i/\partial x_j$, which is questionable in regions of strong inhomogeneity. Therefore, corrections such as those for near-wall regions [52, 53] and low-Re [54] were proposed. Besides, other proposals such as deriving and modelling the transport equation of ν_T [55] were intended but merely for aerodynamic applications. Otherwise, some fundamental changes of the turbulent-viscosity model (2.72) was performed, with the Reynolds-stress developed to the second order approximation, but still based on the modelling of k and ε [56]. Thus derived was the non-linear k-ε model with improved performance and applicability compared to the standard k-ε model.

In parallel with turbulent-viscosity models, another kind of Reynolds-stress model aims at modelling the transport equation of $\langle u'_i u'_j \rangle$. However, with such a principle, the modelling of the Reynolds-stress flux, the pressure-strain-rate correlation and the dissipation tensor are needed, with a tremendous diversity of proposals to be found in the literature. In Chapter 5 for example, we illustrate the form of the pressure strain correlation proposed by Hanjalić and Launder [57], since we will use its form to model the transitions in axisymmetric turbulence.

Different Reynolds-stress models having their own advantages, shortcomings and suitable application range, they provide a basis of reference for modelling trials of various other cases. Particularly, during the establishment of the models in this thesis, some ideas will be borrowed from these RANS models through analogy of situations, mechanisms, *etc.*

Chapitre 3

Numerical Methods

Two kinds of numerical methods will be introduced in this chapter, the first being fully spectral and the second being pseudo-spectral. Both methods integrate the Navier-Stokes equations in a confined cylindrical vessel. They differ in boundary conditions. In general, the no-penetration condition is valid for both methods, but the no-slip condition is applied strictly in the pseudo-spectral method only. The sketch of the flow domain is given in Fig.3.1. Various domain aspect ratios can be considered by imposing different values of the radius R and height H.

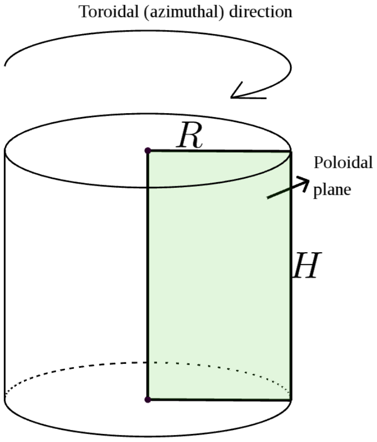

Figure 3.1: Sketch of the computational domain.

Qu *et al.* [7, 8, 9] were the first to numerically investigate strictly axisymmetric turbulence. For this, they used a fully spectral method. In their simulations, the upper and lower bounds of the vessel are open by setting periodic conditions to them, and a partial slip is allowed on the lateral wall. To follow this work, we decide to add gradually the restrictions comparable to realistic experimental set-ups. Therefore, the first part of simulations, using the fully spectral method, focuses on simulations with partial slip but totally confined boundaries, and the second part of simulations, using a pseudo-spectral method, on simulations with more realistic (no-slip) boundaries.

3.1 The fully spectral method (FSM)

The main idea of spectral methods is to use an orthonormal basis to decompose the velocity and the pressure fields. As one will notice, the current fully spectral method (FSM) consists actually in a Galerkin-type approximation : the basis satisfies naturally the wished boundary conditions. The advantage of fully spectral methods is that the derivations are calculated in their spectral form which are analytical and accurate. However, the disadvantage, as one will see in the sequel, is that the nonlinear term will occupy a large amount of computational resources. To illustrate these two points as well as other specialties, this section gives the details of the theoretical derivation and the numerical implementation of the method. Initially devised by Chen *et al.* [10] for magnetohydrodynamics in cylindrical domain, the code was later developed by Li *et al.* [58] for 2D turbulence with circular boundaries, and then adapted to axisymmetric turbulence by Qu [8].

3.1.1 Eigenfunction of the curl

The basis of our FSM is derived from the eigenfunctions of the curl operator under cylindrical coordinates, inspired by the work of Montgomery *et al.* [59, 10, 60] and Chandrasekhar and Kendall (CK) [61] on magnetohydrodynamic (MHD) flows.

These eigenfunctions of the curl operator can form an orthonormal basis to expand divergence-free vector fields under cylindrical coordinates, therefore including incompressible velocity fields, up to certain symmetries and boundary conditions. The expansion can basically be written as

$$\mathbf{u}(r,\theta,z,t)=\sum_{qmn}\xi_{qmn}(t)\mathbf{A}_{qmn}(r,\theta,z), \tag{3.1}$$

where ξ_{qmn} are called CK mode coefficients with q, m, n mode numbers of r, θ, z dimensions respectively, and $\mathbf{A}_{qmn}$ is the basis depending on CK eigenfunctions :

$$\mathbf{A}_{qmn}=I_{qmn}^{-\frac{1}{2}}\left[\lambda_{qmn}\nabla\Psi_{qmn}\times\mathbf{e_z}+\nabla\times(\nabla\Psi_{qmn}\times\mathbf{e_z})\right], \tag{3.2a}$$

$$(\nabla^2+\lambda_{qmn}^2)\Psi_{qmn}=0. \tag{3.2b}$$

A first remark is that ξ_{qmn} and $\mathbf{A}_{qmn}$ are generally complex, since Ψ_{qmn} can possibly be complex functions. Imposing some extra constraints, they can be restricted to be in the real number space purely. Without loss of generality, the inner product here is defined as the average of the integral over the cylinder volume :

$$\langle\mathbf{A}_1(r,\theta,z),\mathbf{A}_2(r,\theta,z)\rangle=\frac{1}{V}\int_V\mathbf{A}_1(r,\theta,z),\mathbf{A}_2^*(r,\theta,z)r\mathrm{d}r\mathrm{d}\theta\mathrm{d}z, \tag{3.3}$$

where $\mathbf{A}_1$ and $\mathbf{A}_2$ are two vectors belonging to the CK basis, V is the volume, and the superscript symbol $*$ denotes the conjugate of a complex field. In this context, the prefix $I_{qmn}^{-1/2}$ in Eq.(3.2a) is a coefficient ensuring that the CK basis is normalized :

$$\frac{1}{V}\int_V\mathbf{A}_{qmn}\mathbf{A}_{qmn}^*r\mathrm{d}r\mathrm{d}\theta\mathrm{d}z=1. \tag{3.4}$$

A second remark is that $\mathbf{A}_{qmn}$ is divergence-free. Thus the velocity field, expanded in the form (3.1), meets naturally the incompressibility condition :

$$\nabla\cdot\mathbf{u}=0. \tag{3.5}$$

A third remark, resulting from the second one, is that all $\mathbf{A}_{qmn}$ vectors are eigenfunctions of the curl : $\nabla\times\mathbf{A}_{qmn}=\lambda_{qmn}\mathbf{A}_{qmn}$. One can then deduce the expression of the vorticity field $\boldsymbol{\omega}$, curl of $\mathbf{u}$, without lots of difficulty :

$$\boldsymbol{\omega}(r,\theta,z,t)=\sum_{qmn}\lambda_{qmn}\xi_{qmn}(t)\mathbf{A}_{qmn}(r,\theta,z). \tag{3.6}$$

Moreover, this virtue can lead to the simplicity of the spectral expression of the Navier-Stokes equations, as will be shown in Section 3.1.3.

The concrete expressions of $\mathbf{A}_{qmn}$ depending on detailed symmetries and boundary conditions will be developed in the next subsection.

3.1.2 Expressions of CK basis for axisymmetric flows confined in a closed cylindrical domain

We aim at imposing the axisymmetry condition : $\partial_\theta = 0$. Then the expression of CK basis of the current thesis originates in solving the Helmholtz equation (3.2b), except that the mode index m must be excluded. Like solving the Laplace equation, the variable separation approach is adopted assuming that the solutions can be written as

$$\Psi_{qn}(r,z) = R(r)Z(z), \tag{3.7}$$

where R and Z are scalar functions of r and z. This develops Eq.(3.2b) into

$$\frac{R''}{R} + \frac{1}{r}\frac{R'}{R} + \lambda_{qn}^2 = -\frac{Z''}{Z}. \tag{3.8}$$

As the left-hand side of Eq.(3.8) is a function of r and the right-hand side of z, they must be reduced to a constant independent from both r and z, denoted as α_{qn}, giving

$$R'' + \frac{1}{r}R' + (\lambda_{qn}^2 - \alpha_{qn})R = 0, \tag{3.9a}$$

$$Z'' + \alpha_{qn}Z = 0. \tag{3.9b}$$

Notice that Eq.(3.9b) is the harmonic oscillation equation if α_{qn} is chosen positive. The corresponding solutions on z are periodic, or say trigonometric functions reflecting to Fourier modes. Thus we prefer to denote $\alpha_{qn} = k_n$ conventionally, which is reminiscent of Fourier wave-numbers. Solutions are then well known as

$$Z(z) = Ae^{\mathrm{i}k_n z} + Be^{-\mathrm{i}k_n z} \tag{3.10}$$

with A and B complex constants. Return to the equation concerning r. Choices are that $\lambda_{qn}^2 - \alpha_{qn}^2 = \lambda_{qn}^2 - k_n^2 > 0$, making Eq.(3.9a) the 0th order Bessel differential equation of the first kind. With $\lambda_{qn}^2 - k_n^2 = \gamma_q^2$, solutions are then well known as

$$R(r) = CJ_0(\gamma_q r), \tag{3.11}$$

where J_0 is the 0th order Bessel function of the first kind and C is a constant. By substituting Eqs.(3.10) and (3.11) in Eq.(3.7), one obtains a first form of Ψ_{qn} :

$$\Psi_{qn} = J_0(\gamma_q r)(Ae^{\mathrm{i}k_n z} + Be^{-\mathrm{i}k_n z}). \tag{3.12}$$

Further reduction of this expression needs the definition of boundary conditions in the z direction. For instance, Qu *et al.* [8, 7, 9] considered periodic boundaries on the z dimension and set $A = 0$, giving rise to

$$\Psi_{qn} = J_0(\gamma_q r)e^{-\mathrm{i}k_n z}. \tag{3.13}$$

Since a confinement with no-penetration (slipping is allowed) condition on top and bottom is in our consideration, we pose $A = a + b\mathrm{i}$ and $B = -a - b\mathrm{i}$ to obtain

$$\Psi_{qn} = J_0(\gamma_q r)\sin(k_n z). \tag{3.14}$$

We notice that Ψ_{qn} is no longer a mapping to the complex number space. As a result, the derived CK basis is a set of vector fields in the real number space, accompanied by real expansion coefficients.

In order to distinguish this expansion in the real number space from its general complex form, it will be denoted subsequently as

$$\mathbf{u}(r,z,t) = \sum_{qn} C_{qn}(t)\mathbf{B}_{qn}(r,z), \tag{3.15}$$

where $\mathbf{B}_{qn}$ is the basis in the real number space and C_{qn} is the related real coefficient. By substituting Eq.(3.14) in Eq.(3.2a), one obtains the final expression of the basis :

$$\mathbf{B}_{qn}(r,z) = I_{qn}^{-\frac{1}{2}} \begin{pmatrix} -k_n\gamma_q J_1(\gamma_q r)\cos(k_n z) \\ \lambda_{qn}\gamma_q J_1(\gamma_q r)\sin(k_n z) \\ \gamma_q^2 J_0(\gamma_q r)\sin(k_n z) \end{pmatrix}, \tag{3.16a}$$

$$\Longrightarrow \mathbf{u}(r,z,t) = \sum_{qn} C_{qn}(t) I_{qn}^{-\frac{1}{2}} \begin{pmatrix} -k_n\gamma_q J_1(\gamma_q r)\cos(k_n z) \\ \lambda_{qn}\gamma_q J_1(\gamma_q r)\sin(k_n z) \\ \gamma_q^2 J_0(\gamma_q r)\sin(k_n z) \end{pmatrix}, \tag{3.16b}$$

$$\Longrightarrow \boldsymbol{\omega}(r,z,t) = \sum_{qn} \lambda_{qn} C_{qn}(t) I_{qn}^{-\frac{1}{2}} \begin{pmatrix} -k_n\gamma_q J_1(\gamma_q r)\cos(k_n z) \\ \lambda_{qn}\gamma_q J_1(\gamma_q r)\sin(k_n z) \\ \gamma_q^2 J_0(\gamma_q r)\sin(k_n z) \end{pmatrix}. \tag{3.16c}$$

Similarly, I_{qn} is the normalization constant guaranteeing :

$$\frac{1}{V}\int_V \mathbf{B}_{qn}\cdot\mathbf{B}_{qn}\mathrm{d}V = 1, \tag{3.17}$$

and its expression will be deduced in Appendix A.1. The determination of parameters γ_q and k_n remain to be done.

γ_q is determined by imposing the no-penetration boundary condition on the lateral wall at $r = R$ with R now the cylinder radius :

$$u_r(r=R,z) = \sum_{qn} C_{qn}(t) I_{qn}^{-\frac{1}{2}} \left(-k_n\gamma_q J_1(\gamma_q R)\cos(k_n z)\right) = 0. \tag{3.18}$$

We then share the same approach as Qu [8] which imposes that $J_1(\gamma_q R)$ is zero for all q modes. γ_q is therefore the qth root of equation $J_1(Rx) = 0$, and should actually be strictly positive. As a result, the q modes will be counted starting from 1 : $q = 1,2,3,...$, representing the qth strictly positive zero of $J_1(Rx)$.

Generally, λ_{qn} and k_n should take both positive and negative values. For the case where the z direction is treated periodically, $n = 0, \pm1, \pm2, \pm3, ...$ with $k_n = 2n\pi/H$ where H is the cylinder height, and both positive and negative λ_{qn} should be considered. The orthogonality and the completeness of the CK basis thus derived are theoretically demonstrated by Yoshida *et al.* [62, 63, 64]. To fulfill the completeness of our basis (3.16a), both positive and negative λ_{qn} should similarly be considered, but differences are that k_n should be chosen as

$$k_n = n\pi/H \quad \text{with} \quad n = 1,2,3,... \tag{3.19}$$

We then rewrite the expansion (3.15) as

$$\begin{aligned}\mathbf{u}(r,z,t) &\equiv \sum_{qn}^{\pm\lambda} C_{qn}(t)\mathbf{B}_{qn}(r,z)\\ &\equiv \sum_{qn}^{+\lambda} C_{qn}(t)\mathbf{B}_{qn}(r,z) + \sum_{qn}^{-\lambda} C_{qn}(t)\mathbf{B}_{qn}(r,z)\\ &\equiv \sum_{qn} C_{qn}^{+\lambda}(t)\mathbf{B}_{qn}^{+\lambda}(r,z) + \sum_{qn} C_{qn}^{-\lambda}(t)\mathbf{B}_{qn}^{-\lambda}(r,z),\end{aligned} \tag{3.20}$$

where r varies from 0 to R, and z varies from 0 to H. We introduce the notation $\sum_{qn}^{\pm\lambda}$ to represent a summing over qn series of both positive and negative λ, and the notation $C_{qn}^{+\lambda}\mathbf{B}_{qn}^{+\lambda}$ (respectively $C_{qn}^{-\lambda}\mathbf{B}_{qn}^{-\lambda}$) refers to the terms on the side of $+\lambda$ (respectively $-\lambda$). Using this notation, the poloidal stream function ψ, the angular momentum σ and the pseudo-vorticity ω have their analytically expanded form as

$$\begin{aligned}\psi(r,z) &= -r\int u_r(r,z)\mathrm{d}z\\ &= r\sum_{qn}^{\pm\lambda} C_{qn} I_{qn}^{-1/2}\gamma_q J_1(\gamma_q r)\sin(k_n z),\end{aligned} \tag{3.21a}$$

$$\sigma(r,z) = r u_\theta(r,z) = r\sum_{qn}^{\pm\lambda} C_{qn} I_{qn}^{-1/2}\lambda_{qn}\gamma_q J_1(\gamma_q r)\sin(k_n z), \tag{3.21b}$$

$$\xi(r,z) = \frac{\omega_\theta}{r} = \frac{1}{r}\sum_{qn}^{\pm\lambda} C_{qn} I_{qn}^{-1/2}\lambda_{qn}^2\gamma_q J_1(\gamma_q r)\sin(k_n z). \tag{3.21c}$$

A first remark is that the basis $\mathbf{B}_{qn}$ satisfies the divergence-free condition as mentioned before, resulting in the natural satisfaction of the incompressibility condition $\nabla\cdot\mathbf{u} = 0$. Besides, one can notice that under $\mathbf{B}_{qn}$, u_θ is zero on all boundaries and on the axis of $r = 0$. However, since $J_0(\gamma_q R) \neq 0$, $u_z \neq 0$ on the lateral wall. The slip of u_z is therefore allowed on this wall. Similarly, the slip of u_r is allowed on the top and the bottom of the cylinder since $\cos(0) = \cos(k_n H) = 1 \neq 0$, but one has $u_r = 0$ on $r = 0$. Finally, penetration is strictly prohibited on all wall boundaries. The axis of $r = 0$ is in fact a location of singularity for our system. In the presence of axisymmetry, u_r and u_θ should be strictly 0 on $r = 0$, which is an additional boundary condition well satisfied by $\mathbf{B}_{qn}$.

Numerical verification of the completeness of $\mathbf{B}_{qn}$

Mathematical demonstration of the orthonormality and the completeness of $\mathbf{B}_{qn}$ under these boundary conditions is given in Appendix A, while numerical verifications of this completeness will be introduced in this paragraph. The principle is to decompose velocity fields in the spectral space and then to recompose them back in the physical space. The qualitative comparison consists in visualizing whether the original fields are identical to the recomposed ones, while quantitively, relative errors between original and recomposed energy will be compared : $\mathrm{Err} = (E_{\text{original}} - E_{\text{recomposed}})/E_{\text{original}}$. Testing cases are shown in Tab.3.1. Visualization comparisons are presented in Fig.3.2. From Tab.3.1, one can see that for Case 1, the resolution of $(q_{\max}, n_{\max}) = (52, 45)$ is sufficient, and the fields are well recovered with high accuracy. As Case 2 contains much higher-order frequencies in the axial direction, a truncation of $q_{\max} = 45$ in the z dimension is no longer sufficient ($\mathrm{Err} = 1.57\%$). But if $q_{\max}$ is raised to a sufficiently high value, like $q_{\max} = 225$ in

Case 3, the relative error decreases again to a negligible level. These testing results then numerically prove the completeness of the basis $\mathbf{B}_{qn}$.

Case	1	2	3
$\psi(r,z) =$	$\sin^2(\frac{2\pi z}{H})(r-R)^3r^2$	$P_{10}(\frac{z}{H/2}-1)(r-R)^3r^2$	$P_{10}(\frac{z}{H/2}-1)(r-R)^3r^2$
$u_\theta(r,z) =$	$\sin^3(\frac{2\pi z}{H})(r-R)^2r$	0	0
$(q_{\max}, n_{\max}) =$	$(52,45)$	$(52,45)$	$(52,225)$
$E_{\text{original}} =$	2.04783636×10^1	1.19498710×10^2	1.19498710×10^2
$E_{\text{recomposed}} =$	2.04780028×10^1	1.17624925×10^2	1.19482179×10^2
$\text{Err} =$	1.76188811×10^{-5}	1.56803790×10^{-2}	1.38336538×10^{-4}

TABLE 3.1: Testing cases verifying the completeness of $\mathbf{B}_{qn}$. P_{10} is the 10th-order Legendre polynomial.

3.1.3 Spectral form of the Navier-Stokes equation

Using the CK basis $\mathbf{B}_{qn}$, we know that the velocity field $\mathbf{u}$ meets analytically the incompressibility condition. Therefore, $\nabla\cdot\mathbf{u}$ is no longer within our consideration in the sequel, and we are going to focus only on the dynamics of the system, of which the spectral form can be derived via $\mathbf{B}_{qn}$. The derivation begins with a reformulation of the Navier-Stokes equation :

$$\frac{\partial\mathbf{u}}{\partial t} = \mathbf{u}\times\boldsymbol{\omega} - \frac{1}{\rho}\nabla p_{\mathrm{t}} + \nu\nabla^2\mathbf{u}, \tag{3.22}$$

where $\boldsymbol{\omega} = \nabla\times\mathbf{u}$ is the vorticity vector, and $p_{\mathrm{t}} = p + \rho\mathbf{u}^2/2$ is the total pressure. Then one carries out inner product operation (3.3) between Eq.(3.22) and a certain basis vector $\mathbf{B}_{qn}$, assuming that the velocity field is decomposed as in Eq.(3.16b), which leads to the presence of the expansion constant C_{qn} on the left-hand side of the equation :

$$\frac{\partial}{\partial t}C_{qn} = \frac{1}{V}\int_V \mathbf{B}_{qn}\cdot\left[(\mathbf{u}\times\boldsymbol{\omega}) - \frac{1}{\rho}\nabla p_{\mathrm{t}} + \nu\nabla^2\mathbf{u}\right]\mathrm{d}V. \tag{3.23}$$

The reason of the reformulation (3.22) resides in the fact that the pressure term disappears after the integration :

$$\int_V \mathbf{B}_{qn}\cdot\nabla p_{\mathrm{t}}\mathrm{d}V = \int_V \nabla(p_{\mathrm{t}}\mathbf{B}_{qn})\mathrm{d}V - \int_V p_{\mathrm{t}}\nabla\cdot\mathbf{B}_{qn}\mathrm{d}V = 0. \tag{3.24}$$

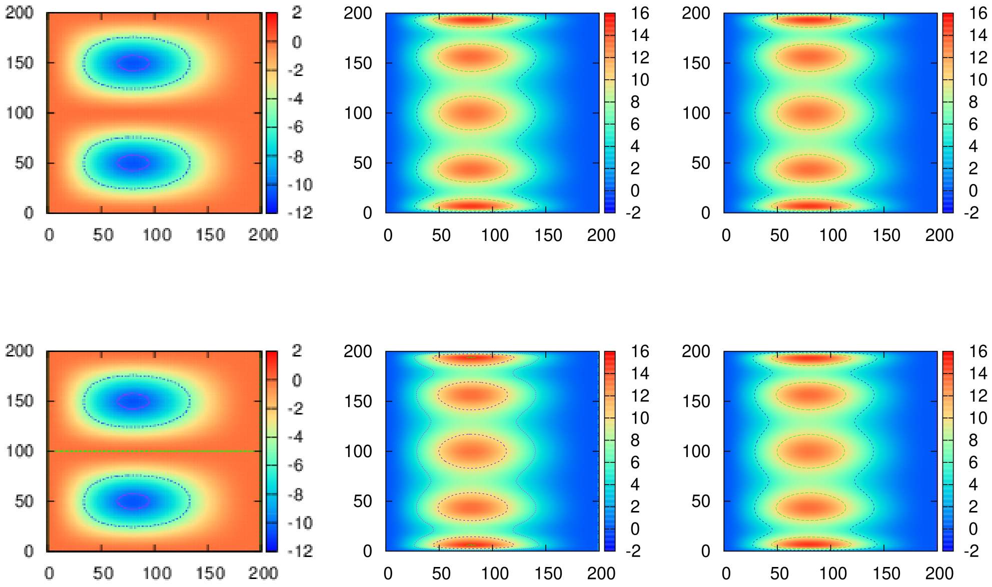

(a) Case 1. (b) Case 2. (c) Case 3.

FIGURE 3.2: Comparison of the stream function ψ in the three cases detailed in Tab.3.1. With naked eye, original (top) and recomposed (bottom) fields show no difference for Cases 1 and 3, while they are slightly different close to the top and bottom of the cylinder for Case 2 due to insufficiency of vertical resolution.

The first term on the right-hand side of Eq.(3.24) is zero, since by applying Green's formula, one has

$$\int_V \nabla(p_{\mathrm{t}}\mathbf{B}_{qn})\mathrm{d}V = \int_{\partial V}(p_{\mathrm{t}}\mathbf{B}_{qn})\cdot\mathbf{n}\mathrm{d}S = 0. \tag{3.25}$$

Recall that the radial component of $\mathbf{B}_{qn}$ on the lateral wall equals to zero, and so does the axial component on the top and the bottom boundaries. The second term on the right-hand side of Eq.(3.24) vanishes since the CK basis is naturally divergence-free. This emphasizes one of the advantages of using the CK basis : there is no need to treat explicitly the pressure term. Another advantage refers to the treatment of the viscous term :

$$\begin{aligned}\nabla^2\mathbf{u} &= \nabla(\underbrace{\nabla\cdot\mathbf{u}}_{0}) - \nabla\times\nabla\times\mathbf{u} \\ &= -\sum_{qn}^{\pm\lambda}\lambda_{qn}^2 C_{qn}\mathbf{B}_{qn},\end{aligned} \tag{3.26}$$

knowing that all $\mathbf{B}_{qn}$ are eigenvectors of the curl. Therefore, the Navier-Stokes equation reduces to :

$$\begin{aligned}\frac{\partial}{\partial t}C_{qn}^{+\lambda} &= \sum_{q_1n_1}^{\pm\lambda}\sum_{q_2n_2}^{\pm\lambda}\lambda_{q_2n_2}C_{q_1n_1}C_{q_2n_2}\left[\frac{1}{V}\int_V \mathbf{B}_{qn}^{+\lambda}\cdot(\mathbf{B}_{q_1n_1}\times\mathbf{B}_{q_2n_2})\,\mathrm{d}V\right] - \nu\lambda_{qn}^2 C_{qn}^{+\lambda}, \\ \frac{\partial}{\partial t}C_{qn}^{-\lambda} &= \sum_{q_1n_1}^{\pm\lambda}\sum_{q_2n_2}^{\pm\lambda}\lambda_{q_2n_2}C_{q_1n_1}C_{q_2n_2}\left[\frac{1}{V}\int_V \mathbf{B}_{qn}^{-\lambda}\cdot(\mathbf{B}_{q_1n_1}\times\mathbf{B}_{q_2n_2})\,\mathrm{d}V\right] - \nu\lambda_{qn}^2 C_{qn}^{-\lambda}.\end{aligned} \tag{3.27}$$

One can see that essentially, the numerical method consists in simulating the time evolution of C_{qn}. However, the first term on the right-hand side of the spectral equations, called the convolution term, complicates the procedure. Here we give the full expression of the integral $\frac{1}{V}\int_V \mathbf{B}_{qn}^{\pm\lambda} \cdot (\mathbf{B}_{q_1n_1} \times \mathbf{B}_{q_2n_2})\, \mathrm{d}V$:

$$\begin{aligned}
&\frac{1}{V}\int_V \mathbf{B}_{qn}^{\pm\lambda} \cdot (\mathbf{B}_{q_1n_1} \times \mathbf{B}_{q_2n_2})\, \mathrm{d}V = \frac{1}{V}\int_{z=0}^{H}\int_{\theta=0}^{2\pi}\int_{r=0}^{R} r\mathrm{d}r\mathrm{d}\theta\mathrm{d}z I_{qn}^{-\frac{1}{2}} I_{q_1n_1}^{-\frac{1}{2}} I_{q_2n_2}^{-\frac{1}{2}} \\
&\{\cos(k_n z)\sin(k_{n_1}z)\sin(k_{n_2}z)k_n\gamma_q\gamma_{q_1}\gamma_{q_2}J_1(\gamma_q r)\left[\gamma_{q_1}\lambda_{q_2n_2}J_1(\gamma_{q_2}r)J_0(\gamma_{q_1}r) - \gamma_{q_2}\lambda_{q_1n_1}J_1(\gamma_{q_1}r)J_0(\gamma_{q_2}r)\right] \\
&+\sin(k_n z)\cos(k_{n_1}z)\sin(k_{n_2}z)k_{n_1}\gamma_q\gamma_{q_1}\gamma_{q_2}J_1(\gamma_{q_1}r)\left[\gamma_{q_2}\lambda_{qn}^{\pm}J_1(\gamma_q r)J_0(\gamma_{q_2}r) - \gamma_q\lambda_{q_2n_2}J_0(\gamma_q r)J_1(\gamma_{q_2}r)\right] \\
&+\sin(k_n z)\sin(k_{n_1}z)\cos(k_{n_2}z)k_{n_2}\gamma_q\gamma_{q_1}\gamma_{q_2}J_1(\gamma_{q_2}r)\left[\gamma_q\lambda_{q_1n_1}J_0(\gamma_q r)J_1(\gamma_{q_1}r) - \gamma_{q_1}\lambda_{qn}^{\pm}J_1(\gamma_q r)J_0(\gamma_{q_1}r)\right]\} .
\end{aligned} \tag{3.28}$$

One can notice that this convolution term does not vary along with the time-advancing. Because the computation to obtain this term is very time-expensive, it should indeed be pre-calculated before the simulation. Its size can be largely constrained after some analyses of the n-n_1-n_2 dependence, but it still gives rise to a seven-dimensional array which occupies a large amount of RAM resources. Consider an illustration example with a truncation of $n_{\max} = 45$ and $q_{\max} = 52$. The size of the convolution array attains 24.9 Gb, although it has already been reduced to 1/30 of its original by the n-n_1-n_2 dependence. Due to this truncation limit, the Reynolds number of simulations cannot reach a very high level. But still, the Reynolds numbers allowed by this new CK basis $\mathbf{B}_{qn}$ is higher than those in [8, 7, 9].

3.1.4 Forcing method

Since the method is fully spectral, it is intuitive to apply a spectral forcing approach. The principle is similar to that in [8, 7, 9], namely a negative viscosity forcing [65]. The difference is that in [8], only one single parameter α is set to control the injection rate in both the poloidal (meaning the r-z plane) and the toroidal (meaning the θ direction) components, while in our simulations, we use two different parameters, named c_P and c_T (the subscript “P” stands for “poloidal” and “T” for “toroidal”). To avoid ambiguity, the negative viscosity ν^- is replaced by $-\nu$ in the following.

We define the poloidal and toroidal portions of the kinetic energy E_P and E_T as

$$\begin{aligned}
E_P &\equiv \frac{1}{V}\int_V \frac{1}{2}(u_r^2 + u_z^2)^2 \mathrm{d}V, \\
E_T &\equiv \frac{1}{V}\int_V \frac{1}{2}(u_\theta^2)^2 \mathrm{d}V.
\end{aligned} \tag{3.29}$$

By the same deduction procedure as in Appendix B for other statistical quantities, one can easily prove that their modal expressions write

$$\begin{aligned}
E_{P,qn} &= \frac{1}{4}(C_{qn}^{+\lambda} + C_{qn}^{-\lambda})^2, \\
E_{T,qn} &= \frac{1}{4}(C_{qn}^{+\lambda} - C_{qn}^{-\lambda})^2.
\end{aligned} \tag{3.30}$$

Then the modal equations respectively for E_P and E_T are :

$$\Longrightarrow \begin{cases}
\dfrac{\partial E_{P,qn}}{\partial t} = \mathrm{transfer}_{P,qn} - 2\nu\lambda_{qn}^2 E_{P,qn} + 2c_P\nu\lambda_{qn}^2 E_{P,qn}, \\
\dfrac{\partial E_{T,qn}}{\partial t} = \mathrm{transfer}_{T,qn} - 2\nu\lambda_{qn}^2 E_{T,qn} + 2c_T\nu\lambda_{qn}^2 E_{T,qn},
\end{cases} \tag{3.31}$$

with "transfer$_{P,qn}$" and "transfer$_{T,qn}$" modal energy transfer terms by nonlinear effets. From Eq.(3.31), it is clear that c_P governs exactly the poloidal forcing and c_T exactly the toroidal energy injection. By adjusting separately the values of (c_P, c_T), scenarii of different toroidal movement intensities can be achieved (this will be presented in Chapter 5 where the transition from non-swirling to swirling turbulence will be studied.).

A first remark from Eq.(3.31) is $\sum_{qn} \text{transfer}_{P,qn} = -\sum_{qn} \text{transfer}_{T,qn}$, because the integral of the total energy transfer is equal to zero. In [8, 7, 9], energy is shown to be transferred to the largest scales in axisymmetric turbulence. The Reynolds friction term corresponding to an all-scale dissipation (in fact, it aims particularly at removing ernergy at big scales) is however not included in Eq.(3.31). This choice is motivated by the fact that [8, 7] find that the insertion of this term is not necessary, probably due to the presence of the cylindrical wall. The geometry in the current thesis is well confined in all directions, and the solid walls are therefore expected to prevent even more the flow structures from growing unlimitedly.

3.1.5 Time step

The time scheme used in this FSM is the 4th-order Runge-Kutta scheme. For the determination of time step, we use an adaptive time step method. The time step Δt is determined by evaluating the Courant number at every time :

$$C(t_m) = \frac{U(t_m)\Delta t(t_m)}{\Delta x} \qquad \Longleftrightarrow \qquad \Delta t(t_m) = \frac{C(t_m)\mathrm{d}x}{U(t_m)}, \tag{3.32}$$

where U is a characteristic velocity that reflects the velocity of largest magnitude at time t_m, and $\mathrm{d}x$ is a characteristic meshing length referring to the smallest discretized length gap within the domain. Because the numerical method is fully spectral, we choose U related to the root mean square of the total kinetic energy

$$U(t_m) = \sqrt{\frac{2E(t_m)}{3}} \quad \text{with} \quad E(t_m) = \frac{1}{2}\sum_{qn}^{\pm\lambda} C_{qn}^2(t_m), \tag{3.33}$$

and define Δx as the reciprocal of the maximal effective wave-number

$$\Delta x = \frac{1}{\sqrt{k_{\max}^2 + \gamma_{\max}^2}} = \frac{1}{\sqrt{(n_{\max}\pi/H)^2 + \gamma_{\max}^2}}. \tag{3.34}$$

The criterion of C is fixed empirically at 0.05 and is validated to be optimal by Qu [8] through a series of tests. All of our computations converge well with this value. This gives rise to a variable time step mechanism during the simulation. However, Δt may be large after a long period of energy dissipation. To ensure that the time discretization is fine enough, another condition is superposed : if Δt is evaluated to be greater than 0.001, then it is forced to be 0.001, *i.e.* the upper bound of Δt is 0.001.

As mentioned in Section 3.1.3, the integral (3.28) needs to be pre-calculated. A numerical approximation rule of definite integration is needed. To obtain the result with high precision, we choose to adopt the Gaussian quadrature method.

3.1.6 Simulation resolution

A classic way to check that the resolution is sufficient for a given Reynolds number is to implement a series of simulations of the same flow with increasing resolutions. When simulations of resolutions higher than a certain level yield identical behavior, this level is said sufficient for the flow. Rigorous as it is, this method is expensive in both aspects of time and computational resources. In the context of our numerical method, the resolution is assessed by comparisons between the smallest simulated scale and the dissipative scales of the turbulent flow, inspired by the standard practice in pseudo-spectral DNS of isotropic turbulence [58]. Since dissipative scales are the smallest scales of a flow, the resolution can be considered of good quality if the smallest simulated scales are smaller than the dissipative scales.

We introduce first the concept of the effective wave-number k, defined as $|\lambda_{qn}|$:

$$k(q,n) = |\lambda_{qn}| = \sqrt{k_n^2 + \gamma_q^2}. \tag{3.35}$$

Thus the smallest simulated scale is determined by the largest effective wave-number :

$$k(q_{\max}, n_{\max}) = \sqrt{k_{\max}^2 + \gamma_{\max}^2}. \tag{3.36}$$

As per Kolmogorov's theory, the energy dissipative scale depends only on the viscosity ν and the energy dissipation rate ε_E, and is derived by dimensional analysis to be

$$k_E = C_E \varepsilon_E^{1/4} \nu^{-3/4}, \tag{3.37}$$

with $C_E \sim O(1)$ a constant. Besides, we consider also the dissipative scales of enstrophy Z, angular momentum I_1 and helicity H_1 by similarly assuming that they depend only on ν and respective dissipation rates ε_Z, ε_{I_1} and ε_{H_1}. Then by dimensional analyses, these scales are derived to be

$$\begin{aligned} k_Z &= C_Z \varepsilon_Z^{1/6} \nu^{-1/2}, \\ k_{I_1} &= C_{I_1} \varepsilon_{I_1}^{1/2} \nu^{-1}, \\ k_{H_1} &= C_{H_1} \varepsilon_{H_1}^{1/5} \nu^{-3/5}, \end{aligned} \tag{3.38}$$

where C_Z, C_{I_1} and C_{H_1} are constants of magnitude $O(1)$. By investigating the spectral governing equations of E, Z, I_1 and H_1, the spectral formulae of their dissipation rates can be derived as well :

$$\begin{aligned} \varepsilon_E &= \nu \sum_{qn}^{\pm\lambda} \lambda_{qn}^2 C_{qn}^2, \\ \varepsilon_Z &= 2\nu \sum_{qn}^{\pm\lambda} \lambda_{qn}^4 C_{qn}^2, \\ \varepsilon_{I_1} &= \frac{4\nu}{\pi} \sum_{q,\text{odd } n} \frac{\lambda_{qn}^2 (C_{qn}^{-\lambda} - C_{qn}^{+\lambda}) \operatorname{sign}(J_0(\gamma_q R))}{n\gamma_q}, \\ \varepsilon_{H_1} &= \nu \sum_{qn}^{\pm\lambda} \lambda_{qn}^3 C_{qn}^2. \end{aligned} \tag{3.39}$$

The scales defined in (3.37) and (3.38) are compared to the smallest numerical scales in our simulations. This testing method has been applied to all simulations using the FSM.

3.1.7 Verification tests

Some first tests are performed here to validate the FSM before using it. We choose to verify the conservation, during an early period, of the kinetic energy E and of some of the Casimirs I_n and H_m. For an inviscid flow constrained by the same boundary conditions as ours, their conservation is mathematically demonstrated in [6]. Respectively, we investgate numerically the behavior of E, I_0, I_1, H_1 and H_2 with zero viscosity. This can be easily accomplished since their modal expressions are derived in Appendix B. Then tests of different resolutions, from the lowest to the highest available, are implemented with $\nu = 0$, $R = \pi$ and $H = 1.7\pi$. Time signals (see Fig.3.3) are plotted using the dimensionless time scale τ, the initial turnover time, defined as

$$\tau = \frac{l_{\text{init}}}{U_{\text{init}}}, \tag{3.40}$$

where l_{init} is the initial integral length scale and U_{init} is related to the root mean square of the initial kinetic energy :

$$l_{\text{init}} = \frac{\sum\limits_{qn}^{\pm\lambda} \left(\sqrt{k_n^2 + \gamma_q^2}\right)^{-1} E_{qn}(t=0)}{\sum\limits_{qn}^{\pm\lambda} E(t=0,q,n)}, \tag{3.41a}$$

$$U_{\text{init}} = \sqrt{\frac{2E(t=0)}{3}}. \tag{3.41b}$$

From Fig.3.3, one can conclude that the kinetic energy E and the helicity H_1 are well conserved for all resolutions (in fact, it can be proved that they are mathematically conserved under the current basis $\mathbf{B}_{qn}$ even with truncation), and that the rest of the quantities diverge due to the truncation effect. But tendencies allow to tell that the higher the resolution, the later and the less the conservations are violated.

3.2 The pseudo-spectral method (PSM)

For axisymmetric cases with higher Reynolds numbers, the fully spectral method described in the previous section is no longer usable due to the huge resource occupation caused by Eq.(3.28). Therefore, we turn to a pseudo-spectral method (PSM) based on the Chebyshev (Gauss-Lobatto) collocation expansion method. For this, we use a code devised by Raspo *et al.* [66] and developed by Peres *et al.* [67] and integrating the full Navier-Stokes equations (with ∂_r, ∂_z and $\partial_\theta \neq 0$) in a closed cylindrical domain. We use this code for two different aims : (i) to investigate strictly axisymmetric turbulence at higher Reynolds numbers than those permitted by the FSM and with boundary conditions closer to those of realistic setups including in particular the von Kármán experiment ; and (ii) to investigate the transition from axisymmetric ($\partial_\theta = 0$) to 3D turbulence. For this, we adapte the code in two different ways.

The initial version of the code, developed by Raspo *et al.* [66], is first briefly described in Section 3.2.1. We then present in Section 3.2.2 the modifications that we have done so as to investigate the flows of interest. The results of some validation tests are finally presented in Section 3.2.4.

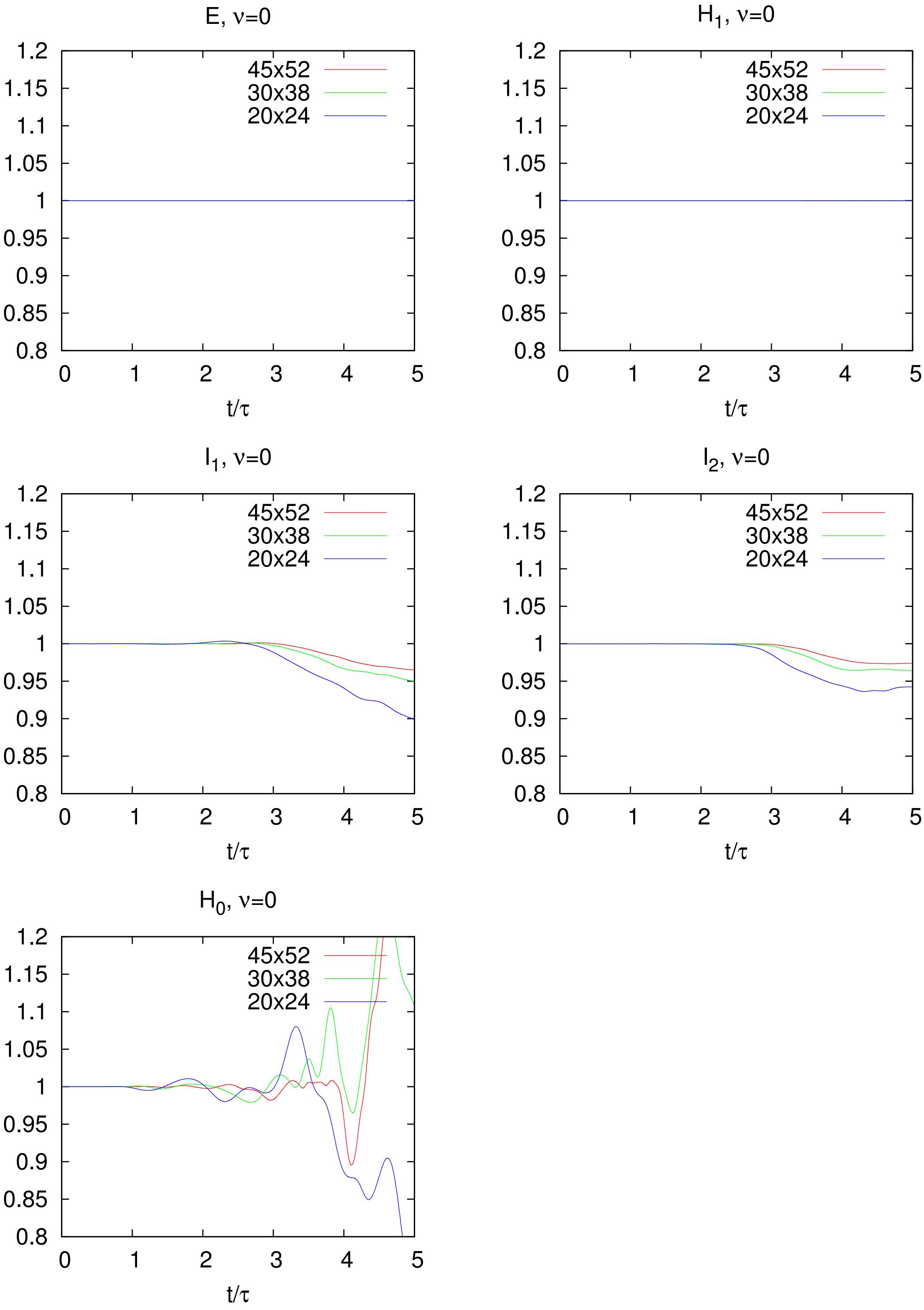

FIGURE 3.3: Temporal signals of statistical invariants for inviscid simulations under different resolutions. The curves are normalized by initial values of corresponding quantities.

3.2.1 Brief description of the initial version of the code

The specialty of pseudo-spectral methods lies in the fact that derivatives are calculated in spectral space to ensure the numerical precision, while multiplication of terms will be conducted in physical space to reduce time expenses. The code developed by Raspo *et al.* [66] uses Chebyshev polynomials to decompose the radial and axial components of flow fields, while azimuthal components are descretized by Fourier modes.

We will show that the Chebyshev (Gauss-Lobatto) collocation method allows to impose real wall boundary conditions to the flow domain. In fact, as the poloidal plane is treated in the physical space, it is more intuitive and convenient to add desired conditions to the domain boundaries.

Apart from the decomposition bases, the PSM that we use here has several differences compared with the FSM presented in the last section :

1. The current PSM decomposes the three velocity components separately, while the FSM has recourse to a vectorial basis that decomposes the three components once for all. Thus, unlike Eq.(3.27), there will be three control equations concerning the three components separately.

2. Most of the calculations will be manipulated in the physical space in the form of matrix products. One of the advantages of this Chebyshev collocation method is that the 1st- and the 2nd-order derivatives of the expanded variable can be analytically expressed in the physical space in a matrix form. Therefore, the flow evolution within the poloidal plane will be directly simulated in the physical space. This is the most important element which will make high Reynolds numbers accessible.

3. For each velocity component as well as for pressure, both Dirichlet and Neumann boundary conditions can be imposed to the walls of the cylinder. When Dirichlet boundary condition are imposed (the boundary value can only be 0), one imposes the no-penetration condition ; when Neumann boundary condition is switched on (the value of the boundary derivative against the wall's normal direction can also only be 0), one imposes the no-slip condition.

The time discretization method of the PSM is proposed by Raspo *et al.* [66], featured by its modified projection method, is directly applicable in our cases.

Forcing method

To mimic the mechanical forcing by counter-rotating impellers, angular velocities Ω of opposite signs are added to the upper and the lower bounds of our computational domain, and they play the role of "rotors". The lateral wall is fixed. The curved blades are not taken into consideration for the sake of simplicity (see Fig.3.4). However, the junction areas between the rotors and the lateral walls present some singularity. Take the upper bound of the cylinder as example. The rotation velocity attains its maximum ΩR at the outer radius of the rotors, but the nodes on the lateral boundary and vertically right under the rotor layer should be motionless, meaning that there is a drop of $|u_\theta|$ from ΩR to 0 at this junction area. The lower bound should deal with the same problem. To regularize this singularity, a boundary layer function of $V_\theta(\bar{z}) = \mathrm{e}^{-(\bar{z}-1)/\mu}$ is applied on the lateral wall which softens the discontinuous drop into an exponential decrease. Here μ is an arbitrary shape parameter that equals 0.006 and is independent of the grid size. Otherwise, it is shown by Serre and Bontoux [68] that the value 0.006 represents reasonably the gap size of the junction in experimental devices.

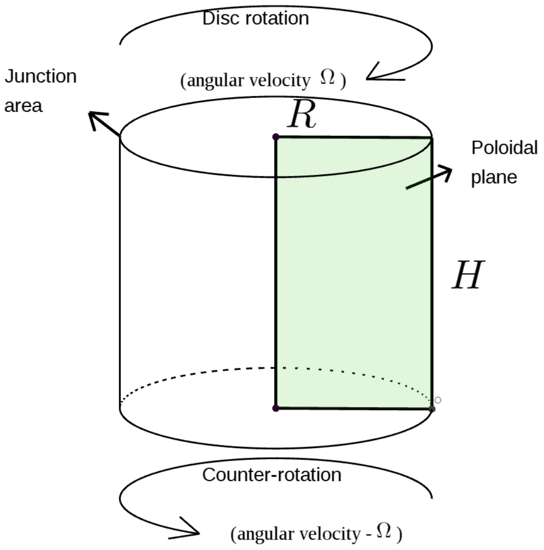

FIGURE 3.4: Sketch of the PSM numerical set-up. The impellers are simplified into symmetrically counter-rotating discs.

3.2.2 Adaptation of the code to investigate the transition from axisymmetric to 3D turbulence ($\partial\theta \mapsto \alpha\partial_{\overline{\theta}}$; $\alpha \in [0,1]$)

As already mentioned, the original version of the code integrates the Navier-Stokes equation without restriction on the spatial derivatives. Our purpose is to investigate axisymmetric flows ($\partial_\theta = 0$), but also flows slowly varying in the azimuthal direction ($\partial_\theta \mapsto \alpha\partial_{\overline{\theta}}$ with $0 \leqslant \alpha \leqslant 1$).

Axisymmetric flows are mathematically described by the peculiarity $\partial_\theta = 0$. However, they can also be described from another angle : for axisymmetric flows, the variation period in the azimuthal direction is $+\infty$. Similarly, general 3D flows retained in a cylinder can be considered as flows of which the azimuthal variation period is 2π. Then here comes an interesting question : what are flows with an azimuthal variation period between $+\infty$ and 2π ?

If such intermediary flows can be simulated, then there should be some variation tendencies that characterize their physics. One subject to look into is the characteristic length scale of toroidal structures (denoted as L_T). For axisymmetric flows, since the azimuthal variation period is infinity, the toroidal characteristic length scale should also be infinitely long : $L_T = +\infty$. For a general 3D flow, the toroidal characteristic length scale should be of the same order as that in the poloidal plane (denoted as L_P), and conventionally we define them to be identical and equal to the cylinder radius R : $L_T = L_P = R$. However, for cases where the azimuthal variation period is between $+\infty$ and 2π, one has $L_T \in [R, +\infty)$. Then toroidal lengths can in fact be normalized by L_T instead of L_P, while original normalization of poloidal lengths is kept. We can define dimensionless coordinates $\bar{r}$, $\bar{z}$ and $\bar{\theta}$ such that :

$$\begin{aligned} r &= R\bar{r}, \\ z &= \frac{H}{2}\bar{z} = \frac{R}{G}\bar{z}, \\ r\theta &= L_T\overline{r\theta} = L_T\bar{r}\bar{\theta} = \frac{L_T}{R}R\bar{r}\bar{\theta}, \end{aligned} \tag{3.42}$$

with $G \equiv 2R/H$ the aspect ratio of the poloidal plane. We introduce the notation $\alpha = R/L_T$ and the toroidal normalization becomes $r\theta = R\bar{r}\bar{\theta}/\alpha$. By applying this toroidal characteristic length scale and the α parameter, the Navier-Stokes equations can be rewritten as

$$
\begin{aligned}
&\frac{1}{G}\frac{\partial \bar{u}_r}{\partial \bar{r}} + \frac{1}{G}\frac{\bar{u}_r}{\bar{r}} + \frac{1}{G}\frac{1}{\bar{r}}\alpha\frac{\partial \bar{u}_\theta}{\partial \bar{\theta}} + \frac{\partial \bar{u}_z}{\partial \bar{z}} = 0,\\
&\frac{\mathrm{Re}_\Omega}{G^2}\frac{\partial \bar{u}_r}{\partial \bar{t}} + \frac{\mathrm{Re}_\Omega}{G}\left(\frac{1}{G}\bar{u}_r\frac{\partial \bar{u}_r}{\partial \bar{r}} + \frac{1}{G}\frac{\bar{u}_\theta}{\bar{r}}\alpha\frac{\partial \bar{u}_r}{\partial \bar{\theta}} + \bar{u}_z\frac{\partial \bar{u}_r}{\partial \bar{z}} - \frac{1}{G}\frac{\bar{u}_\theta^2}{\bar{r}}\right)\\
=&-\frac{\mathrm{Re}_\Omega}{2G^2}\frac{\partial \bar{p}}{\partial \bar{r}} + \left(\frac{1}{G^2}\frac{\partial^2 \bar{u}_r}{\partial \bar{r}^2} + \frac{1}{G^2}\frac{1}{\bar{r}}\frac{\partial \bar{u}_r}{\partial \bar{r}} + \frac{1}{G^2}\frac{1}{\bar{r}^2}\alpha^2\frac{\partial^2 \bar{u}_r}{\partial \bar{\theta}^2} + \frac{\partial^2 \bar{u}_r}{\partial \bar{z}^2} - \frac{1}{G^2}\frac{\bar{u}_r}{\bar{r}^2} - \frac{1}{G^2}\frac{2}{\bar{r}^2}\alpha\frac{\partial \bar{u}_\theta}{\partial \bar{\theta}}\right),\\
&\frac{\mathrm{Re}_\Omega}{G^2}\frac{\partial \bar{u}_\theta}{\partial \bar{t}} + \frac{\mathrm{Re}_\Omega}{G}\left(\frac{1}{G}\bar{u}_r\frac{\partial \bar{u}_\theta}{\partial \bar{r}} + \frac{1}{G}\frac{\bar{u}_\theta}{\bar{r}}\alpha\frac{\partial \bar{u}_\theta}{\partial \bar{\theta}} + \bar{u}_z\frac{\partial \bar{u}_\theta}{\partial \bar{z}} + \frac{1}{G}\frac{\bar{u}_r\bar{u}_\theta}{\bar{r}}\right)\\
=&-\frac{\mathrm{Re}_\Omega}{2G^2}\frac{1}{\bar{r}}\alpha\frac{\partial \bar{p}}{\partial \bar{\theta}} + \left(\frac{1}{G^2}\frac{\partial^2 \bar{u}_\theta}{\partial \bar{r}^2} + \frac{1}{G^2}\frac{1}{\bar{r}}\frac{\partial \bar{u}_\theta}{\partial \bar{r}} + \frac{1}{G^2}\frac{1}{\bar{r}^2}\alpha^2\frac{\partial^2 \bar{u}_\theta}{\partial \bar{\theta}^2} + \frac{\partial^2 \bar{u}_\theta}{\partial \bar{z}^2} - \frac{1}{G^2}\frac{\bar{u}_\theta}{\bar{r}^2} + \frac{1}{G^2}\frac{2}{\bar{r}^2}\alpha\frac{\partial \bar{u}_r}{\partial \bar{\theta}}\right),\\
&\frac{\mathrm{Re}_\Omega}{G^2}\frac{\partial \bar{u}_z}{\partial \bar{t}} + \frac{\mathrm{Re}_\Omega}{G}\left(\frac{1}{G}\bar{u}_r\frac{\partial \bar{u}_z}{\partial \bar{r}} + \frac{1}{G}\frac{\bar{u}_\theta}{\bar{r}}\alpha\frac{\partial \bar{u}_z}{\partial \bar{\theta}} + \bar{u}_z\frac{\partial \bar{u}_z}{\partial \bar{z}}\right)\\
=&-\frac{\mathrm{Re}_\Omega}{2G}\frac{\partial \bar{p}}{\partial \bar{z}} + \left(\frac{1}{G^2}\frac{\partial^2 \bar{u}_z}{\partial \bar{r}^2} + \frac{1}{G^2}\frac{1}{\bar{r}}\frac{\partial \bar{u}_z}{\partial \bar{r}} + \frac{1}{G^2}\frac{1}{\bar{r}^2}\alpha^2\frac{\partial^2 \bar{u}_z}{\partial \bar{\theta}^2} + \frac{\partial^2 \bar{u}_z}{\partial \bar{z}^2}\right).
\end{aligned}
\tag{3.43}
$$

where $\bar{t}$ is the dimensionless time, $\bar{u}_r$, $\bar{u}_\theta$ and $\bar{u}_z$ are dimensionless velocity components, $\mathrm{Re}_\Omega \equiv R^2\Omega/\nu$ is the large-scale Reynolds number based on Ω, and $\bar{p} \equiv p/(\rho R^2\Omega^2/2)$ is the dynamic pressure coefficient based on Ω. All of the derived variables are then discretized within $(\bar{r}, \bar{z}) \in [-1, 1] \times [-1, 1]$ by Chebyshev polynomials. There are two arguments to clarify before fitting these equations into numerical simulations :

1. Since $L_T \in [R, +\infty)$, one has $\alpha \in [0, 1]$. For the case where $\alpha = 0$, the toroidal characteristic length scale is infinity. This also leads to the disappearance of azimuthal derivation terms, and Eq.(3.43) returns to its axisymmetric version. For $\alpha = 1$, toroidal characteristic length scale is R, and Eq.(3.43) keeps the general 3D version. Then, the cases of $\alpha \in [0, 1]$ represent the flows of which the regime is between axisymmetric and general three-dimensional.
2. One can observe that in Eq.(3.43), ∂_θ is replaced by $\partial_{\bar{\theta}}$ where $\bar{\theta}$ signifies the rescaled azimuthal coordinate. This means that there is a mapping of the definition domain of θ to a rescaled definition domain of $\bar{\theta}$. For the sake of numerical feasibility, this rescaled azimuthal definition domain should be $\bar{\theta} \in [0, 2\pi]$.

In general, the result of the upper two arguments is that when adapting the algorithm, one inserts the α-like factors before the azimuthal derivation terms :

$$\frac{\partial}{\partial \theta} \mapsto \alpha\frac{\partial}{\partial \bar{\theta}} \quad \text{and} \quad \frac{\partial^2}{\partial \theta^2} \mapsto \alpha^2\frac{\partial^2}{\partial \bar{\theta}^2}, \tag{3.44}$$

with $\bar{\theta}$ varies also from 0 to 2π. This means that we consider velocity fields slowly varying in the azimuthal direction.

3.2.3 Spatial and temporal resolution

We will check the spatial and temporal resolution for the PSM by using the same method as for the FSM : the mesh size will be compared with the dissipation scales of different statistical quantities, while the time step fineness will be judged by calculating the Courant number. However, differences arise from the fact that we now use a non-homogeneous mesh :

1. **Spatial resolution.** Dissipation rates of various quantities are calculated through the decomposition and integration methods mentioned in Appendices C and D, and will be used to derive the dissipative wave-numbers like those in Section 3.1.6. The effective wave-number of the largest mesh size will be chosen to compare with them. Because of the property of Gauss-Lobatto collocation points, the largest mesh size lies at the center of the domain. We denote its radial and axial dimensions as $\Delta R_{\max}$ and $\Delta H_{\max}$, and define the corresponding maximal effective wave-number as

$$k_{\max} = \sqrt{\left(\frac{2\pi}{\Delta R_{\max}}\right)^2 + \left(\frac{2\pi}{\Delta H_{\max}}\right)^2}. \tag{3.45}$$

   This effective wave-number will then be compared with the dissipation wave-numbers of E, Z, I_1 and H_1.

2. **Temporal resolution.** Like in the FSM, we use the Courant number as a criterion to determine the required time step. The time step appears in the calculation of solver matrices. These matrices need to be recalculated if $\Delta \bar{t}$ changes its value. We then adopt a fixed time step mechanism to simplify the procedure and to avoid extra time expense, given the fact that the calculation of these matrices takes several minutes. Due to the non homogeneity of the grid, we calculate the Courant number for each velocity component on each grid node.
   For axisymmetric flows, the Courant numbers are calculated as :

$$C_r(r,z,t) = \left|\frac{u_r(r,z,t)\Delta t}{\Delta R(r,z)}\right|, \tag{3.46a}$$

$$C_z(r,z,t) = \left|\frac{u_z(r,z,t)\Delta t}{\Delta H(r,z)}\right|, \tag{3.46b}$$

   with $\Delta R(r,z)$ and $\Delta H(r,z)$ the local grid sizes in the radial and axial directions respectively. The maximal value among them, $\max(C_r(r,z,t), C_z(r,z,t))$, will be picked out as the characterizing Courant number of the current time step.
   For non-axisymmetric flows, the Courant numbers are calculated as :

$$\begin{aligned}
C_r(r,\bar{\theta},z,t) &= \left|\frac{u_r(r,\bar{\theta},z,t)\Delta t}{\Delta R(r,\bar{\theta},z)}\right|, \\
C_\theta(r,\bar{\theta},z,t) &= \left|\frac{u_\theta(r,\bar{\theta},z,t)\Delta t}{r\Delta\bar{\theta}}\right|, \\
C_z(r,\bar{\theta},z,t) &= \left|\frac{u_z(r,\bar{\theta},z,t)\Delta t}{\Delta Z(r,\bar{\theta},z)}\right|, \\
C_{\max}(r,\bar{\theta},z,t) &= \max(C_r(r,\bar{\theta},z,t), C_\theta(r,\bar{\theta},z,t), C_z(r,\bar{\theta},z,t)).
\end{aligned} \tag{3.47}$$

3.2.4 Verification test of axisymmetric freely decaying flows

In this subsection, a verification test of the PSM code will be conducted. For this, we simply run simulations by using respectively the PSM and the FSM, and compare the results of both. For the FSM, the code is written for strictly axisymmetric flows; for the PSM, axisymmetric flows can be simulated by setting $\alpha = 0$. The two cases are for the same geometry ($R = \pi$ and $H = 1.7\pi$), initial condition (see Fig.3.5), viscosity ($\nu = 0.005$), and boundary conditions :

$$\begin{aligned} \bar{u}_r &= 0 \quad \text{on lateral walls,} \\ \frac{\partial \bar{u}_r}{\partial \bar{r}} &= 0 \quad \text{on top and bottom,} \\ \bar{u}_\theta &= 0 \quad \text{on } \partial\mathrm{D}, \\ \frac{\partial \bar{u}_z}{\partial \bar{z}} &= 0 \quad \text{on lateral walls,} \\ \bar{u}_z &= 0 \quad \text{on top and bottom,} \end{aligned} \tag{3.48}$$

and are freely decaying from the initial condition. As mentioned in Section 3.2.1, the PSM code indeed allows to simulate flows with partial slip boundary conditions, which is reflected in Fig.3.5b by the fact that u_r is not zero on top and bottom of the cylinder.

Fig.3.6 is the contour plots of ψ at a certain time during the evolution and shows qualitatively the coincidence of the two simulations. Further, the coincidence is quantitatively validated by the kinetic energy curves in Fig.3.7 which are perfectly superimposed. Besides, resolution tests and Courant number evolution are also shown (see Figs.3.8 and 3.9), showing the reliability of the two simulations. For details, the resolution for the FSM test case is $(q_{\max}, n_{\max}) = (52, 45)$, giving rise to a maximal effective wave-number of 59, and for the PSM test case it is $(N, M) = (246, 257)$, giving rise to a maximal effective wave-number of 247 ; the time step of the FSM test case varies along the simulation, as mentioned in Section 3.1.5, and Δt for the PSM test case is fixed as 5×10^{-4} s.

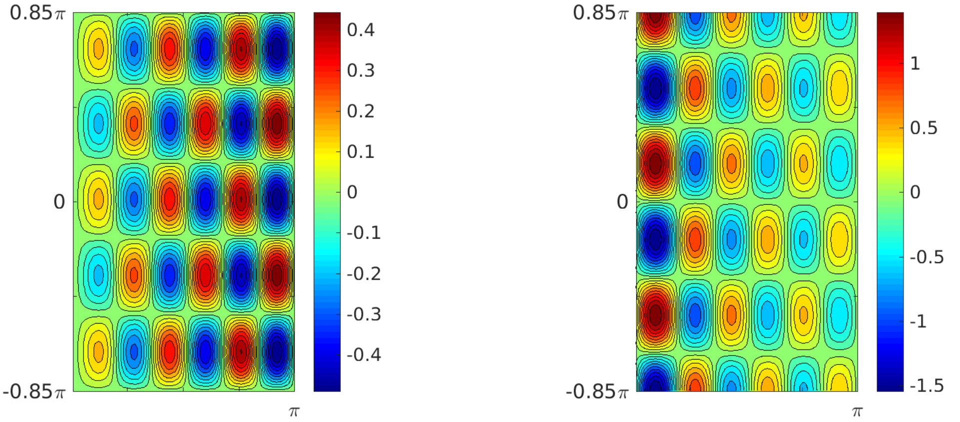

(a) Initial stream function ψ (b) Initial radial velocity component u_r

FIGURE 3.5: Visualization of initial conditions for the comparison cases.

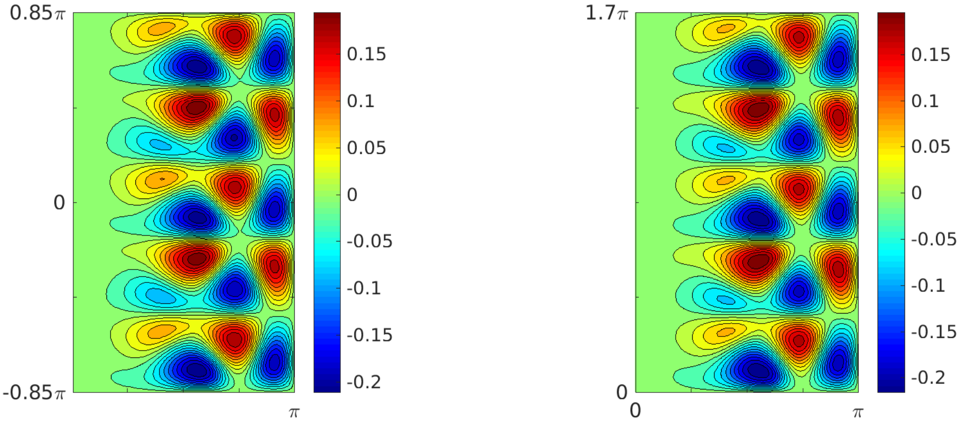

(a) ψ of PSM (b) ψ of FSM

FIGURE 3.6: Contour plots of ψ for the PSM and the FSM at $t = 5$ s. Some slight differences can be remarked and may be due to numerical errors.

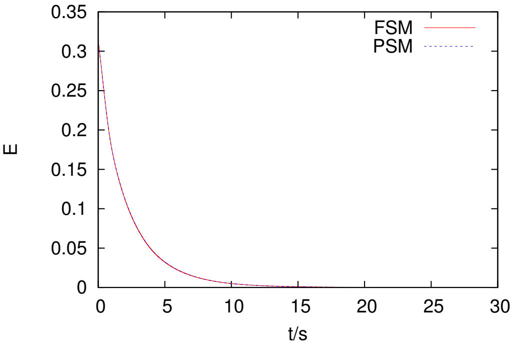

FIGURE 3.7: Comparison of kinetic energy simulated by the two codes. It validates the PSM code, and at the same time proves that the integration and decomposition methods are globally correct and accurate.

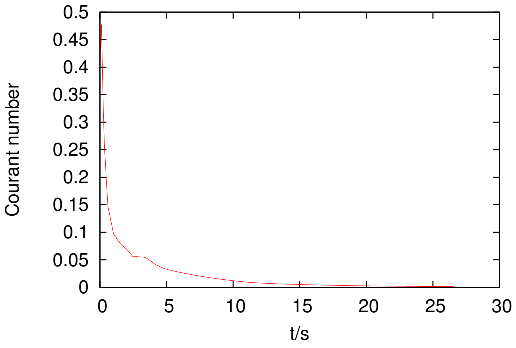

FIGURE 3.8: Courant number time signal of the PSM simulation.

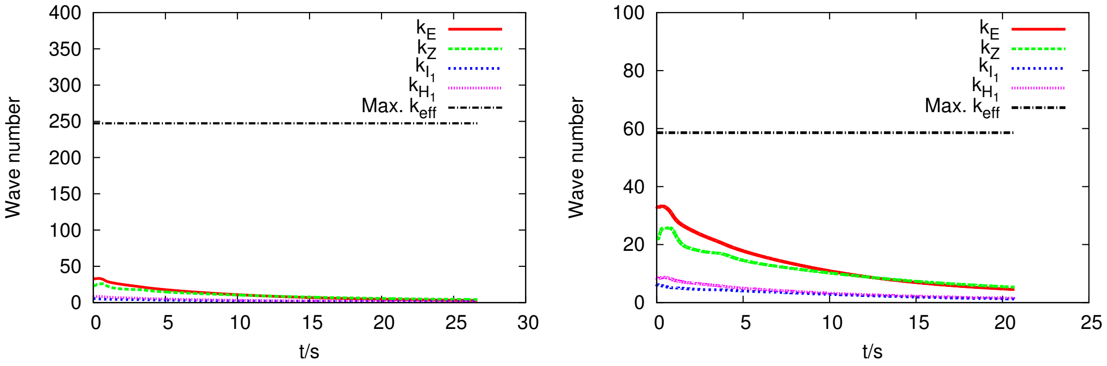

(a) PSM (b) FSM

FIGURE 3.9: Wave-number comparison.

CHAPITRE 4

Coherent Structures in Statistically Stationary Axisymmetric Turbulence

---

The general behavior of axisymmetric turbulence was recently studied in [7, 8, 9] in cylindrical geometry, periodic in its axial direction, at fairly low Reynolds number. Coherent structures predicted by statistical mechanics of the Euler equations were nevertheless observed in freely decaying flows. In the current thesis, both our FSM and PSM codes for axisymmetric flows allow not only the confinement of the cylinder, but also the possibility for higher Re. It is therefore interesting to try to numerically assess in forced flows the possible existence of coherent structures. Particularly, the PSM allows to investigate a configuration which is close to the von Kármán flow [21], where coherent structures are experimentally seen. In this chapter, therefore, we will present the results obtained by FSM and PSM in statistically steady states, and compare our observations with those in [7, 8, 9] and [21].

4.1 Spectrally forced axisymmetric flow

In this section, results obtained for statistically steady flow using the FSM will be presented and compared to those obtained in [7, 8, 9]. We recall that the computational configuration in [7, 8, 9] is different from ours. Therein, a periodic boundary condition is imposed in the z direction, which leads to an axial decomposition using complex Fourier series. At difference, the computation domain in our thesis is confined in the z direction, and trigonometric functions in the real number space are employed to decompose the axial direction. The numerical method poses a constraint on the Reynolds number in our simulations, as in [7, 8, 9]. Indeed, the fact of employing trigonometric functions in the real number space instead of complex Fourier series allows a certain reduction of the size of array (3.28), and thus a possible access to higher Reynolds numbers. Many interesting results, either with or without energy injection, are given and analyzed in [7, 8, 9], concerning the presence of coherent structures, functional relationships between different variables, energy spectra, cascade directions, velocity probability distribution functions (called “PDF” hereafter), *etc.* We will evaluate these quantities and make comparisons between our results and those in [7, 8, 9].

We consider the aspect ratio as in [8] with $R = \pi$ and $H = 1.7\pi$. We present the results of a simulation, with a kinematic viscosity of $\nu = 0.0025$ and a selected band of wave-number $k \in [11, 15]$ for the spectral forcing presented in Section 3.1.4. The stationary Reynolds number $\mathrm{Re} \equiv \sqrt{2E/3}H/\nu$ is about 1230. To achieve this, the resolution is $(q_{\max}, n_{\max}) = (52, 45)$, generating a maximal effective wave-number $k_{\max} \approx 59$.

4.1.1 Temporal results

Time signals of the statistical quantities and the resolution tests are shown in Fig.4.1. Time is normalized by a characteristic time defined as

$$\tau = \frac{R}{\sqrt{2E/3}}. \tag{4.1}$$

The curves of E, H_0 and I_1 show an almost quiescent stationary state while those of H_1 and I_2 fluctuate are more intermittent. However, all of these quantities are rather well conserved during $2\tau \leq t \leq 15\tau$. The resolution test compares the characteristic physical cut-off wave-numbers defined in Section 3.1.6 with the numerical maximum wave-number. The curves of the resolution tests show that except at the beginning of the simulation, during the transient state, there is a sufficient overall resolution.

Because statistical mechanics theories predict the existence of coherent structures, it will be interesting to inspect their emergence. Contour plots of the stream function ψ at different times are shown in Fig.4.2 and those of σ in Fig.4.3. For σ plots, no notable structures can be observed. For ψ, in contrast, coherent structures are better distinguishable. One can see that at certain moments, big structures appear and persist, while at some others moments, they break into smaller ones which then tend to reunite again to extend their sizes. We reiterate the conclusion drawn in [22] that the critical points of the variational problem (2.57) are linearly unstable solutions of the Euler equations. It is also experimentally confirmed by [21] that coherent structures cannot resist the impact of some "optimal" perturbations. It is clearly possible that the modal injection method induces some movements playing the role of optimal perturbations that force the coherent structures to wobble and to crush. The dynamics of ψ being stable only during certain time periods, we investigate the averaged behaviors of the system during these periods.

4.1.2 Time-averaged results

There are indeed stable time intervals of different lengths during which the ψ structures keep their sizes and do not move a lot. Fig.4.4 shows the time-averaged ψ and σ isocontours and functional relationships. Time average has been performed on the interval $4\tau \leqslant t \leqslant 6\tau$. Large and smooth structures of $\overline{\psi}$ are seen. A clear fitting of the function $\overline{\sigma} = F(\overline{\psi}) = 0.1\overline{\psi} + 0.08\overline{\psi}^3$ is extracted by the least square method. By focusing on the coherent bulk where the effect of dissipation is less important than on the boundaries, and with the expression of $F(\overline{\psi})$, the fitting of the function $G(\overline{\psi}) = \overline{\xi} - \overline{\sigma}'\overline{\sigma}/r^2$ can also be done, yielding $G(\overline{\psi}) = 0.9\overline{\psi}$. This means that the bulk flow resembles a solution of the axisymmetric Euler equations (2.49).

4.1.3 Energy spectrum

Energy and helicity cascades

The energy and helicity cascades in three-dimensional turbulence have long been the focus of many studies. First described by Richardson [69] in 1922, a three-dimensional turbulent flow transfers **energy** from bigger to smaller and smaller scales until the viscous dissipation comes into play. Basing on this description as well as a set of additional

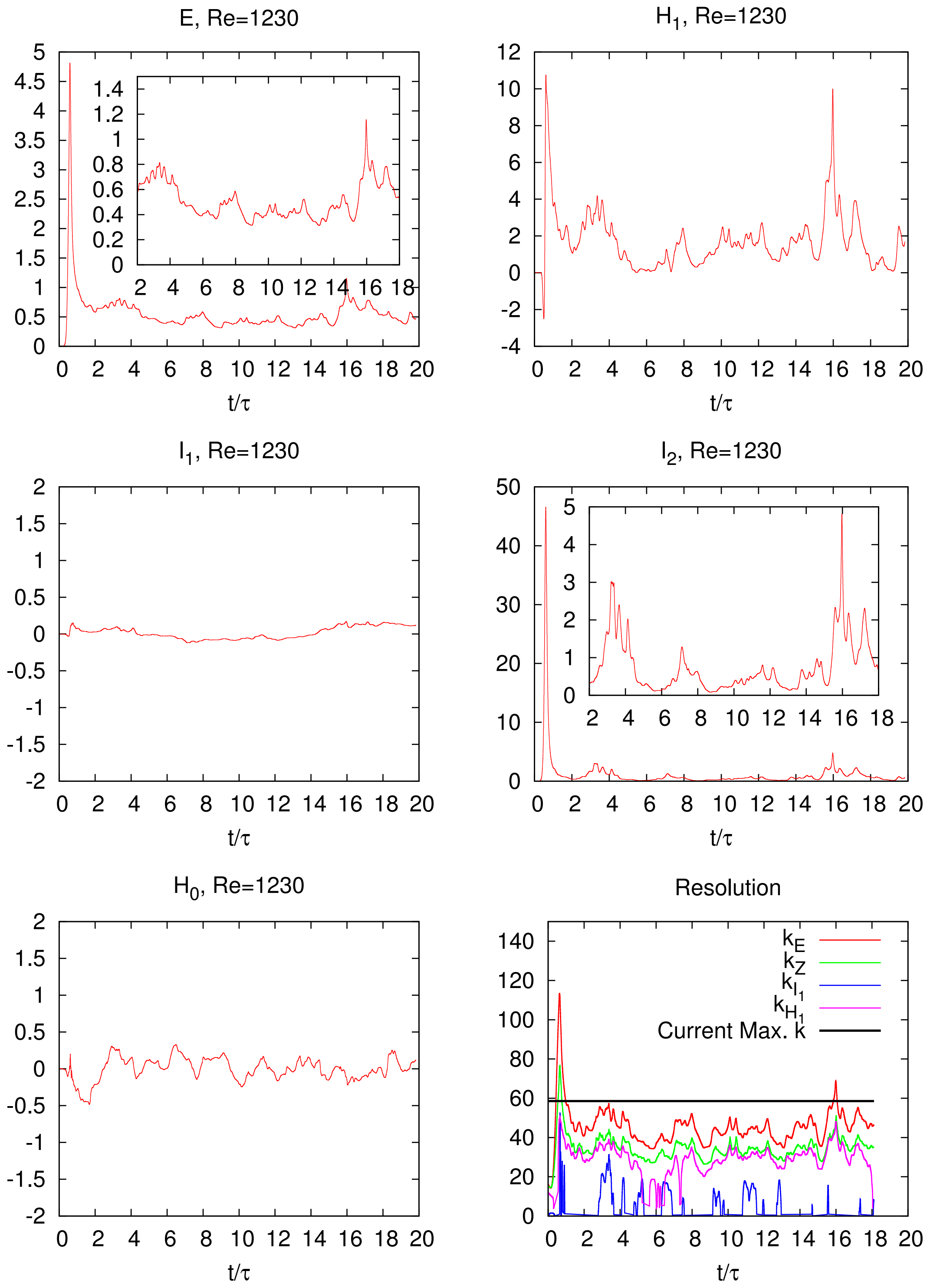

FIGURE 4.1: Temporal signals of statistical invariants and resolution tests for a forced simulation. In this simulation, velocity fields of $2\tau \leqslant t \leqslant 15\tau$ are considered stationary and are thus used.

hypotheses, Kolmogorov [70] proposed in 1941, for stationary turbulent flows with sufficiently high Reynolds numbers, a formula of the energy spectrum within the inertial range :

$$E(k) = C_E \varepsilon^{2/3} k^{-5/3}, \tag{4.2}$$

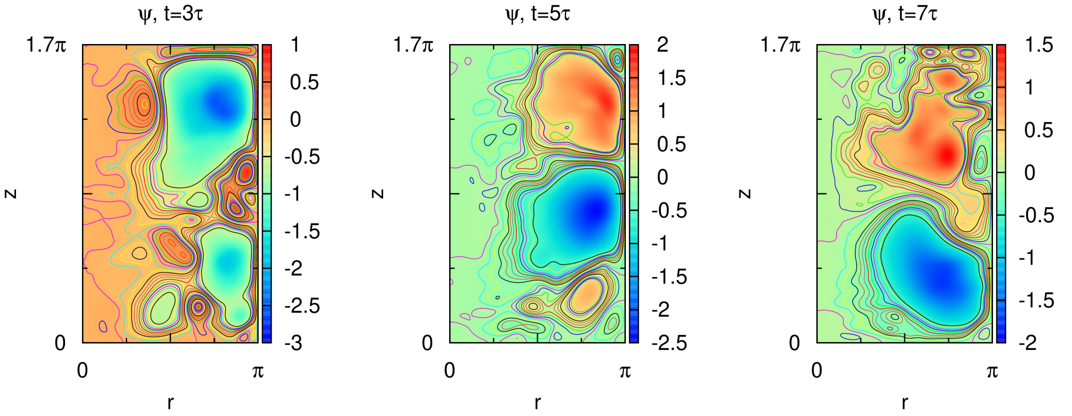

(a) Dominance of negative structures.

(b) Presence of a dipole system.

(c) Dissolution of the positive structure.

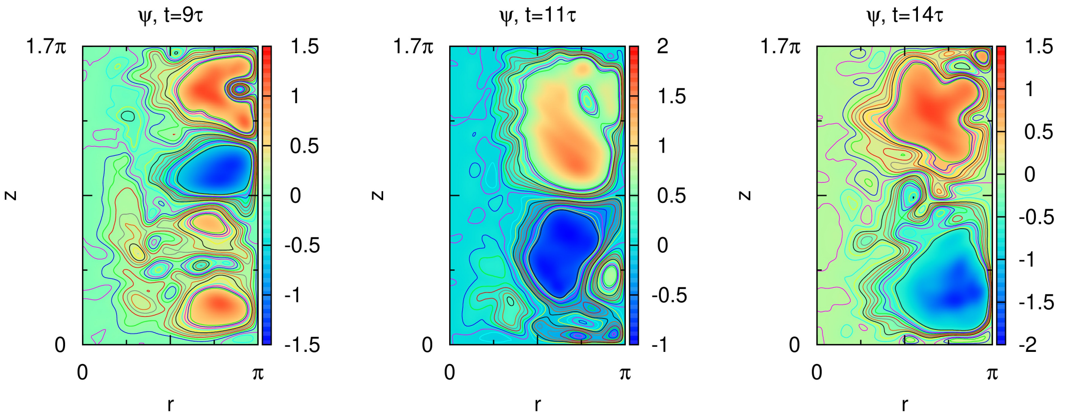

(d) Strong disorder of the flow.

(e) Reorganization into a new dipole.

(f) Tendency of destabilization again.

FIGURE 4.2: Contour plots of the stream function ψ within the poloidal plane $(r, z) \in [0, R] \times [0, H]$ at different times. Both emergence and dissolution of big structures can be observed.

where C_E is the Kolmogorov constant which is expected to be universal, ε is the stationary energy dissipation rate and k is the wave-number.

The cascade of **helicity** is also of interest because it is another invariant in general three-dimensional flows, but its sign is not definite. Brissaud *et al.* [71] first discuss different scenarii in homogeneous isotropic turbulence. For the helicity, the authors propose that H_1 is always transferred in the forward direction ; for the kinetic energy, they propose that the cascade can take place in either the forward or the inverse direction, but in both of the two possibilities the energy cascade obeys the same scaling law (4.2) within the energy inertial range. Further, for the case of direct helicity cascade with inverse energy cascade,

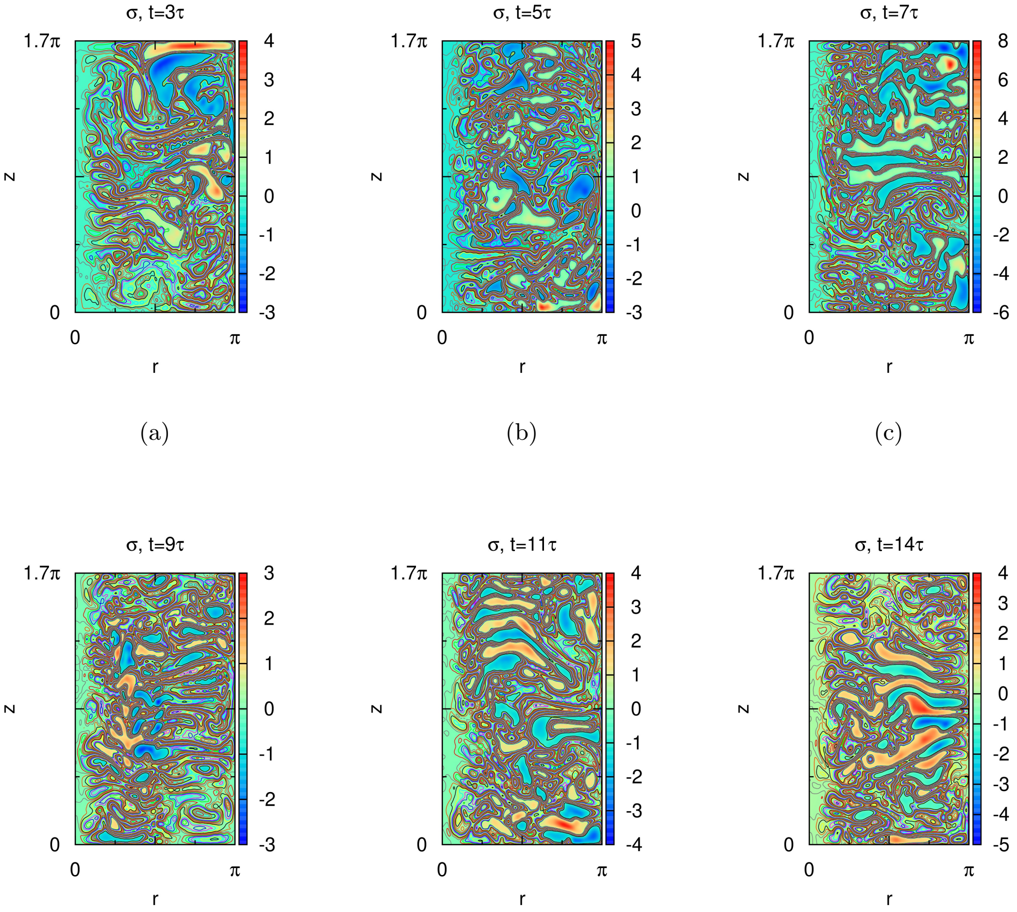

(a) (b) (c)

(d) (e) (f)

FIGURE 4.3: Contour plots of the angular momentum σ within the poloidal plane $(r, z) \in [0, R] \times [0, H]$ at different times. No persistent structure appears.

they suppose that the scaling law for the direct helicity inertial range is

$$H_1(k) \sim \delta^{2/3} k^{-4/3} \Longrightarrow E(k) \sim \delta^{2/3} k^{-7/3}, \tag{4.3}$$

with δ the stationary helicity dissipation rate. However, as pointed out by Chen *et al.* [72], this scaling behavior is generally absent and may appear when the helicity has one single definite sign. The reason of stating this condition is similar to that in two-dimensional turbulence where the enstrophy Z is invariant and positive definite and thus hinders the forward cascade. Numerical illustration of this mechanism is first given by Borue and Orszag [73], and at the same time, simulations therein reveal a coexistence of direct cascades of both energy and helicity with

$$H_1(k) \sim \delta^{2/3} \varepsilon^{-1/3} k^{-5/3}. \tag{4.4}$$

In later investigations, the helicity is divided into its positive and negative contributions

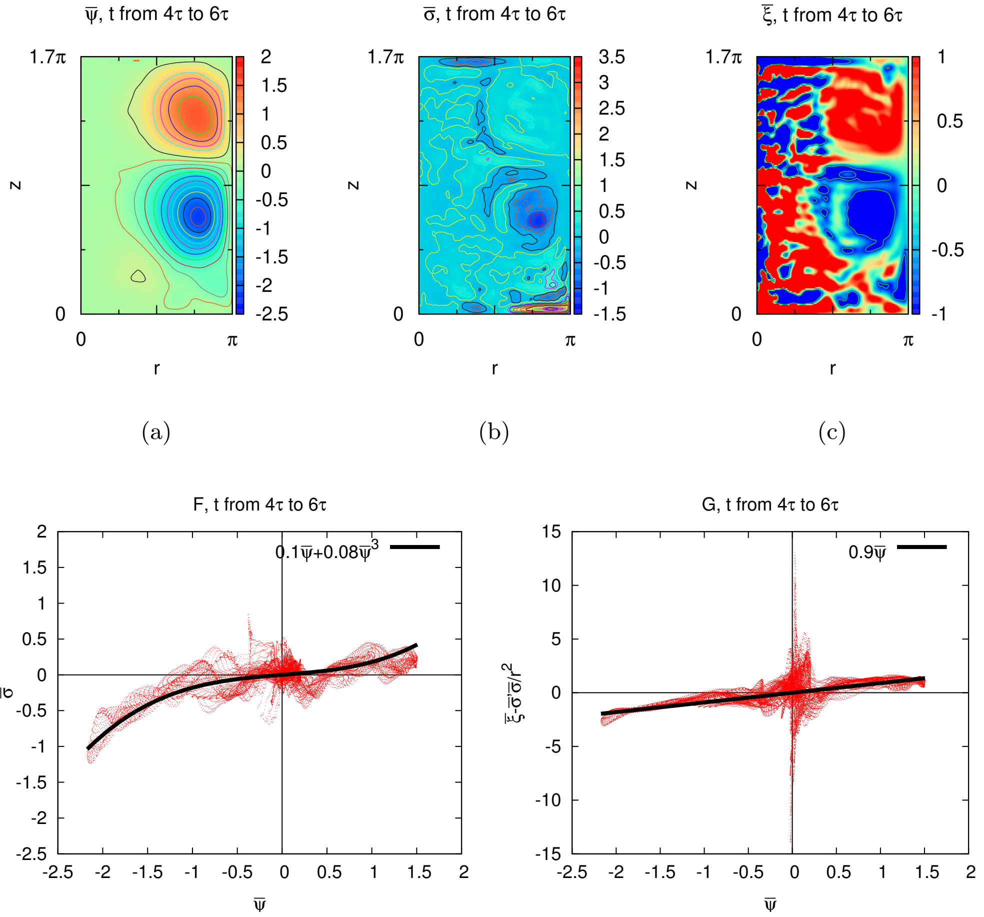

(a) (b) (c)

(d) (e)

FIGURE 4.4: Time-averaged ψ, σ and relationships of $\overline{\sigma} = F(\overline{\psi})$ and $\overline{\xi} - \overline{\sigma}'\overline{\sigma}/r^2 = G(\overline{\psi})$ during $4\tau \leqslant t \leqslant 6\tau$. The scatter plots of functions F and G consider only the points within the bulk of $(r, z) \in [3R/16, 7R/8] \times [H/16, 15H/16]$.

[74, 72], leading to scaling predictions

$$\begin{aligned} E^{\pm}(k) &\sim C_E \varepsilon^{2/3} k^{-5/3} \left[1 \pm \frac{C_{H_1}/C_E}{2k} \left(\frac{\delta}{\varepsilon} \right) \right], \\ \Longleftrightarrow H_1^{\pm}(k) &\sim C_E \varepsilon^{2/3} k^{-2/3} \left[1 \pm \frac{C_{H_1}/C_E}{2k} \left(\frac{\delta}{\varepsilon} \right) \right], \end{aligned} \tag{4.5}$$

with C_{H_1} a constant characterizing the helicity cascade. Biferale *et al.* [75] consider then only one sign of E and H_1 of a homogeneous isotropic flow and observe a local energy cascade in the inverse direction with $E(k) \sim k^{-5/3}$ which corresponds to a direct helicity cascade with $E(k) \sim k^{-7/3}$.

However, **there is no classic theory describing the scaling behavior of axisymmetric turbulence**. In von Kármán flows, where only the average flow is axisymmetric, a -1.7 energy scaling for the direct helicity cascade region is reported experimentally by Pinton and Labbé [76] and by Zocchi *et al.* [77] through local measurements under the Taylor hypothesis. Without using the Taylor hypothesis, Herbert *et al.* [23] show a dual cascade compatible with cascades of E and H_1 in opposite directions : inverse cascade with $E(k) \sim k^{-1}$ and forward cascade with $E(k) \sim k^{-2.2}$ for Re $\geq 10^5$. They explain that such a scaling is compatible with direct cascade of H_1 and inverse cascade of E, associated to the non-locality of the energy transfer. This means that the interaction between big scales and small scales caused by strong shear is an important issue in real von Kármán flows since there are strong mean flows which will not allow the flow to be statistically isotropic. In isotropic 2D turbulence, this distinction between local and non-local transfer and its influence on scaling was investigated in [78]. Numerically, strictly axisymmetric flows with periodic boundary conditions in the axial direction is simulated in Qu *et al.* [8, 9]. The spectrum of a helical case (where H_1 has one single definite sign) is studied and a dual cascade of E and H_1 in opposite directions is also found but with different scaling laws : $E(k) \sim k^{-5/3}$ for E and $E(k) \sim k^{-5.5}$ for H_1, this latter scaling being probably due to the influence of intermittency.

Results

In our case, because the helicity depicted in Fig.4.1 is positive definite, a forward helicity cascade accompanied by an inverse energy cascade can be expected. We then choose the stable period of $4\tau \leq t \leq 6\tau$, and the energy spectrum is shown in Fig.4.6a. This spectrum shows the coexistence of an inverse and of a direct cascade (see "total energy"). These cascades can be better characterized by the averaged energy flux spectrum. Indeed, if one combines the two governing equations in Eq.(3.31), a simpler spectral form can be obtained :

$$\frac{\partial E(k,t)}{\partial t} = T(k,t) - 2\nu k^2 E(k,t) + F(k,t), \tag{4.6}$$

with $T(k,t)$ the transfer spectrum function and $F(k,t)$ the forcing function. Then, the flux spectrum function $\Pi(k)$ can be defined as

$$\Pi(k,t) = \int_0^k T(\kappa,t)\mathrm{d}\kappa, \tag{4.7}$$

and a positive value designates a gain of energy from smaller scales.

The averaged energy flux is shown in Fig.4.5, where a clear positive range of the flux function $\Pi(k)$ for $k < 11$ can be seen. Meanwhile, one observes in Fig.4.5 that there is a rather strong energy cascade in the forward direction, meaning that one has a case with a split energy cascade. It is however possible that at higher Reynolds number only one of these cascades persists. It will be shown in Chapter 5 that in the system of interest, energy can be preferentially transferred towards large scales or towards small scales depending on the ratio between the toroidal and the poloidal energy components E_T/E_P.

In Fig.4.6a, the inverse energy cascade is shown to be compatible with a $-5/3$ scaling in [71] for homogeneous isotropic cases. One remark is that the peak of energy takes place at $k = 2$ corresponding to the size of the dipole structures observed in Fig.4.4a. If one separates the total kinetic energy into its poloidal and toroidal parts as is done in Fig.4.6a, it can be observed that the inverse energy cascade is mainly conducted by the poloidal contribution and that the direct helicity cascade is dominated by the toroidal contribution, and the same observation can be found in [8]. On one hand, the absence of big and persistent structures in contour plots of $\overline{\sigma}$ can be explained by this phenomenon because little toroidal energy is transferred to big scales ; on the other hand, this also leads to the fact that the integral value of E_T is much smaller than E_P, with the ratio

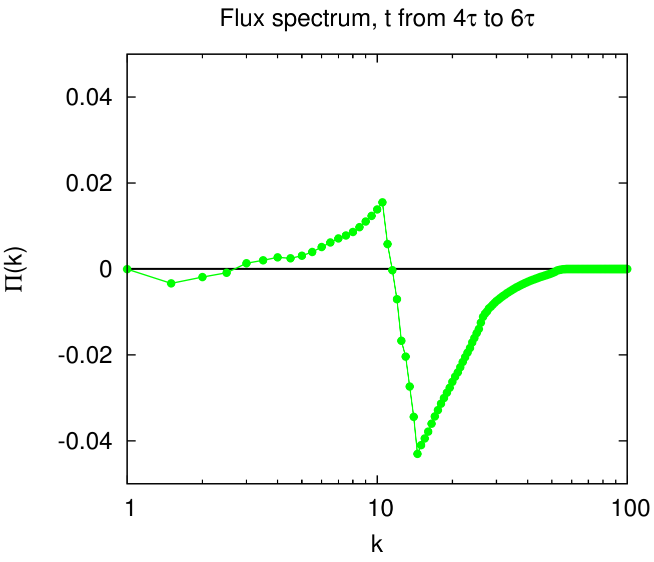

FIGURE 4.5: Time-averaged energy flux spectrum. Both an inverse and a forward energy fluxes are observed.

E_T/E_P estimated to be 0.16, which is similar to that in [8]. In Fig.4.6b, the PDFs of both radial and axial velocity components u_r and u_z are close to a Gaussian distribution, only the azimuthal component exhibits flaring tails, meaning that the intermittency is largest for u_θ. Some scaling laws which are not very clear are proposed in Fig.4.6a. As we will see in the next section, the cascade scaling is even less observable when strong rotation is present in the system. Also, one should always be aware that the effective wave-number k in our context, defined as Eq.(3.35), are considered to be equivalent to, but are in fact different from traditional Fourier wave-numbers, and that there is no theoretical scaling prediction for axisymmetric turbulence. One can also expect that as the Reynolds number gets higher, flatter scaling slopes for the direct helicity cascade may appear.

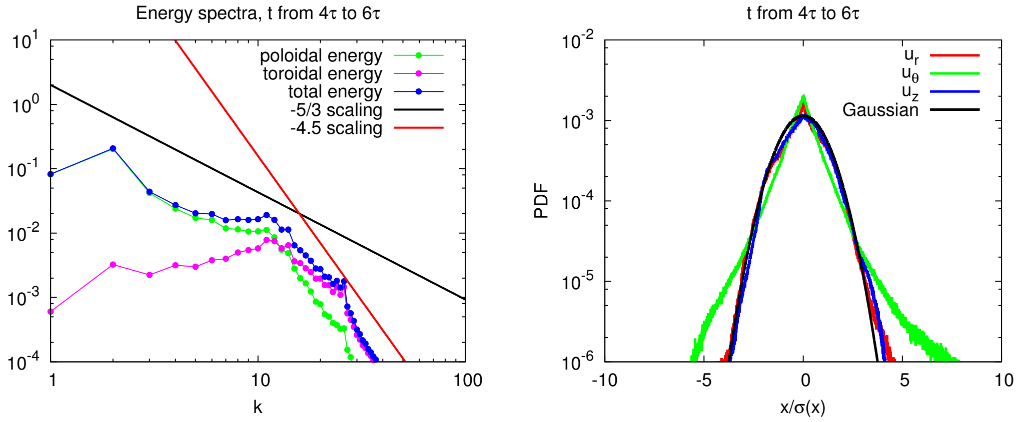

(a) Spectra of E, E_T and E_P. (b) PDFs of velocity components.

FIGURE 4.6: Energy spectra and velocity PDF of a helical case from the FSM code.

Because a higher Reynolds number of axisymmetric flows is reachable by the PSM, in the next section, results of forced PSM cases will be interpreted and compared with the results of this section and with those of experiments.

4.2 Axisymmetric flow generated by counter-rotating discs

In the previous section we used a spectral forcing. In order to approach the experimental boundary conditions, we consider in this section axisymmetric flows which are generated by rotating top and bottom discs. This is performed using the PSM code, again by setting $\alpha = 0$. We remind that the pseudo-spectral method, which is fundamentally different from the fully spectral method, avoids the direct calculation of the convolution product (array (3.28)) in spectral space and therefore needs less computational resources. This allows to attain higher Reynolds numbers. By using Chebyshev polynomials as decomposition basis, more realistic boundary conditions can be achieved, namely solid wall boundaries without penetration nor slip, which is also a difference with the FSM. The forcing which is closer to experiments allows a better comparison with the results from the experiments by Monchaux *et al.* [21]. In [21], the functional relationships of $\sigma = F(\psi)$ and $\xi - F^{'}F/r^2 = G(\psi)$ were investigated. Here we will also focus on these issues. Regarding spectral analysis, the $\mathbf{B}_{qn}$ basis which we used to analyze the spectra in the last section is no longer applicable to decompose the velocity field because $u_\theta \neq 0$ at the top and bottom of the cylinder. But the energy spectra of the central flow bulk can still be studied through the $\mathbf{B}_{qn}$ basis, by excluding the data at boundary areas.

In a real von Kármán device (see Fig.4.7), the cylindrical vessel is equipped with two rotating impellers on the top and the bottom. Each impeller consists of a disc and numerous curved blades. By changing the rotation direction and by tuning the rotation speed of each disc, different scenarii can be achieved, but the most classical scenario is to set up a counter-rotation with the same constant angular velocity. In this thesis, the curved blades are not considered in simulations to avoid meshing difficulty and programming complexity.

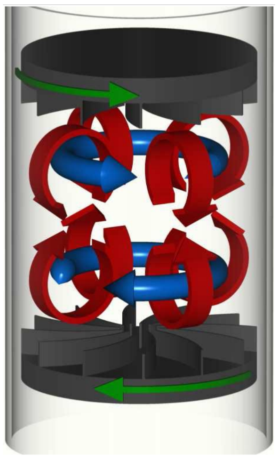

FIGURE 4.7: Picture from [21], representing the working principle of a von Kármán device. Toroidal mean flow is indicated by blue, poloidal mean flow by red arrows.

For experimental details we refer to [21]. There are also many other different experimental set-ups using the von Kármán device. Investigations point out that the essential elements that have crucial effects to the results are the aspect ratio $2R/H$ ([22]), the rotation speed asymmetry ([79]), the blade curvature ([20]) and Reynolds number

([21, 80]). However, Ravelet *et al.* [20] show that even with different curved blades, the scenarii are the same as long as the discs are symmetrically counter-rotating. These conclusions then support the reasonability of comparing our no-blade simulations to experimental flows stirred by impellers, if they share the same aspect ratio and the same symmetrically counter-rotation, and attain sufficiently high Reynolds numbers.

Knowing that the radius of the von Kármán vessel in [21] is $R = 100$ mm and the height (distance between inner faces of impellers) is $H = 180$ mm, in this section we also set the aspect ratio of our computational domain to be $H/R = 1.8$. Precisely we have $R = \pi$ and $H = 1.8\pi$ ($z \in [-0.9\pi, 0.9\pi]$), and collocation point numbers in these two dimensions are $(N, M) = (676, 649)$ yielding a maximal effective wave-number of 650. The time step is fixed as $\Delta t = 5 \times 10^{-5}$ s. The angular velocity of counter-rotating boundaries is fixed as $\Omega = 5$ and the kinematic viscosity as $\nu = 0.002$, yielding a macroscale Reynolds number of $\mathrm{Re}_\Omega \equiv R^2\Omega/\nu = 25000$. We adopt in this section this definition of Reynolds number not only because it appears in the non-dimensional governing equations (and thus in the algorithm), but also due to the fact that it is a common choice for von Kármán experiments. Indeed, it is reasonable because in such cases, R is the forcing scale and ΩR should be the characteristic velocity that determines the energy level. For comparison, if we pick up the definition of the Reynolds number of the FSM section, our $\mathrm{Re}_\Omega = 25000$ is equivalent to $\mathrm{Re} \equiv \sqrt{2E/3}H/\nu = 3170$ at its stationary state, which is 2.5 times higher than that in the last section.

4.2.1 Temporal results

Temporal signals of the statistical quantities and the resolution tests are shown in Fig.4.8. We apply again the typical time τ calculated by Eq.(4.1) to normalize the physical time. All of these quantities of E, H_1, I_1, I_2 and H_0 are rather well conserved after $t = 53\tau$. Particularly, it is expected that I_1 converges finally to 0 because the angular momentum is largely generated by the rotating discs, and in our case the discs are strictly counter-rotating. The curves of the resolution tests tell that the current spatial resolution is sufficiently fine. Because coherent structures are predicted by statistical mechanics theories of the Euler equations, and more precisely that symmetric counter-recirculating toric cells are reported in experiments, it will be interesting to see whether the simulated flow reproduces these structures. Contour plots of ψ and σ at different times are presented in Figs.4.9 and 4.10, showing the stability of the structures of both variables. Indeed, since in this case the forcing is well localized in space, the applied big scale injection may be less destabilizing than the spectral forcing used in the previous section. The shear layer in the middle that delimits the two recirculating cells is not static and moves in a chaotic manner around its average position at $z = 0$, which is in agreement with experimental observations [21]. Further, compared to Figs.4.2 and 4.3 of the last section, there turns out to be a higher coherence between instantaneous values of ψ and σ, and thus better fittings for the averaged functional relationships of $F(\overline{\psi})$ and $G(\overline{\psi})$ can be expected.

4.2.2 Time-averaged results

Because the flow is statistically stationary after $t = 53\tau$, an averaging operation is applied to the evolution in the time interval of 53τ till the end of 97τ. Averaged contour pictures of $\overline{\psi}$ and $\overline{\sigma}$ (within the entire domain) are given in Figs.4.11a, 4.11b and 4.11c.

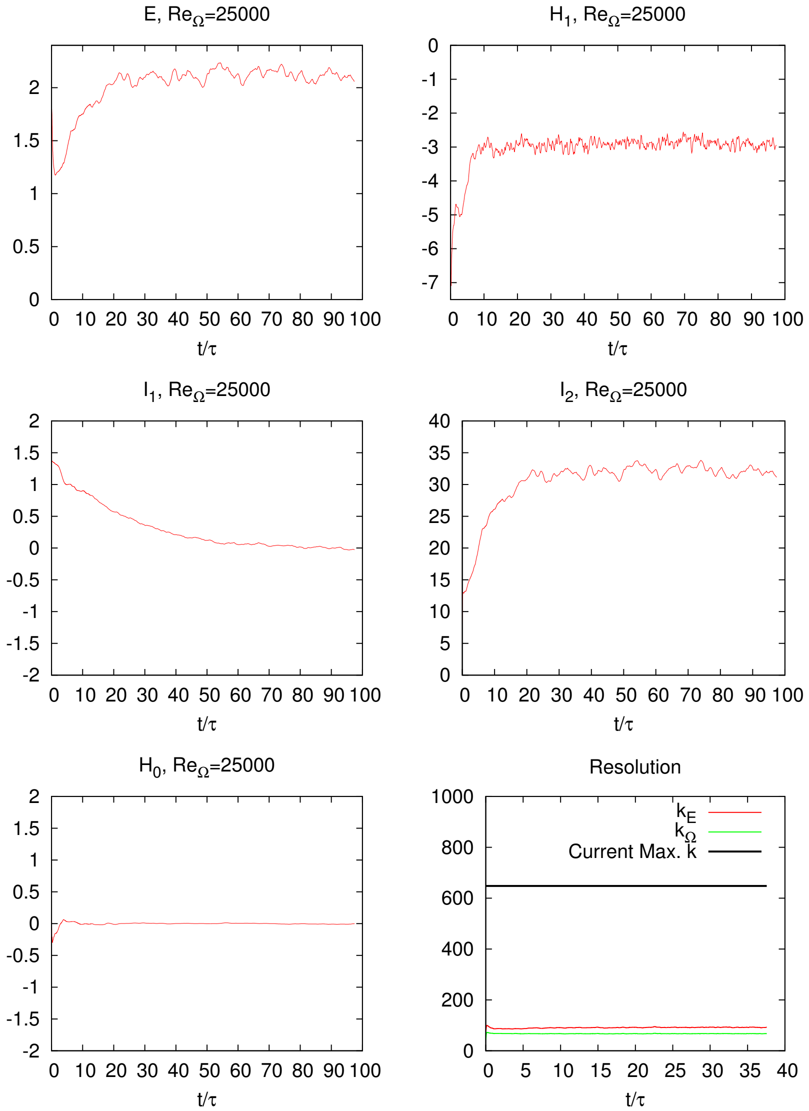

FIGURE 4.8: Temporal signals of statistical invariants and resolution tests for a forced simulation. As explained in Appendix C, the dissipation rate of I_1 and H_1 in a mechanically forced case are not well defined, and hence only the energy and enstrophy dissipation rates are used to check the resolution.

Coherent structures can be observed for both $\overline{\psi}$ and $\overline{\sigma}$. For $\overline{\xi}$, the structures are difficult to detect since there are extreme value appearing at $r \approx 0$. However, when the color scales are adapted to zoom on smaller values, the vorticity structures resemble those of $\overline{\psi}$. The averaged fields in [21] are shown in Fig.4.12. One can see that the structures of our case are very similar to those in [21], and that both of them are located in areas close to the lateral wall and occupy a radial extent of $R/2$. As for scatter plots of $F(\overline{\psi})$ and $G(\overline{\psi})$, the same principle as that in [21] is adopted to use only the central flow bulk data of $r \leq 0.81R$ and $-0.56H/2 \leq z \leq 0.56H/2$. Indeed, boundary areas are locations where viscous effects, strong shears and impeller stirring take place and may lead to obvious deviations from theoretical predictions considering Euler equations which are inviscid and unforced. Scatter plots concerning the flow bulk as well as the fittings obtained via the least square method are presented in Figs.4.11d and 4.11e. A high similarity between them and those of [21] can be seen : they are all cubic and the fittings of G of both possess a

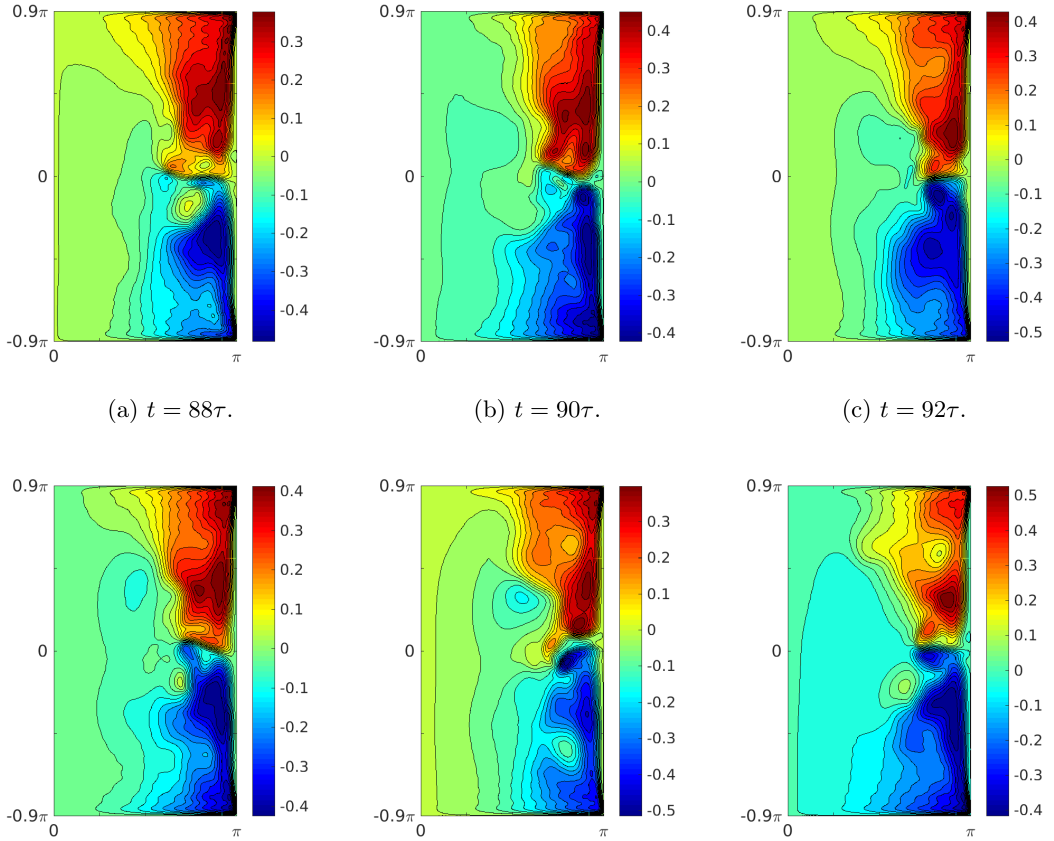

(a) $t = 88\tau$.

(b) $t = 90\tau$.

(c) $t = 92\tau$.

(d) $t = 94\tau$.

(e) $t = 96\tau$.

(f) $t = 97\tau$.

FIGURE 4.9: Contour plots of the stream function ψ within the poloidal plane $(r, z) \in [0, R] \times [0, H]$ at different times.

horizontal band of zero. Compared to those of the FSM in the last section, the current functional fittings are much neater and clearer. The fitting of $\overline{\sigma} = F(\overline{\psi})$ appears to be in a cubic form of $F(\overline{\psi}) = -41882\overline{\psi}^3 + 2.05\overline{\psi}$ which is compatible with the observation in [21]. The fitting of $\overline{\xi} - \overline{\sigma}'\overline{\sigma}/r^2 = G(\overline{\psi})$ turns out to be $G(\overline{\psi}) = -346020\overline{\psi}^3 + 15.16\overline{\psi}$, and exhibits a wide range of $G(\overline{\psi}) = 0$.

Low Reynolds numbers results

For comparison, we now investigate the effect of Reynolds number. For this, we also give the results of cases of which the kinematic viscosity is respectively 10 times and 100 times greater, corresponding to $\mathrm{Re}_\Omega = 2500$ and $\mathrm{Re}_\Omega = 250$. For these flows, coherent structures and functional relationships can still be observed. Tendencies (see respectively Fig.4.13 and Fig.4.14) are that as Re_Ω gets smaller, coherent structures become more circular, and the functional relationships progressively disappear, as expected since the flow is not expected any more to be a solution of the Euler equations.

4.2.3 Energy spectra of central flow bulk

On one hand, the modes of Chebyshev polynomials are not as intuitive as those of the FSM, let alone the comparison to wave-numbers of the Fourier transform. The Chebyshev modes cannot be directly linked with physical length scales, which can be reflected from

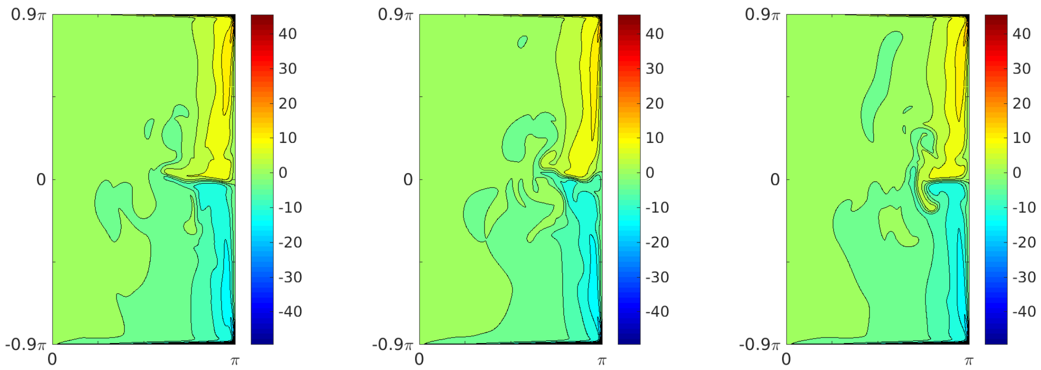

(a) $t = 88\tau$. (b) $t = 90\tau$. (c) $t = 92\tau$.

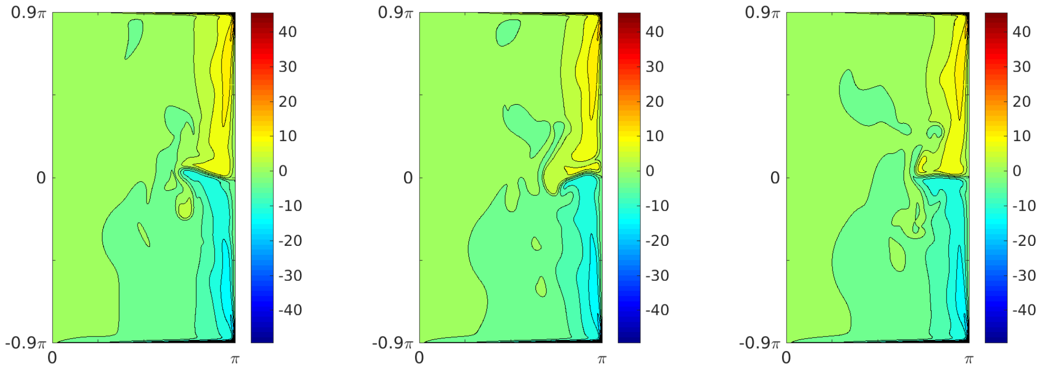

(d) $t = 94\tau$. (e) $t = 96\tau$. (f) $t = 97\tau$.

FIGURE 4.10: Contour plots of the angular momentum σ within the poloidal plane $(r, z) \in [0, R] \times [0, H]$ at different times.

the fact that the Gauss-Lobatto collocation points are not equi-distant. On the other, the $\mathbf{B}_{qn}$ basis derived in FSM part is no longer complete for a decomposition of a velocity field of which $u_\theta \neq 0$ on the top and the bottom of the cylinder. However, if one chooses to consider only the velocity field of the flow bulk, $\mathbf{B}_{qn}$ is again valid to decompose the filtered velocity field. Since the temporal signal of the helicity H_1 in Fig.4.8 possesses one single definite sign (effect of the formation of toric recirculating cells resulting in the alignment of $\mathbf{u}$ and $\boldsymbol{\omega}$), one can imagine that there might be a similar dual cascade : forward for the helicity and inverse for the energy. The spectra concerning the flow bulk are depicted in Fig.4.15. Almost all of the energy is contained in the toroidal component. A flatter slope is observed for $k \leq 15$ and a steeper slope of -3 controls the region of $k \geq 20$. These slopes can be reasonably associated to inverse and direct cascades, respectively. However, the Reynolds number is too low and the scaling ranges consequently too small to accurately assess asymptotic scaling. Indeed, these slopes are different from existing theoretical attempts, experimental observations and numerical estimations. First, they are not compatible with $-5/3$ and $-7/3$ scalings in [75] that treats isotropic flows obtained from decimated Navier-Stokes equations. Second, they are different from the -1 and -2.2 power laws in [23]. Indeed, although the flow investigated in this section is also subjected to strong mean motions and should have strong non-locality, there is a difference between the flows in [23] and our simulated flow : in [23], the radial and azimuthal energy components are of the same order and are one-order greater than

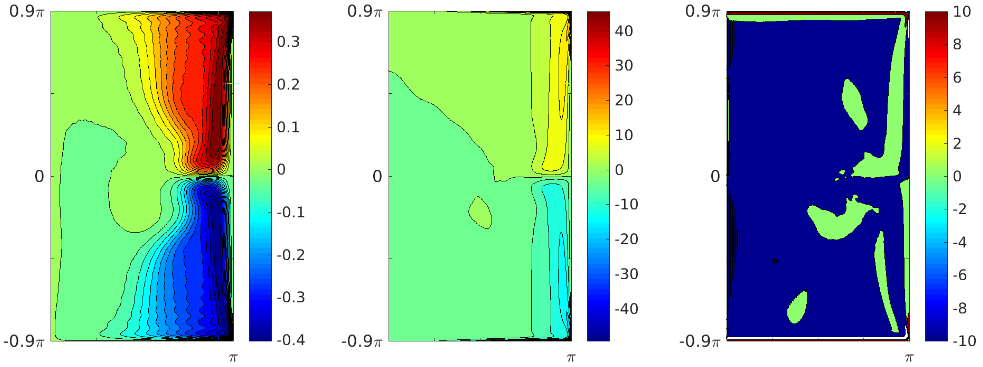

(a) $\overline{\psi}$ (b) $\overline{\sigma}$ (c) $\overline{\xi}$

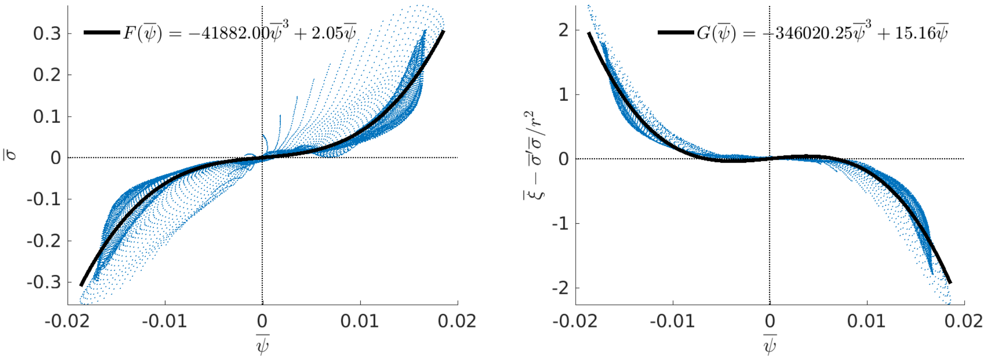

(d) (e)

FIGURE 4.11: Time-averaged ψ, σ and relationships $\overline{\sigma} = F(\overline{\psi})$ and $\overline{\xi} - \overline{\sigma}'\overline{\sigma}/r^2 = G(\overline{\psi})$ during $53\tau \leq t \leq 97\tau$ for $\mathrm{Re}_\Omega = 25000$. The scatter plots of functions F and G consider only the points within the region of $(r, z) \in [0, 0.81R] \times [-0.56H/2, 0.56H/2]$.

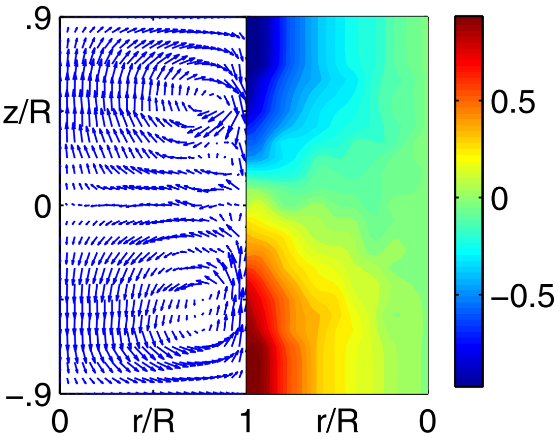

FIGURE 4.12: Pictures cited from [21] showing time-averaged fields. Time-averaged ψ and u_θ for $\mathrm{Re}_\Omega = 2.5 \times 10^5$. The arrow plot represents the $\overline{\psi}$ field and the colored contour displays the $\overline{u}_\theta$ field.

the axial energy component, while in our case, the toroidal (azimuthal) component is one-order more intensive than the poloidal (radial + axial) component. Third, the slopes seen in Fig.4.15 are different to those obtained by FSM either in [8] or in the last section

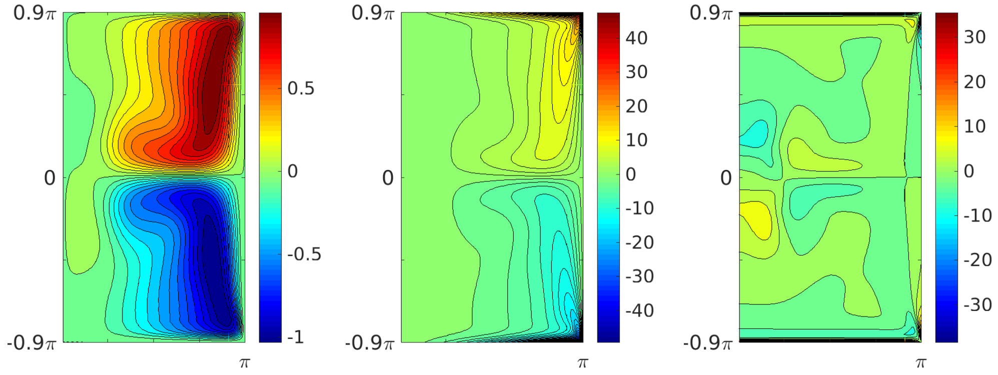

(a) $\overline{\psi}$ (b) $\overline{\sigma}$ (c) $\overline{\xi}$

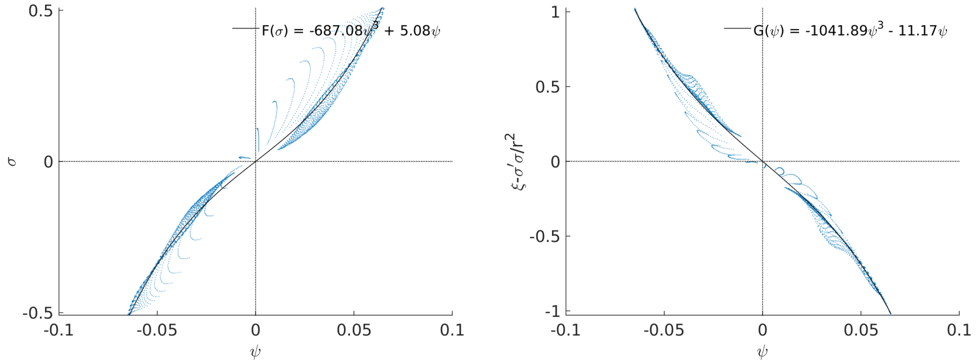

(d) (e)

FIGURE 4.13: Time-averaged ψ, σ and relationships $\overline{\sigma} = F(\overline{\psi})$ and $\overline{\xi} - \overline{\sigma}'\overline{\sigma}/r^2 = G(\overline{\psi})$ during the stationary state for $\mathrm{Re}_\Omega = 2500$. The scatter plots of functions F and G consider only the points within the bulk of $(r, z) \in [0, 0.81R] \times [-0.56H/2, 0.56H/2]$.

of this thesis. One can note that in either the case of [8] or the case in the last section, the poloidal energy component is more important than the toroidal, but the situation is reversed in the current simulation due to the presence of a strong counter-rotation. A supposition can be put forward that in axisymmetric flows, the scaling behavior is highly dependent on the energy distribution among the radial, azimuthal and axial directions, and can be significantly affected by the adopted filtering principles. At least, the former half of this supposition will be confirmed by simulations presented in the next chapter.

4.3 Summary

In this chapter, we compare the results of both the FSM and the PSM to those of existing studies. Coherent structures are observed in both instantaneous and averaged fields, in agreement with theoretical predictions and experimental observations. Functional relationships are clear in averaged fields of off-boundary flow bulks, and are particularly clear in the PSM results where a higher Reynolds number is reached and the flow is forced by rotating discs rather than by a spectral forcing. This is the first time that the existence of such coherent structures and associated relationships is evidenced in strictly axisymmetric forced turbulence (in literature, experimental results were obtained

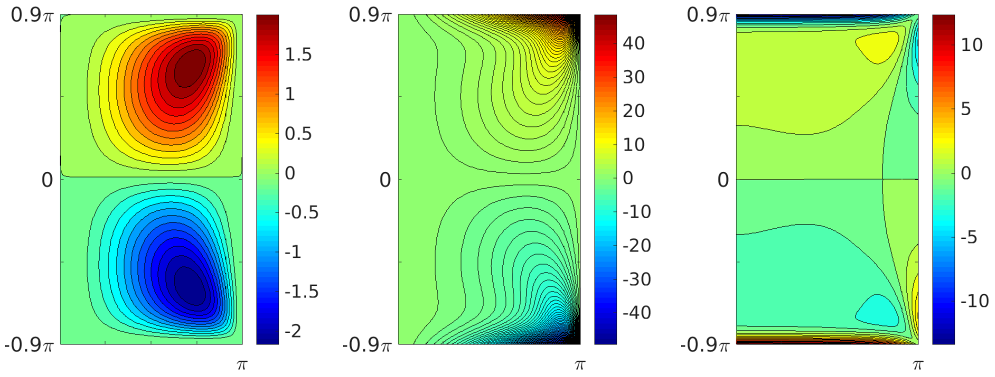

(a) $\overline{\psi}$ (b) $\overline{\sigma}$ (c) $\overline{\xi}$

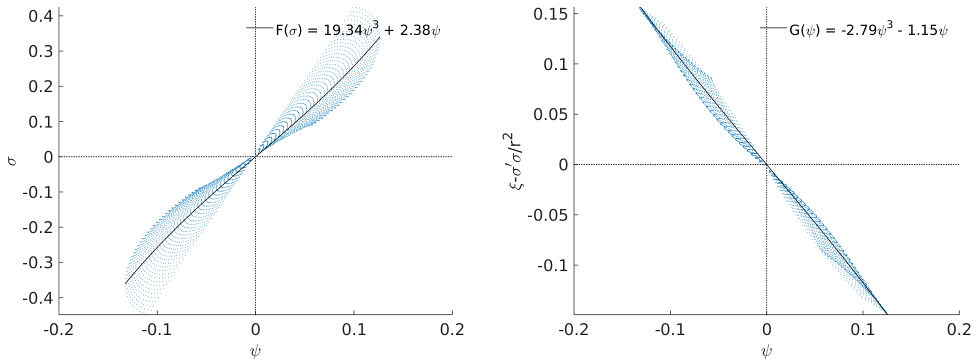

(d) (e)

FIGURE 4.14: Time-averaged ψ, σ and relationships $\overline{\sigma} = F(\overline{\psi})$ and $\overline{\xi} - \overline{\sigma}'\overline{\sigma}/r^2 = G(\overline{\psi})$ during the stationary state for $\mathrm{Re}_\Omega = 250$. The scatter plots of functions F and G consider only the points within the bulk of $(r, z) \in [0, 0.81R] \times [-0.56H/2, 0.56H/2]$.

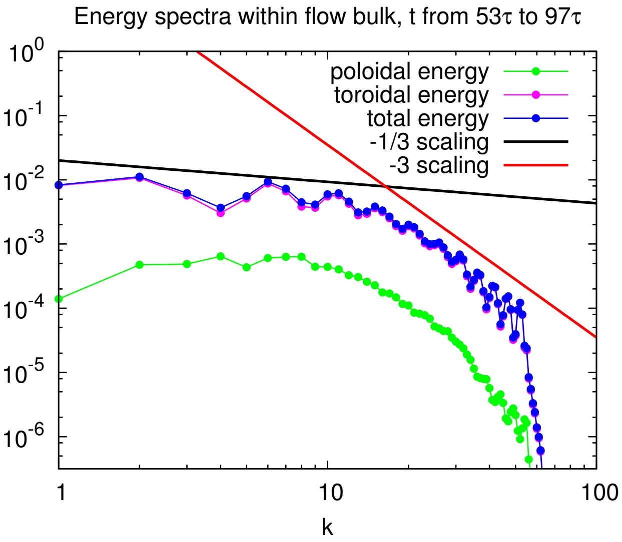

FIGURE 4.15: Comparison of bulk energy spectra. The flow bulk is defined as $(r, z) \in [0, 0.81R] \times [-0.56H/2, 0.56H/2]$.

in statistically axisymmetric turbulence, numerical results in freely decaying turbulence).

Energy spectra and scaling behaviors are particularly discussed in parallel with a succinct review of relative theoretical, experimental and numerical works in literature. For the results issuing from the FSM, the extracted scaling slopes are comparable to those obtained by Qu *et al.* [8, 7, 9]. As for the PSM part, the extracted scaling slopes differ from the reported results in [75, 23]. We suspect that spectra scalings of von Kármán turbulence depend on the energy distribution among the radial, azimuthal and axial components. Let us recall that the numerical and experimental Reynolds numbers are also very different.

The comparison and agreement of the two parts serve us as confirmation of the reliability of the two codes. This step of validation is important because the codes will be used for other studies, concerning the transition behavior from non-swirling axisymmetric flows to swirling axisymmetric flows (see Chapter 5) and the transition from strictly axisymmetric flows to general cylindrical 3D flows (see Chapter 6). Simulations from non-swirling to swirling axisymmetric flows will be conducted by using the FSM code, while the simulations from strictly axisymmetric flows to general cylindrical 3D flows will be conducted by using the PSM code.

Chapitre 5

Transition from Non-swirling to Swirling Axisymmetric Turbulence

The work presented in this chapter was done in collaboration with Bérengère Dubrulle (SPEC, CEA Saclay) and Hugues Faller (LIMSI). The present chapter is the copy of an early version of a manuscript in preparation, which will be shortly submitted to Physical Review Fluids : Z. Qin, H. Faller, B. Dubrulle, A. Naso and W. Bos, *Transition from non-swirling to swirling axisymmetric turbulence.*

5.1 Introduction

Transitions between different states of fluid flow have been intensively studied since the work of Osborne Reynolds, who systematically characterized the transition from laminar to turbulent pipe flow [81]. In that transition, the control parameter which allows to switch from one state to another is the Reynolds number. More recently, transitions between different turbulent states have received attention [26]. For instance, the transition between two- and three-dimensional turbulence was first investigated by Frisch, Lesieur and Sulem [40]. The control parameter used in this work was the flow dimensionality D, and the authors reported that the energy cascade direction (forward in three dimensions, backward in two dimensions) changes for a value of D close to 2. Transitions between different turbulent states have recently received even more attention, in particular in the context of thin fluid layers [28, 29], where the control parameter is the ratio between the thickness of the fluid layer and the scale at which energy is injected. In these numerical investigations the Navier-Stokes equations were integrated in a periodic domain, and the only external force to which the flow was subject was the forcing.

A distinct manner to influence the effective dimension of a turbulent flow consists in applying anisotropic body forces. For instance, a recent investigation showed the existence of a subcritical transition in rotating Rayleigh-Bénard convection [82], where a condensate appears for a particular choice of the control parameters. Other examples are the application of a magnetic field on a conductive fluid, resulting in the appearance of the Lorentz force, or the application of a solid body rotation, introducing the Coriolis force in the momentum balance [83]. When the order of magnitude of these forces becomes large compared to that of the inertial ones, the flow becomes invariant, or almost, along the direction of the magnetic field or of the rotation axis, respectively. These two configurations therefore exhibit transitions from three-dimensional three-velocity-component (3D3C) to two-dimensional three-velocity-component (2D3C) turbulent flows. In other words, the flows in these examples have three non-zero velocity components, but these three components can vary either in the three dimensions or in a plane only (perpendicular to the axis of rotation or to the magnetic field).

A different transition between turbulent states is the transition from a 3D3C to a three-dimensional two-component (3D2C) flow. A typical example is strongly stratified turbulence, in which the dynamics is almost entirely confined in the plane perpendicular to the imposed density gradient, but these two velocity components vary strongly in the three directions [84].

In the present work we will investigate by direct numerical simulation a transition from 2D2C to 2D3C turbulence. This transition occurs in strictly axisymmetric turbulence, solution of the Navier-Stokes equations modified such that the flow is invariant in the azimuthal direction. This system is intermediate between two- and three-dimensional turbulence, and was recently investigated by direct numerical simulation (DNS). It was shown in particular that an inverse energy cascade, responsible for the generation of large scale coherent structures, and a direct helicity cascade towards small scales can coexist in this flow [7, 9]. As predicted from theoretical works using statistical mechanics tools [6, 85, 22], different behaviors were obtained for non-swirling (zero azimuthal velocity component) and for swirling flows. We investigate here the transition from the non-swirling (two-dimensional two-component, 2D2C) to the swirling (two-dimensional three-component, 2D3C) regime.

The chapter is organized as follows. We first recall the definition of strictly axisymmetric turbulence and give some definitions in Section 5.2. The numerical method and the results of the simulations carried out are presented in Section 5.3. A statistical model is derived and its results are compared with these numerical data in Section 5.4. Finally, our conclusions are reported in Section 5.5.

5.2 Axisymmetric turbulence

We consider incompressible, Newtonian and isothermal axisymmetric turbulence. The flow is confined in a cylindrical domain of radius R and of axis length H, and is solution of the Navier-Stokes equations written in cylindrical coordinates (r, θ, z) for the three velocity components $\boldsymbol{u} = (u_r, u_\theta, u_z)$. The system is assumed invariant in the toroidal direction. In practice, this means that $\boldsymbol{u} = (u_r(r,z), u_\theta(r,z), u_z(r,z))$ and that the pressure $p = p(r,z)$, so that any toroidal variation $\partial_\theta(\boldsymbol{u}, p)$ is zero. All external effects which can inject energy into the system in this simplified system are modelled by a forcing term added in the momentum equation. Under these assumptions, the flow is solution of the following system of equations :

$$D_t[u_r] \quad = \quad f_r + \nu\Delta_r u_r - \frac{1}{\rho}\partial_r p + \frac{u_\theta^2}{r}, \tag{5.1}$$

$$D_t[u_z] \quad = \quad f_z + \nu\Delta_z u_z - \frac{1}{p}\partial_z p, \tag{5.2}$$

$$D_t[u_\theta] \quad = \quad f_\theta + \nu\Delta_\theta u_\theta - \frac{u_r u_\theta}{r}, \tag{5.3}$$

where the operator D_t is defined as

$$D_t[g] = \partial_t g + u_r\partial_r g + u_z\partial_z g, \tag{5.4}$$

ρ is the fluid density, ν its kinematic viscosity, and Δ_i are the three components of the cylindrical vector Laplacian. Incompressibility is ensured by the relation

$$\frac{1}{r}\partial_r(ru_r) + \partial_z u_z = 0. \tag{5.5}$$

The forcing $\mathbf{f}$ considered in this investigation is based on the negative viscosity method [65] and will be defined more precisely later on.

We will distinguish throughout this study the poloidal plane (r, z) from the toroidal (azimuthal) direction. The interaction between the toroidal and the poloidal dynamics is represented by the last terms on the right-hand sides of Eqs.(5.1) and (5.3). These coupling terms will be of major importance in the following. A simple measure of the flow dimensionality is the ratio $\gamma = \overline{E}_T/\overline{E}_P$, where E_T and E_P respectively denote the toroidal and poloidal components of energy :

$$E_T = \frac{\langle u_\theta^2 \rangle}{2}, \tag{5.6}$$

$$E_P = \frac{\langle u_r^2 + u_z^2 \rangle}{2}, \tag{5.7}$$

and $\langle ... \rangle$ are volume averages. If $\gamma = 0$ the flow is purely poloidal ($u_\theta = 0$), whereas if $\gamma > 0$ toroidal and poloidal velocity fluctuations coexist. These energy components are solutions of equations that can be derived from the Navier-Stokes equations (5.1-5.5) and formally write :

$$\frac{\mathrm{d}E_P}{\mathrm{d}t} = F_P - \varepsilon_P + T, \tag{5.8}$$

$$\frac{\mathrm{d}E_T}{\mathrm{d}t} = F_T - \varepsilon_T - T, \tag{5.9}$$

where ε_P and ε_T are viscous dissipation terms ($\varepsilon_P, \varepsilon_T > 0$), F_P and F_T are forcing terms ($F_P, F_T > 0$), and the transfer from the toroidal to the poloidal energy components is (deduction in Appendix E.1) :

$$T = \left\langle \frac{u_\theta^2 u_r}{r} \right\rangle. \tag{5.10}$$

5.3 Numerical simulations

5.3.1 Method and parameters

The Navier-Stokes equations (5.1-5.5) were integrated by using a fully spectral method based on an expansion of the velocity field in a basis consisting of a combination of Fourier modes in the axial direction and of Bessel functions in the radial one [7] (the code is based on the original design of [58]). In this approach, n and q are the mode-numbers respectively associated to the axial and radial directions, k_n being the axial wave-number and γ_q the qth zero of the Bessel function J_1 in the radial direction. This allows to define a global wave-number defined as $k(n, q) = (k_n^2 + \gamma_q^2)^{1/2}$. As already mentioned, use was made of the negative viscosity method [65] :

$$\hat{f}_i(k) = c_i \nu h(k) \hat{u}_i(k), \quad i \in \{r, \theta, z\}, \tag{5.11}$$

where $\hat{g}$ denotes the spectral coefficient associated with a function $g(r, \theta, z)$, $h(k) = k^2$ for $k_{f,\min} \leqslant k \leqslant k_{f,\max}$ and zero elsewhere, and c_i is a dimensionless forcing coefficient measuring the intensity of energy injection in the i direction ($i \in \{r, \theta, z\}$). Contrary to the configuration investigated in [7, 9], in which the flow was periodic in the axial direction, we imposed a confinement of the fluid in the cylindrical domain by using a suitable choice of the axial mode-numbers n.

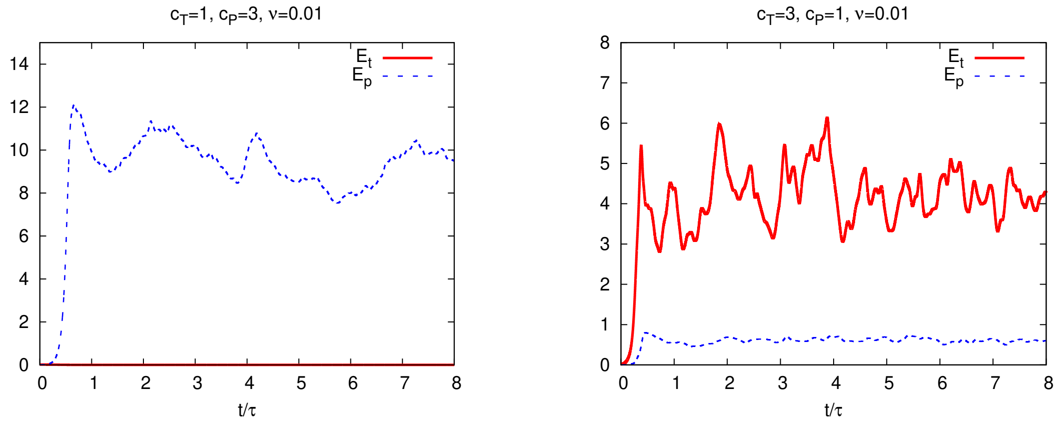

(a) (b)

FIGURE 5.1: Time evolution of the poloidal and toroidal energy components for : (a) $c_P = 3$, $c_T = 1$ ($c_T/c_P = 1/3$) and (b) $c_P = 1$, $c_T = 3$ ($c_T/c_P = 3$). Time is normalized by $\tau = R/(2\overline{E}/3)^{1/2}$, where $\overline{E}$ is the total kinetic energy of the flow time-averaged in the statistically steady state.

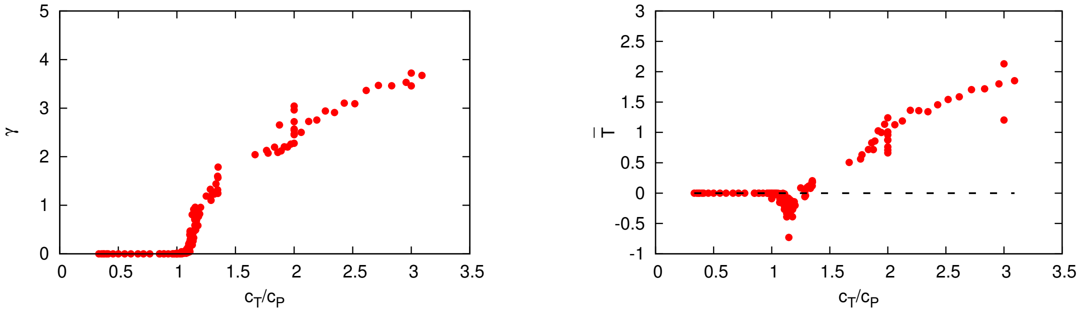

(a) (b)

FIGURE 5.2: (a) Ratio between the energy components time-averaged during the steady state, $\gamma = \overline{E}_T/\overline{E}_P$, plotted as a function of the forcing parameters ratio, c_T/c_P, for the complete set of simulations. (b) Transfer from the toroidal to the poloidal energy components, $\overline{T} = \overline{\langle u_\theta^2 u_r/r \rangle}$, plotted as a function of c_T/c_P.

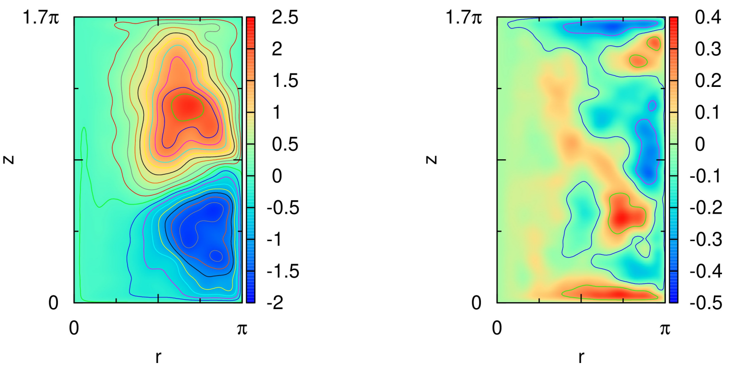

(a) (b)

FIGURE 5.3: Contour plots of the time-averaged poloidal stream function ψ defined as : $u_r = -\partial_z\psi/r$, $u_z = \partial_r\psi/r$. The average is performed during the statistically steady state. The time interval over which ψ is averaged is (a) $4 < t/\tau < 16$ and (b) $9 < t/\tau < 22$. Forcing parameters are : (a) $c_P = 3$, $c_T = 1$ ($c_T/c_P = 1/3$) and (b) $c_P = 1.2$, $c_T = 3.6$ ($c_T/c_P = 3$).

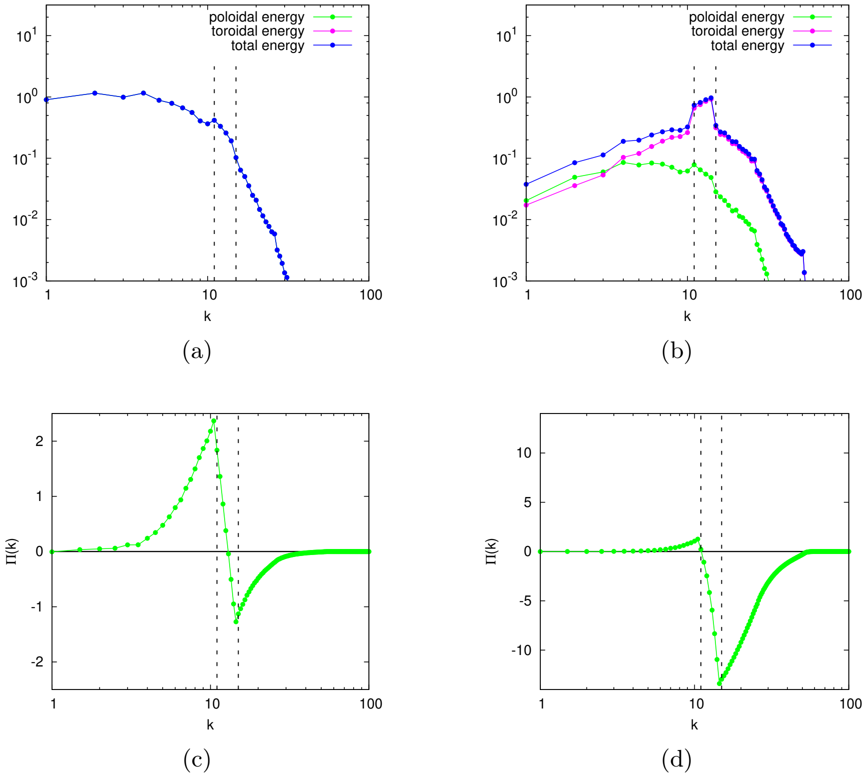

FIGURE 5.4: Time-averaged (a,b) energy spectra of the total, poloidal and toroidal energy, and (c,d) energy flux. Values of the forcing parameters : (a,c) $c_P = 3$, $c_T = 1$ ($c_T/c_P = 1/3$), (b,d) $c_P = 1.2$, $c_T = 3.6$ ($c_T/c_P = 3$). The vertical dashed lines indicate the range of wave-numbers in which forcing is applied.

More than 150 simulations were carried out in a cylindrical domain of radius $R = \pi$ and height $H = 1.7\pi$. In all of them the viscosity was set to $\nu = 0.01$. Calculations were performed using 52 modes in the radial direction and 45 modes in the axial one. The forcing band, $11 \leqslant k \leqslant 15$, corresponds to scales intermediate in size between the dissipation scale and the cylinder size, as in [9], which allows for the existence of cascades towards both small and large scales. The forcing coefficients were set such that $c_r = c_z \equiv c_P$ and $c_\theta \equiv c_T$. The values of c_P and c_T were both chosen in the interval $[1, 3.6]$. Statistically steady states were reached in all cases. The results presented in the following subsection were obtained during them.

5.3.2 Numerical results

We first show in Fig.5.1 the time evolution of the poloidal and toroidal energy components, for two distinct choices of the forcing parameters such that $c_T/c_P = 1/3$ and $c_T/c_P = 3$ respectively. Statistically steady states are observed after a transient time. In this regime, although both energy components fluctuate around finite values when $c_T/c_P = 3$ (Fig.5.1(b)), the toroidal energy component E_T is found to be zero for $c_T/c_P = 1/3$ (Fig.5.1(a)). In the latter case, the flow therefore remains 2D2C, without swirl ($u_\theta = 0$).

A more refined information is provided in Fig.5.2(a), in which the ratio between the toroidal and poloidal energy components time-averaged during the statistically state, γ, is plotted as a function of the ratio c_T/c_P (in the range of c_T and c_P values considered here, γ depends only on the *ratio* of these parameters). A transition from a 2D2C ($E_T = 0$) to a 2D3C ($E_T \neq 0$) state, occurring for $c_T/c_P \approx 1$, is clearly visible. For weak toroidal forcing, the flow is purely poloidal, governed by purely two-dimensional dynamics. We recall here that axisymmetric turbulence can, in the absence of toroidal fluctuations, be reformulated, using a suitable change of variables, as purely Cartesian two-dimensional turbulence [86, 87]. When $c_T/c_P \approx 1$, a sharp transition is observed towards a swirling state, where both toroidal and poloidal velocity components are finite.

The different natures of the flows for $c_T/c_P < 1$ and $c_T/c_P > 1$ are also illustrated in Fig.5.3, in which the poloidal flow time-averaged during the stationary state is shown. Coherent large-scale structures reminiscent of two-dimensional turbulence are clearly visible in the case $c_T/c_P < 1$ (Fig.5.3(a)), which is not the case when $c_T/c_P > 1$ (Fig.5.3(b)), whatever the time interval chosen. The exact type of structures obtained in the former case may depend on the time interval chosen, as is well known in forced two-dimensional wall-bounded turbulence [88].

Finally, we illustrate the different dimensionalities of the flows for $c_T/c_P < 1$ and $c_T/c_P > 1$ by showing in Fig.5.4(a,b) energy spectra. When $c_T/c_P < 1$ (Fig.5.4(a)), a clear signature of an inverse energy cascade is observed, unlike in the case $c_T/c_P > 1$ (Fig.5.4(b)). This result is confirmed in Fig.5.4(c,d), in which the energy flux is shown. For the purely poloidal flow (Fig.5.4(c)), an important part of the energy is transferred to lower wave-numbers. This is not the case in the swirling regime (Fig.5.4(d)), where the energy flux is predominantly directed towards the large wave-numbers.

To summarize, we have shown numerically the existence of a transition from 2D2C to 2D3C turbulent flows. The control parameter of this transition is the ratio between the forcing coefficients, c_T/c_P, the transition occurring for $c_T/c_P \approx 1$. The order parameter is the ratio between the toroidal and poloidal components of energy, γ, which measures the flow "componentionality" : 2D2C for $\gamma = 0$, 2D3C for $\gamma \neq 0$. We now derive a model allowing to reproduce this transition. A crucial term to model is the transfer from the toroidal to the poloidal energy components, T, defined in Eq.(5.10). This term was calculated by direct numerical simulation ; its time-average in the statistically steady state is plotted as a function of c_T/c_P in Fig.5.2(b). For $c_T/c_P < 1$ (2D2C turbulence), no transfer occurs between both flow components, as expected. For $1 < c_T/c_P \lesssim 1.3$, energy is preferentially transferred from the poloidal to the toroidal fields ($\overline{T} < 0$, the poloidal field "feeds" the toroidal one), whereas for higher values of c_T/c_P it is transferred from the toroidal to the poloidal directions ($\overline{T} > 0$).

5.4 Statistical model

In order to elucidate the nature of the transition, we developed a statistical model of the dynamics. Our aim was to derive the simplest possible model able to capture the steady states of the system (5.8-5.9), by estimating the five terms appearing on the right-hand sides of these equations.

The derivation of the statistical model is presented in Section 5.4.1-5.4.3. The values of its free parameters are then determined in Section 5.4.5, by using the direct numerical simulation data. We finally calculate analytically, in Section 5.4.6, the stationary solutions E_P and E_T of the model, and compare them to the direct numerical simulations results.

5.4.1 Dissipation modelling

We first estimate the viscous dissipation terms ε_P and ε_T. Even though the Reynolds number of our simulations is only moderate, we will use for the sake of simplicity arguments in principle valid for high Reynolds number flows. In this regime, the dissipation rate is in general not set by viscosity, but rather by the nonlinear energy transfer between scales.

This inertial transfer is associated with the nonlinear advection term of the Navier-Stokes equations, which formally writes for axisymmetric flows $u_r\partial_r g + u_z\partial_z g$, where g can be any of the velocity components. For such flows the nonlinear advection is therefore due to the poloidal velocity components u_r, u_z. The dissipation rates ε_P and ε_T can be therefore estimated as

$$\varepsilon_P = d_P \frac{E_P}{\tau}, \tag{5.12}$$

$$\varepsilon_T = d_T \frac{E_T}{\tau}, \tag{5.13}$$

where d_P and d_T are dimensionless model parameters, and τ is a typical time scale associated with the poloidal motion :

$$\tau \sim L/E_P^{1/2}. \tag{5.14}$$

In this expression L is a length scale, undefined at this stage. We will come back to this point later on. Equations (5.12, 5.13, 5.14) form the simplest possible model for the dissipation terms ε_P and ε_T.

5.4.2 Forcing modelling

According to Eq.(5.11), the simplest model for the forcing is :

$$F_P = \beta_P c_P \nu E_P, \qquad F_T = \beta_T c_T \nu E_T, \tag{5.15}$$

where β_P and β_T are model parameters.

5.4.3 Transfer modelling

In order to model the transfer term $T = \left\langle u_\theta^2 u_r / r \right\rangle$, we first derive an equation for the triple product $u_\theta^2 u_r$. Using the incompressibility condition and ignoring viscous dissipation and forcing, it is possible to derive from the axisymmetric Navier-Stokes equations (5.1-5.5) the following equality (deduction in Appendix E.2) :

$$\partial_t (u_\theta^2 u_r) = -\left[\frac{1}{r}\partial_r\left(r u_r^2 u_\theta^2\right) + \partial_z\left(u_r u_z u_\theta^2\right) + \frac{2u_r^2 u_\theta^2}{r} - \frac{u_\theta^4}{r} + \frac{u_\theta^2}{\rho}\partial_r p\right]. \tag{5.16}$$

Applying the operator $\langle\ \rangle$ to this equation leads to :

$$\partial_t \left\langle u_\theta^2 u_r \right\rangle = -\left\langle \frac{2u_r^2 u_\theta^2}{r} \right\rangle + \left\langle \frac{u_\theta^4}{r} \right\rangle - \left\langle \frac{u_\theta^2}{\rho}\partial_r p \right\rangle. \tag{5.17}$$

Following [57], the pressure term is modelled as :

$$\left\langle \frac{u_\theta^2}{\rho}\partial_r p \right\rangle \sim \frac{1}{\tau}\left\langle u_\theta^2 u_r \right\rangle, \tag{5.18}$$

where the typical correlation time of the triple correlations is τ, defined in Eq.(5.14). Combining Eqs.(5.17) and (5.18) and making the crude assumption that $\langle f(r)\rangle \sim \langle g(r)\rangle \Rightarrow \langle f(r)/r\rangle \sim \langle g(r)/r\rangle$ allows to propose the following rough, statistically homogeneous model for the transfer term :

$$\begin{aligned} \left\langle \frac{u_\theta^2 u_r}{r} \right\rangle &\sim -\tau \left\langle \frac{2u_r^2 u_\theta^2}{r^2} - \frac{u_\theta^4}{r^2} \right\rangle \\ &\sim \tau \left\langle \frac{u_\theta^2}{r^2}\left(u_\theta^2 - 2u_r^2\right) \right\rangle. \end{aligned} \tag{5.19}$$

Estimating r as R in the right-hand side of Eq.(5.19), assuming that $\left\langle u_r^2 \right\rangle \approx \left\langle u_z^2 \right\rangle$, and neglecting all correlations between u_θ^2, u_r^2 and u_z^2, the transfer can therefore be estimated as :

$$\begin{aligned} T &= \zeta\tau \frac{E_T}{R^2}\left(E_T - E_P\right) \\ &= \zeta\tau \frac{E_T^2}{R^2}\left(1 - \gamma^{-1}\right), \end{aligned} \tag{5.20}$$

where ζ is a dimensionless parameter of the model and τ can be estimated as in Eq.(5.14).

Inserting the estimates (5.12, 5.13, 5.15, 5.20) in the sytem (5.8, 5.9) leads to a model remarkably similar to a classical Reynolds-stress model formulated in cylindrical coordinates [89]. More sophisticated approaches might be envisaged if the present estimate does not capture the physics of the system.

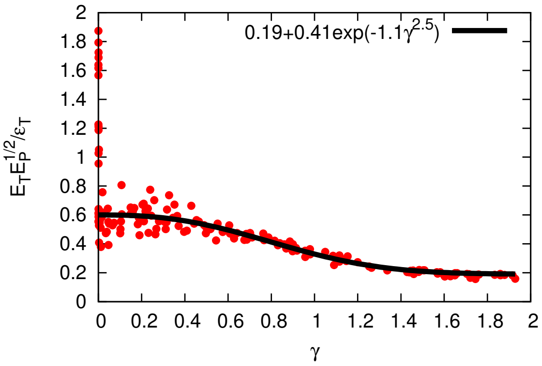

FIGURE 5.5: $E_T E_P^{1/2}/\varepsilon_T$ calculated by DNS, plotted as a function of γ (red dots). The (black) line shows the best data fitting $0.19+0.41\exp(-1.1\gamma^{2.5})$. Following Eq.(5.13), this fitting provides an estimate of $L' = L/d_T$.

5.4.4 Determination of the length scale L

The model derived in the previous subsections requires an expression for the length scale L appearing in the expression of the time scale τ, Eq.(5.14). As a first guess, we assumed that the typical poloidal length scale is proportional to the domain size, and therefore set $L = R$. Under this assumption, the model only displays a weak qualitative agreement with the numerical data.

Our second choice consists in extracting a length scale $L(\gamma)$ from the numerical data using Eq.(5.13) (an equivalently choice would have been to use Eq.(5.12) instead). For this, we plotted for each run the quantity $E_T E_P^{1/2}/\varepsilon_T$ (thereby estimating L/d_T according to Eq.(5.13)) as a function of γ. As shown in Fig.5.5, this quantity is well approximated by the relation :

$$L' \equiv L/d_T \sim E_T E_P^{1/2}/\varepsilon_T \sim 0.19 + 0.41\exp(-1.1\gamma^{2.5}). \tag{5.21}$$

We will thereafter use this expression of $L' \equiv L/d_T(\gamma)$. With this choice, the model can be rewritten as :

$$\frac{\mathrm{d}E_P}{\mathrm{d}t} = \beta_P c_P \nu E_P - d'_P \frac{E_P^{3/2}}{L'(\gamma)} + \zeta' \frac{E_T E_P^{1/2}}{L'(\gamma)} (\gamma - 1)\,, \tag{5.22}$$

$$\frac{\mathrm{d}E_T}{\mathrm{d}t} = \beta_T c_T \nu E_T - \frac{E_T E_P^{1/2}}{L'(\gamma)} - \zeta' \frac{E_T E_P^{1/2}}{L'(\gamma)} (\gamma - 1)\,, \tag{5.23}$$

where $d'_P = d_P/d_T$ and $\zeta' = \zeta/d_T$.

5.4.5 Determination of the model parameters

The model (5.22-5.23) contains four a priori free parameters β_P, β_T, d'_P and ζ', whose value need to be determined. This was done by applying a linear regression to the DNS results, plotting : (i) F_i as a function of E_i ($i \in \{P, T\}$, see Eq.(5.15)) ; (ii) ε_P as a function of $E_P^{3/2}/L'(\gamma)$ (Eqs.(5.12), (5.14) and (5.21)) ; and (iii) T as a function of $E_T E_P^{1/2}(\gamma - 1)/L'(\gamma)$ (Eqs.(5.20), (5.14) and (5.21)).

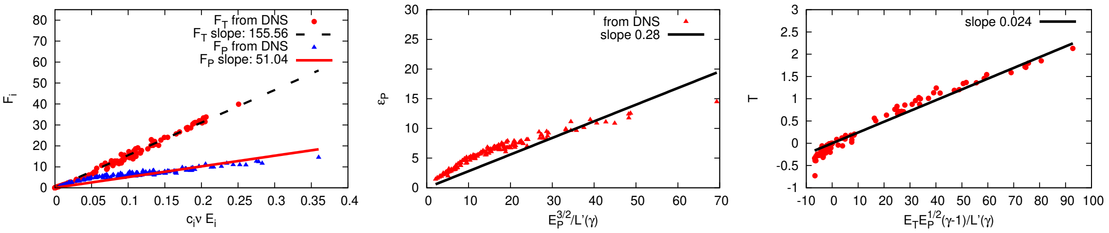

(a) (b) (c)

FIGURE 5.6: Determination of the model parameters (a) β_P, β_T (b) d'_P and (c) ζ' by linear regression of the DNS data.

As shown in Fig.5.6, all the resulting curves display approximately linear dependencies, which confirms our modelling. We found : $\beta_P \approx 51$, $\beta_T \approx 156$, $d'_P \approx 0.28$, and $\zeta' \approx 0.024$. The linear approximation is particularly well satisfied for F_T and T. For F_P and ε_P this approximation is less satisfying, in particular for small values of these quantities.

We compare in Fig.5.7(a) the transfer modellings (5.20, 5.14, 5.21) (with $\zeta' = 0.024$) with the definition of T, Eq.(5.10), for different values of γ. A good agreement is obtained, thereby providing a first, partial validation of the model.

5.4.6 Analytical solution of the model and comparison with the numerical data

Steady states of the system (5.22-5.23) can be easily determined. They are solutions of the following equation for γ :

$$\gamma\left[\gamma^2 + \frac{1-\eta}{\eta}\gamma + \frac{1-d'_P\eta-\zeta'}{\zeta'\eta}\right] = 0, \tag{5.24}$$

where $\eta = (\beta_T c_T)/(\beta_P c_P)$. For any η (or, equivalently, any c_T/c_P), $\gamma = 0$ is a solution. For $\eta \geqslant \eta_c$ such that :

$$\eta_c = \frac{2-\zeta'+2\sqrt{1-\zeta'(d'_P+1)}}{\zeta'+4d'_P}, \tag{5.25}$$

corresponding to a value of $(c_T/c_P)_c \approx 1.13$, another solution exists :

$$\gamma = \frac{\eta-1+\sqrt{(\eta-1)^2+4\eta[1+(d'_P\eta-1)/\zeta']}}{2\eta}. \tag{5.26}$$

The resulting function $\gamma(c_T/c_P)$ is plotted in Fig.5.7(b), and displays an excellent agreement with the numerical results.

The asymptotic value of $\gamma = E_T/E_P$ defined in Eq.(5.26) for large values of c_T/c_P (or ζ) is $\lim_{\zeta\to\infty}\gamma = \left(1+\sqrt{1+4d'_P/\zeta'}\right)/2 \approx 3.95$, which is therefore the maximal value of the ratio between the toroidal and poloidal energy components permitted in this system (see Fig.5.7(b)).

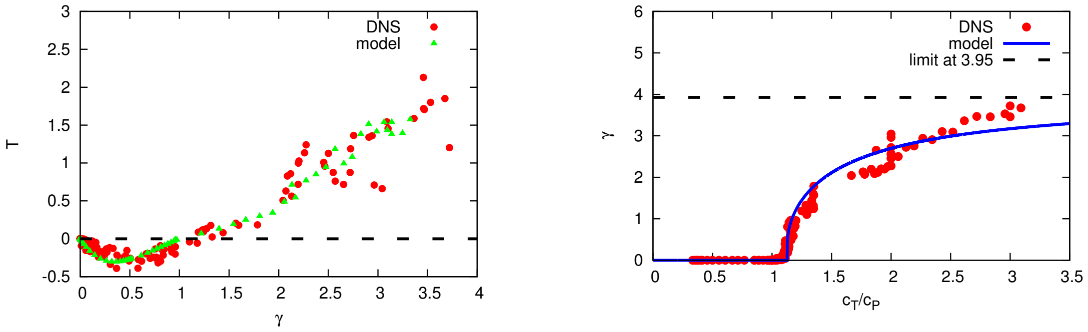

(a)

(b)

Figure 5.7: (a) Steady state values of the transfer T plotted as a function of γ : models (5.20, 5.14) with Eq.(5.21) and $\zeta' = 0.024$, compared with the numerical simulations results. (b) Steady state values of γ plotted as a function of c_T/c_P : analytical solution of the model (5.26) with $\beta_P = 51$, $\beta_T = 156$, $d'_P = 0.28$, and $\zeta' = 0.024$, compared to the numerical simulations results. The horizontal dashed line shows the asymptotic value $\left(1 + \sqrt{1 + 4d'_P/\zeta'}\right)/2$.

5.5 Conclusion

Direct numerical simulations of axisymmetric turbulence forced by a negative viscosity method show the existence of a sharp transition between 2D2C, purely poloidal, or non-swirling turbulence, and the 2D3C poloidal-toroidal, or swirling turbulence. On the level of kinetic energy, the steady states of the system are well captured by a statistical model, reminiscent of a Reynolds-stress closure. This model is derived using assumptions usually valid in the limit of high Reynolds number turbulence. It would be interesting to investigate numerically the dependence of the transition on the Reynolds number.

Finally, a transition from 2D3C (strictly axisymmetric) to 3D3C turbulence could be investigated by using similar tools. This will be done in the next chapter of this thesis.

CHAPITRE 6

Transition from Axisymmetric to General Three-dimensional Turbulence

---

In the previous chapter, we investigated the transition from non-swirling to swirling flow in a purely axisymmetric set-up. This transition was therefore considering the 2D2C to 2D3C transition. The next step towards realistic flows is the transition from 2D3C to 3D3C flows and this is what will be considered in this chapter. To carry out this investigation, we use the pseudo-spectral code which has been modified as described in Section 3.2. The results will be modelled, as in the previous chapter, by a description in terms of volume-averaged kinetic energy components.

6.1 Non-integer dimensions

One of the cornerstones of the theory of isotropic turbulence is its supposed small-scale universality at high Reynolds numbers. In practice only very few flows are close to isotropic. For instance, oceanic and atmospheric flows are three-dimensional but due to the presence of geometrical confinement and body-forces (rotation and/or stratification) the nature of the turbulent motions is at certain scales more two- than three-dimensional.

Compared to academic isotropic flows, realistic flows thus show features which are somewhere between 3D (presence of a direct energy cascade towards small scales) and 2D (presence of well-defined coherent structures) turbulence. Such situations can be investigated numerically by directly integrating the Navier-Stokes equations combined with the appropriate body-forces and boundary conditions. In the present chapter we proceed differently by modifying the Navier-Stokes equations to mimic the anisotropic behavior corresponding to a dynamical dimension which is somewhere between two and three.

The way in which we do this is the following. We consider the Navier-Stokes equations in cylindrical coordinates (a simplified form of Eq.(3.43)) :

$$\begin{aligned}
D_t^{(\alpha)}[u_r] &= f_r + \nu\Delta_r^{(\alpha)} u_r - \partial_r p + \frac{u_\theta^2}{r}, && (6.1)\\
D_t^{(\alpha)}[u_z] &= f_z + \nu\Delta_z^{(\alpha)} u_z - \partial_z p, && (6.2)\\
D_t^{(\alpha)}[u_\theta] &= f_\theta + \nu\Delta_\theta^{(\alpha)} u_\theta - \frac{\alpha}{r}\partial_{\bar{\theta}} p - \frac{u_\theta u_r}{r}, && (6.3)
\end{aligned}$$

where the operator $D^{(\alpha)}[g]$ is defined as

$$D^{(\alpha)}[g] = \partial_t g + u_r \partial_r g + u_z \partial_z g + \alpha \frac{u_\theta}{r}\partial_{\bar{\theta}} g, \tag{6.4}$$

$\Delta_i^{(\alpha)}$ are the three components of the cylindrical vector Laplacian, where, as in $D^{(\alpha)}[g]$, all azimuthal derivatives are multiplied by α or α^2 according to their order.

Incompressibility is ensured by the relation

$$r^{-1}\partial_r(ru_r) + \partial_z u_z + \alpha r^{-1}\partial_{\bar{\theta}}(u_\theta) = 0. \tag{6.5}$$

The above system represents the Navier-Stokes equations for $\alpha = 1$ and axisymmetric flow for $\alpha = 0$. In between these two values the flow is expected to show a transition between the two regimes. It is this transition that we will try to characterize in the following.

6.2 Numerical set-up

As in the simulations presented in Chapter 5, the computational domain has a cylindrical geometry with an aspect ratio of $H/R = 1.7$. The kinematic viscosity is $\nu = 0.01$.

In the present chapter the flow is forced through a linear forcing [90, 91]

$$f_i = \beta u_i. \tag{6.6}$$

This forcing is different from the spectral-band forcing, as it is applied to all scales of the velocity field.

Its implementation is easier which is convenient since in the pseudo-spectral method, based on Chebyshev polynomials it is more difficult to define the wave-number k used before in the spectral code. The forcing is applied in the poloidal plane only, $f_\theta = 0$ and $f_r = f_z$ with a coefficient $\beta = 0.04$ s^{-1}. Computations with azimuthal forcing showed that a very strong dominant, almost uniform azimuthal flow was generated without a very interesting dynamics, and we focus therefore on the case of pure poloidal forcing. Recalling the fact that in this limit the $\alpha = 0$ axisymmetric flow does not generate any toroidal component, our choice will allow to see for which value of α this purely poloidal flow becomes unstable.

The physical time step is set to be $\Delta t = 5 \times 10^{-4}$ s, and the temporal resolution is assessed by monitoring the Courant number as a function of time (see Fig.6.1). The maximal Courant number is chosen in the manner described in Section 3.2.3. Simulations with different α varying from 0 (strictly non-axisymmetric case) to 1 (normal three-dimensional case) are carried out, namely $\alpha = 0$, 0.05, 0.1, 0.15, 0.2, 0.25, 0.3, 0.4, 0.5, 0.6, 0.7, 0.8, 0.9, 1.

With these numerical settings, the attainable large-scale Reynolds number, defined as $\mathrm{Re} \equiv H\sqrt{2E/3}/\nu$, is about 300, which is rather low. In particular the case $\alpha = 0$ is challenging, since due to the inverse cascade that we have evidenced in this case, the energy at the large scales increases importantly and is difficultly dissipated at moderate spatial resolution. Even at the relatively low Reynolds numbers considered, simulations could be carried out for a limited time only and the modified Laplacian $\Delta_i^{(\alpha)}$ in expression (6.1) was replaced by the normal Laplacian $\Delta_i^{(1)}$ in the following. The non-integer dimension α therefore affects only the nonlinear and pressure terms in these simulations.

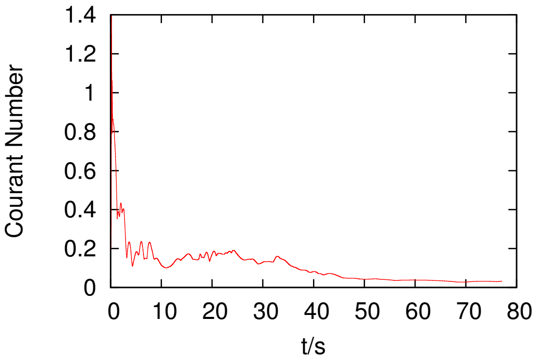

FIGURE 6.1: Temporal evolution of Courant number for $\alpha = 0.3$. After a certain early moment, the Courant number is smaller than 0.5, thereby confirming that the temporal resolution is sufficient.

In order to investigate higher Reynolds number dynamics and to be able to use the modified Laplacian $\Delta_i^{(\alpha)}$, we compared our simulations to results using the spectral vanishing viscosity method [92]. This method, of the Large Eddy Simulation type, allows to attain higher Reynolds numbers and details. Results will be presented in Section 6.6.

6.3 Results of the simulations

6.3.1 Flow visualizations and azimuthal structures

Fig.6.2 shows the instantaneous kinetic energy in cross-sections through the median ($z = 0$) of the cylinder. For values of $\alpha \geqslant 0.15$, we observe a self-organization into azimuthally periodic flower-like structures. We have found in the literature mentions of such structures in three-dimensional cylindrical flows in rotor-stator disc cavities. For instance, in the experimental study by Czarny *et al.* [93] or the numerical work of Craft *et al.* [94] using unsteady k-ε RANS model, the emergence of lobes in flows stirred by one single rotating disc were reported. We do not have discs and we do not know whether these observations are related.

We propose here a phenomenological explanation of the effect. When changing α, the typical gradient length scale in the azimuthal direction changes such that $L_T = \alpha^{-1} L_T^{(1)}$, where $L_T^{(1)}$ is the length scale for $\alpha = 1$, the three-dimensional case, as was explained in Section 3.2.2. We assume that a certain size of structures is generated by the poloidal forcing, typically of the size of the box, since the linear forcing adds energy to all scales. Through nonlinear interactions, these scales destabilize and will also have a finite extend in the azimuthal direction. It can be expected that the azimuthal and poloidal sizes of the structure are of the same order of magnitude. If this is so, a larger number of poloidal structures fits into the box if $L_T \gg R$. The number of structures will thus increase when α diminishes and the number of azimuthal structures will scale as

$$N_s \sim \alpha^{-1}. \tag{6.7}$$

We have evaluated the spatial frequency of the lobes in the horizontal cross-section by counting the number of flow structures during the steady state (Fig.6.2). It is shown in Fig.6.3 that the general trend of the number of lobes is well reproduced by the function $N_s = 2/\alpha$.

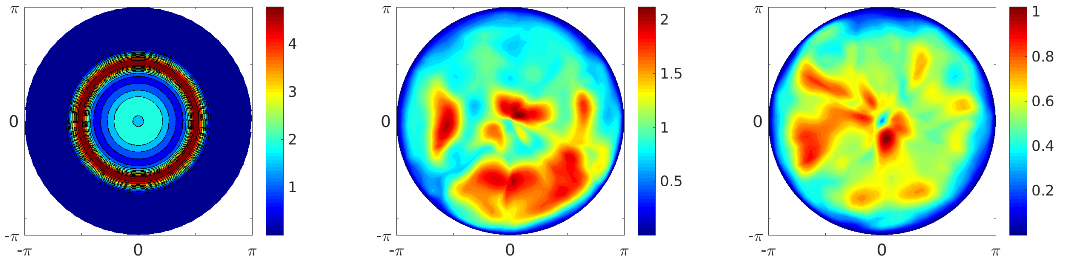

(a) $\alpha = 0.$ (b) $\alpha = 0.05.$ (c) $\alpha = 0.1.$

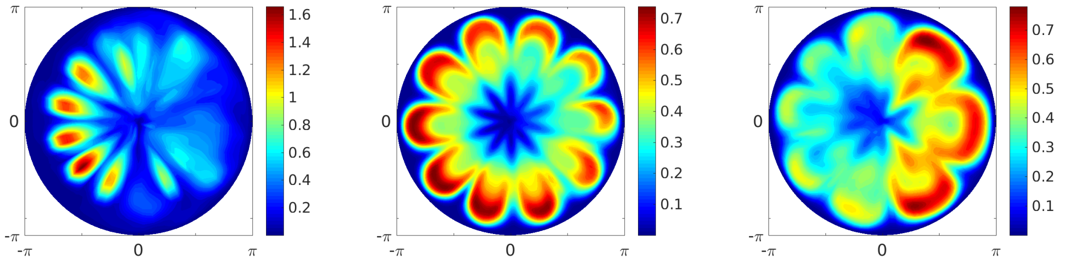

(d) $\alpha = 0.15$: 9-lobe pattern. (e) $\alpha = 0.2$: 10-lobe pattern. (f) $\alpha = 0.25$: 8-lobe pattern.

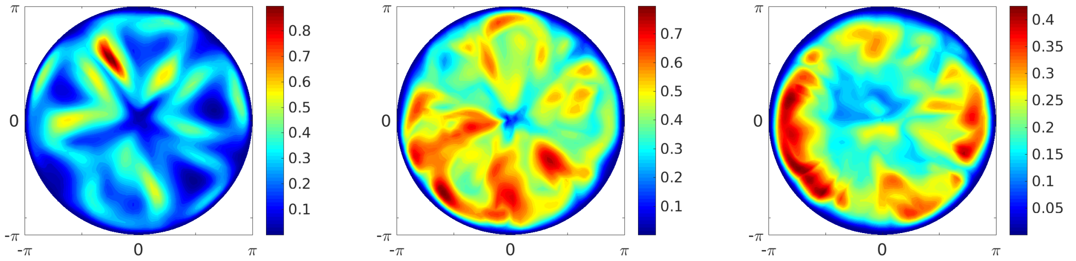

(g) $\alpha = 0.3$: faint 5-lobe pattern. (h) $\alpha = 0.4.$ (i) $\alpha = 0.5.$

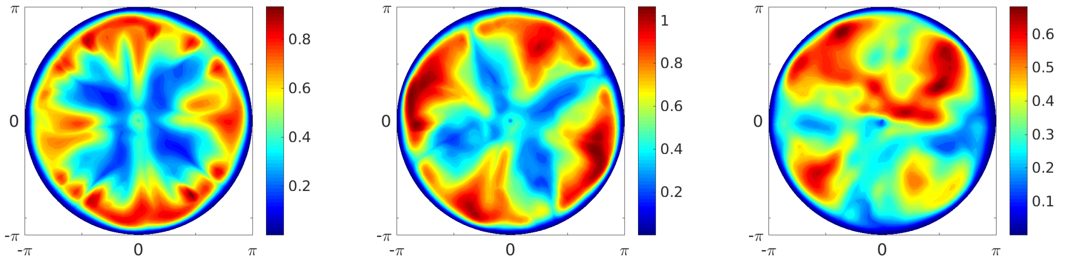

(j) $\alpha = 0.6$: 4-lobe pattern. (k) $\alpha = 0.7$: 4-lobe pattern. (l) $\alpha = 0.8.$

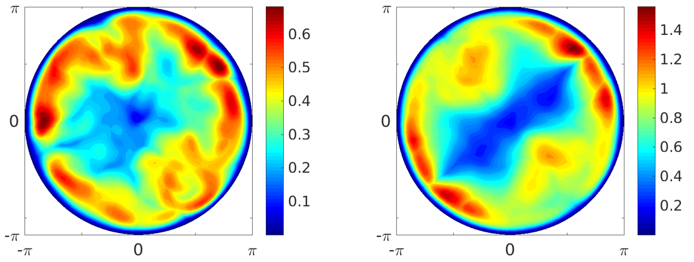

(m) $\alpha = 0.9.$ (n) $\alpha = 1.0$: symmetric pattern.

FIGURE 6.2: Typical instantaneous kinetic energy distribution at $z = 0$ during the statistically steady state of the simulations.

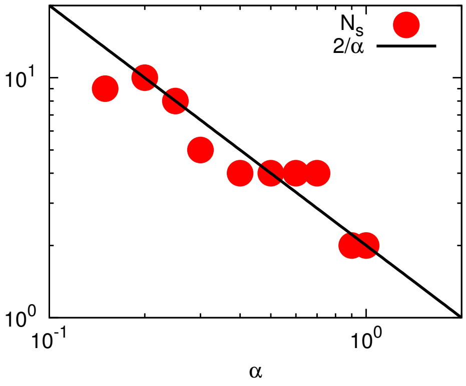

FIGURE 6.3: Number of lobes observed in the kinetic energy visualization in the horizontal median plane of the cylinder, for different values of α. The trend is reproduced by the function $N_s = 2/\alpha$.

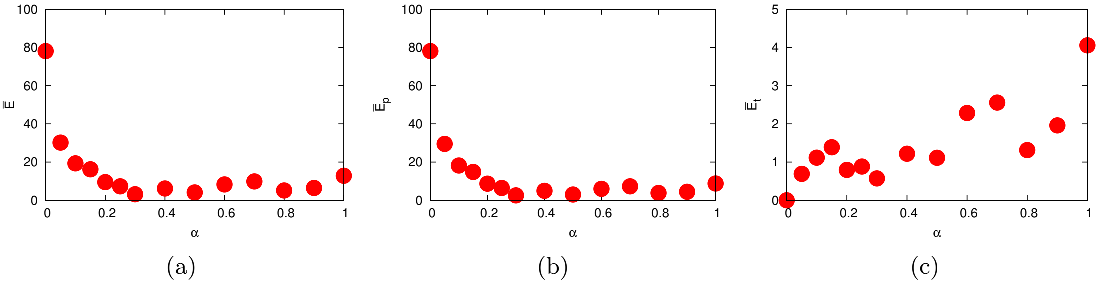

(a)

(b)

(c)

FIGURE 6.4: Dimensionless energy components plotted as a function of α.

6.3.2 Statistical characterization

We show in Fig.6.4 the α-dependence of the dimensionless kinetic energy defined as

$$\overline{E} = \frac{E}{(H\beta)^2}, \tag{6.8}$$

and of dimensionless poloidal energy and azimuthal energy components, defined as

$$\overline{E}_P = \frac{E_P}{(H\beta)^2}, \quad \overline{E}_T = \frac{E_T}{(H\beta)^2}. \tag{6.9}$$

It can be observed that $\overline{E}$ and $\overline{E}_P$ reach their maximum at $\alpha = 0$, then drop abruptly as α increases, and attain an approximately constant value for $\alpha \gtrsim 0.3$. In between 0 and 0.3, the dimensionality parameter α exerts a significant influence on the dynamics.

The situation is inversed for $\overline{E}_T$ which vanishes at $\alpha = 0$ and increases for larger α values. Indeed, when axisymmetry is imposed, it was shown in Chapter 5 that a pure poloidal forcing leads to a two-dimensional two-component dynamics. It is therefore normal and reassuring to observe the same dynamics in the present investigation, by using a different forcing and a different numerical code.

Because the azimuthal dynamics is unforced, the only possible sources of the increase of E_T are the nonlinear transfer of energy T from the radial energy component (see Chapter 5), and the pressure-velocity correlation, which is zero for $\alpha = 0$ and which will

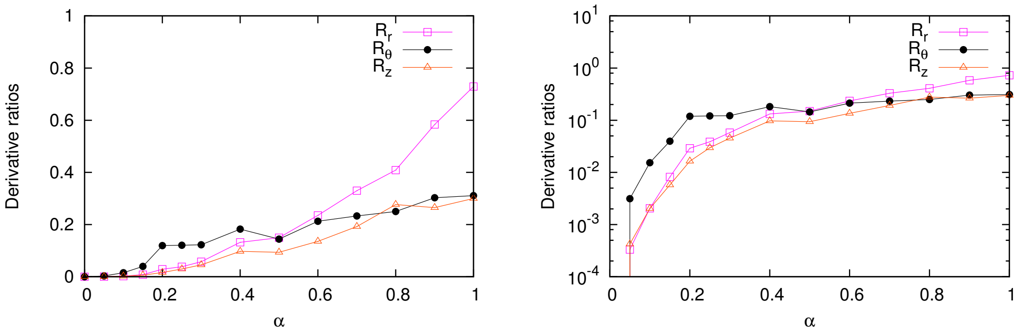

(a) (b)

FIGURE 6.5: Axisymmetry level described by the ratios $\mathcal{R}_r$, $\mathcal{R}_\theta$, $\mathcal{R}_z$. For $\alpha = 0$, the three ratios are 0, as expected due to the axisymmetry constraint. (a) linear-linear scale ; (b) linear-log scale.

be analyzed and modelled in the next section.

Therefore, if the dependence of the kinetic energy on α is an indicator of dimensionality, then the transition from the axisymmetric to the three-dimensional regime appears to be within the interval $\alpha \in [0, 0.3]$, where E_P decreases and E_T increases from 0 to an almost constant value.

We now introduce gradient-based indicators to measure the axisymmetry level. These indicators are

$$\mathcal{R}_r = \frac{\langle \left(\frac{1}{r}\frac{\partial u_r}{\partial \theta}\right)^2 \rangle}{\langle \left(\frac{\partial u_r}{\partial r}\right)^2 + \left(\frac{\partial u_r}{\partial z}\right)^2 \rangle}, \quad \mathcal{R}_z = \frac{\langle \left(\frac{1}{r}\frac{\partial u_z}{\partial \theta}\right)^2 \rangle}{\langle \left(\frac{\partial u_z}{\partial r}\right)^2 + \left(\frac{\partial u_z}{\partial z}\right)^2 \rangle}, \quad \mathcal{R}_\theta = \frac{\langle \left(\frac{1}{r}\frac{\partial u_\theta}{\partial \theta}\right)^2 \rangle}{\langle \left(\frac{\partial u_\theta}{\partial r}\right)^2 + \left(\frac{\partial u_\theta}{\partial z}\right)^2 \rangle}. \quad (6.10)$$

The quantities $\mathcal{R}_r$, $\mathcal{R}_z$ and $\mathcal{R}_\theta$ are therefore defined as the ratio between the strength of the volume-averaged azimuthal derivatives and that of the poloidal derivatives. Their values measure directly the weight of azimuthal variations. Since their definitions involve derivatives, their value is more sensitive to small-scale variations than those of energy-based quantities. $\mathcal{R}_r$, $\mathcal{R}_z$ and $\mathcal{R}_\theta$ are plotted as a function of α in Fig.6.5. One can note that all of them are increasing functions of α and do not reach stable plateaus. This confirms that the axisymmetry constraint is gradually relaxed as α increases. The log-scale plot of Fig.6.5b shows that $\mathcal{R}_i$ $(i \in \{r, \theta, z\})$ increases strongly for $\alpha < 0.2$. Therefore, if the behaviors of $\mathcal{R}_i$ can be considered as indicators of small-scale dimensionality, then the transition from the axisymmetric to the three-dimensional regime takes place within the interval $\alpha \in [0, 0.2]$.

The previous results show that a “transition” from axisymmetric to three-dimensional dynamics takes place between $\alpha = 0$ and $\alpha = 1$. The behavior of the flow is radically different when $\alpha = 0$, by comparison with the other values of α considered. The dependence on α for energy-based anisotropy is most important for $\alpha < 0.3$, while gradient-based quantities are most importantly affected by the value of α when $\alpha < 0.2$.

6.4 Energy based model of the transition

In this section the model proposed in the previous chapter to reproduce the swirling transition is extended to study the transition from 2D2C/2D3C to 3D3C. Exact equations governing the volume-averaged energy budget of the poloidal and toroidal energy can be derived from the Navier-Stokes equations (2.71)

$$\begin{aligned}\frac{\partial E_P}{\partial t} &= T + F_P - \varepsilon_P + \Pi, \\ \frac{\partial E_T}{\partial t} &= -T + F_T - \varepsilon_T - \Pi,\end{aligned} \tag{6.11}$$

where

$$\Pi = \langle \frac{u_\theta}{r\rho}\frac{\partial p}{\partial \theta}\rangle = -\left(\langle \frac{u_r}{\rho}\frac{\partial p}{\partial r}\rangle + \langle \frac{u_z}{\rho}\frac{\partial p}{\partial z}\rangle\right), \tag{6.12}$$

and we recall that F_P and F_T are energy forcing powers, ε_P and ε_T are energy dissipation rates, and T is the energy transfer between azimuthal and radial directions (see Chapter 5 and Appendix E). By a similar process to that presented in Appendix E.1, it can be shown that in the non-axisymmetric case, one has again $T = \langle u_r u_\theta^2/r\rangle$. When the non-complete axisymmetry is introduced, we have that $\partial_\theta \mapsto \alpha\partial_{\bar{\theta}}$, so that

$$\Pi = \alpha\langle \frac{u_\theta}{r\rho}\frac{\partial p}{\partial \bar{\theta}}\rangle. \tag{6.13}$$

This pressure-strain correlation appears as a new term in the energy balance once axisymmetry is broken. In the following we will model this term.

6.4.1 Model for the pressure-strain correlation

The simplest possible model for the pressure-strain correlation is the Rotta model [95]. The pressure-strain correlation acts to restore isotropy in anisotropic flows. Rotta's model uses a linear relation between the anisotropy of the flow and the strength of Π, and is written in Cartesian coordinates as

$$\Pi_{ij} = \frac{c_\Pi}{\mathcal{T}}\left(R_{ij} - \frac{1}{3}R_{mm}\delta_{ij}\right), \tag{6.14}$$

where c_Π is a parameter to be determined, $R_{ij} = \langle u_i u_j\rangle$ is the second-order velocity correlation, δ_{ij} denotes the Kronecker symbol and $\mathcal{T}$ is a characteristic time.

We focus here on the poloidal and toroidal energy components. For fully three-dimensional, volume-averaged flows in cylindrical geometry (α=1), the isotropic state can be expected to be such that $E_\theta = E_r = E_z \implies E_T = E_P/2 = E/3$. By analogy with Eq.(6.14), we can therefore assume that :

$$\Pi(\alpha = 1) = \frac{c_\Pi}{\mathcal{T}}\left(E_T - \frac{1}{3}E\right), \tag{6.15}$$

with the characteristic time being $\mathcal{T} = L/E^{1/2}$.

The question is how this model should be modified for incomplete axisymmetry ($0 < \alpha < 1$). The simplest modification allowing the correct limits (Eq.(6.15) as $\alpha \to 1$ and 0 as $\alpha \to 0$) is

$$\begin{aligned} \Pi(\alpha) &= \alpha\frac{c_\Pi}{\mathcal{T}}\left(E_T - \frac{1}{3}E\right) \\ &= \alpha\frac{c_\Pi}{3\mathcal{T}}\left(2E_T - E_P\right). \end{aligned} \tag{6.16}$$

This model will be shown not to describe the data in the following. The reason for this is not clear from the outset, but it will be shown that replacing (6.16) by

$$\Pi(\alpha) = \alpha\frac{c_\Pi}{\mathcal{T}}\left(E_T - \lambda E_P\right), \tag{6.17}$$

with λ a free constant, the pressure model describes the data more accurately.

The presence of this pressure-strain correlation term changes the energy balance drastically. Indeed, even in the absence of toroidal forcing the pressure-strain correlation allows a transfer from the poloidal to the toroidal component. This can be seen from expression (6.17), where, even for zero toroidal energy, the poloidal energy can be redistributed, as long as $\alpha \neq 0$.

6.4.2 Adaptation of the model to $\alpha \neq 0$

In the model used in the previous chapter, we have modelled the terms T, F_P, F_T, ε_P and ε_T. We recall the equations used :

$$T = \frac{\zeta\tau E_T(E_T - E_P)}{L^2}, \tag{6.18}$$

$$F_i = c_i E_i, \tag{6.19}$$

$$\varepsilon_i = d_i\frac{E_i}{\tau}, \tag{6.20}$$

with $i \in \{T, P\}$. In the axisymmetric case we modelled the typical time scale as

$$\tau(\alpha = 0) \sim L/E_P^{1/2} \tag{6.21}$$

since in this case the poloidal velocity field dominates the dynamics and, in the absence of the transfer term, advects the toroidal velocity as if it were a passive scalar. In the fully three-dimensional case the toroidal velocity plays the same role in the dynamics as the poloidal one, and therefore we model the time scale as

$$\tau(\alpha = 1) \sim \frac{L}{(E_P + E_T)^{1/2}}. \tag{6.22}$$

For any $\alpha \in [0, 1]$, the simplest expression reducing to these forms in the axisymmetric case for $\alpha = 0$ and in a classic three-dimensional form for $\alpha = 1$ is :

$$\tau(\alpha) \sim \frac{L}{(E_P + \alpha E_T)^{1/2}}. \tag{6.23}$$

The forcing F_i does not need any modelling in the present simulations since all modes are forced so that F_i appears in closed form, $F_i = c_i E_i$.

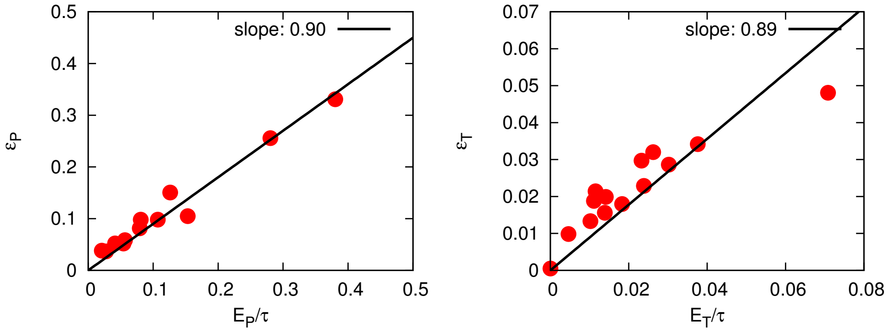

(a) (b)

FIGURE 6.6: Scatter plots of dissipation rates to extract dissipation coefficients d_P and d_T. The linear fittings show that the model (6.20,6.23) for the dissipation rates appears to work well.

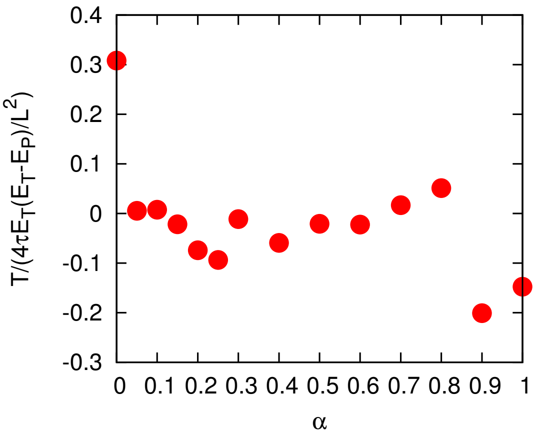

FIGURE 6.7: Assessment of the transfer model (6.18,6.23).

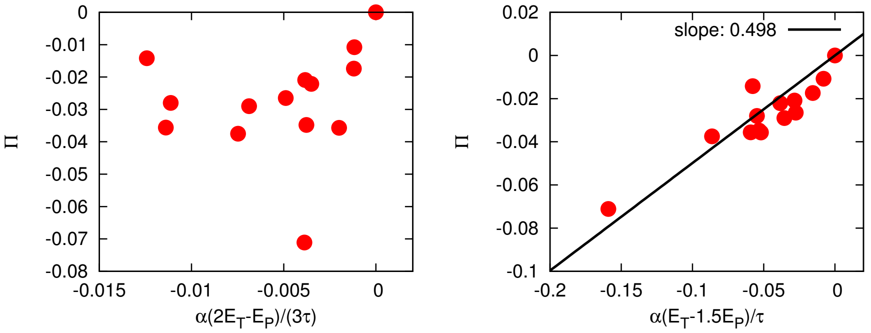

(a) (b)

FIGURE 6.8: Scatter plots for obtention of c_Π in the pressure-strain models from numerical data : (a) Eq.(6.16) and (b) Eq.(6.17).

6.4.3 Numerical assessment of the model

In Fig.6.6 we assess the performance of the dissipation rate model (6.20,6.23). For simplicity, we first choose a constant characteristic scale L independent from α and γ. This choice is shown to work well in Fig.6.6, the linear fittings yielding $\delta_P \approx \delta_T = 0.9$. The model therefore does not need any refinement as was needed for the axisymmetric model, where the integral length scale was found to be a function of γ : it does not seem to be an important function of α in the present simulations.

The modelling of the transfer term (6.18,6.23) is assessed in Fig.6.7. It is observed that the model constant fluctuates around zero. However, the constant of the transfer term is not easy to determine near the axisymmetric limit, because it is zero in the limit $\alpha = 0$ and $c_T = 0$ and since we have only carried out simulations for the case $c_T = 0$ in the present chapter, we cannot evaluate ζ, at least not near the $\alpha = 0$ limit. We will therefore retain the same model as in Chapter 5, and change only the form of the integral time scale.

The pressure-strain model is the main novelty introduced in the present chapter. We first show that the simple extension (6.16) of the Rotta model does not work. Fig.6.8a shows that this form of the model is not satisfied by the data. When we use the expression (6.17) in which an additional model constant λ is introduced, a simultaneous fitting of the parameters c_Π and λ allows to reproduce the data relatively well, giving $c_\Pi = 0.498$ and $\lambda = 1.50$, even though the scatter remains important. This is shown in Fig.6.8b.

To summarize, the model can be written as

$$\begin{aligned}
&T = \frac{\zeta\tau E_T(E_T - E_P)}{L^2},\\
&F_i = c_i E_i,\\
&\varepsilon_i = d_i \frac{E_i}{\tau},\\
&\Pi(\alpha) = \alpha\frac{c_\Pi}{\tau}\left(E_T - \lambda E_P\right),\\
&\tau(\alpha) \sim \frac{L}{(E_P + \alpha E_T)^{1/2}},
\end{aligned} \tag{6.24}$$

where $d_T \approx d_P = 0.90$, $c_\Pi = 0.498$, $\lambda = 1.50$, ζ remains undetermined, and c_T and c_P

will be varied in order to form different ratios between them (as is done in Chapter 5). The model is now complete and we will evaluate its properties in the following section.

6.5 Insights from the simplified model

Now that we have a closed description for the toroidal-poloidal energy dynamics, we focus on the steady state predictions of the model. The toroidal balance, in the absence of toroidal forcing writes

$$0 = -T - \varepsilon_T - \Pi. \tag{6.25}$$

Let us first consider the simplified case where $T = 0$. This is exact in the $\alpha = 0$ limit. We have then directly a balance of energy redistribution by the pressure term Π and the toroidal dissipation ε_T. Using the expressions of the model, this gives

$$\alpha \frac{c_\Pi}{\tau} (E_T - \lambda E_P) = -d_T \frac{E_T}{\tau} \tag{6.26}$$

with an expression for the energy ratio,

$$\gamma \equiv \frac{E_T}{E_P} = \frac{\alpha\lambda}{d_T/c_\Pi + \alpha}. \tag{6.27}$$

According to the model, the energy ratio is therefore a nonlinear function of α. We have plotted this relation in Fig.6.9 and superimposed it to our numerical data. The agreement is satisfactory.

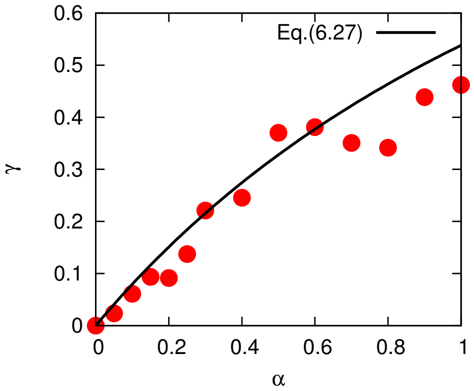

FIGURE 6.9: Energy ratio $\gamma = E_T/E_P$ plotted as a function of α for $c_T = 0$. Dots stand for numerical data, while the line stands for Eq.(6.27).

What we have learned here is that the nonlinear dependence of the energy ratio on α is a direct consequence of the presence of the pressure-strain term, which redistributes the energy over the different energy components.

Another question is how the results from Chapter 5 change when the value of α is varied simultaneously with a change in the forcing anisotropy c_T/c_P. Does a clear bifurcation persist or will the traces of this bifurcation be washed away completely by a gradual introduction of the third dimension and thus of the pressure-strain energy redistribution ? In order to check this, we have integrated the model (6.24), with $\zeta = 0$ at $c_T/c_P = 0$, and $\zeta = 0.024$ (the same value as that used in Chapter 5) for $c_T/c_P \neq 0$. The steady state results are presented in Fig.6.10. We observe that the transition observed in Chapter 5 gradually smoothens out when $\alpha \neq 0$. Particularly, the bifurcation of γ appears to be sensitive to α. For small α close to 0, as is shown in Fig.6.10c, the behavior of $\alpha \neq 0$ is very different from that of $\alpha = 0$. Indeed, this has already been predicted by Eq.(6.17), explaining that once $\alpha \neq 0$, Π will be an important source of energy transfer from the poloidal to the toroidal direction.

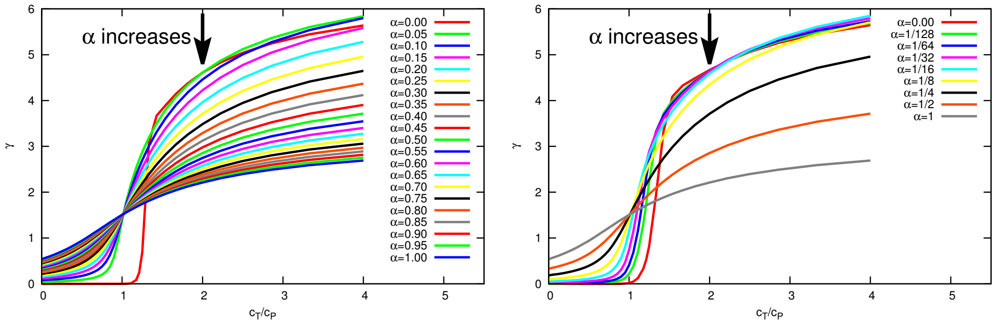

(a) α successively shifted by 0.05.

(b) α successively divided by 2.

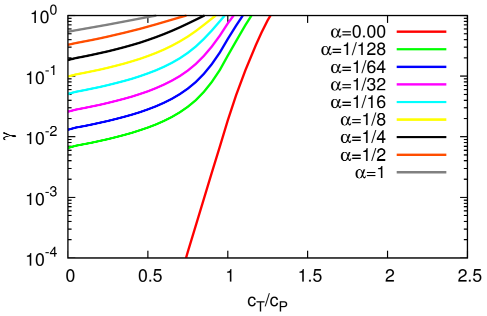

(c) Log-scale view of γ for small α.

FIGURE 6.10: (a-c) Energy ratio $\gamma = E_T/E_P$ plotted as a function of the forcing amplitude ratio c_T/c_P, for different values of α.

6.6 Results at higher Reynolds numbers

The nature of our forcing and the numerical method we used restrict the value of the Reynolds number which can be reached in our simulations. In particular in the axisymmetric, non-swirling limit, where the dynamics are governed by an inverse cascade, the linear forcing tends to feed large scales too efficiently for the viscous dissipation to damp.

Therefore, since we want to assess whether the observed results are not only a low Reynolds number effect, in the present section we carry out Large-Eddy Simulations where the equations are modified using a Spectral Vanishing Viscosity method [92, 67].

The effective viscosity used is $\nu = 10^{-4}$ and is therefore 100 times smaller than that used in our DNS. The Reynolds number is increased by the same factor. The dimensional indicator α is now also present in the Laplacian of the Navier-Stokes equations. The forcing is again purely poloidal and linear. The limit $\alpha = 0$ might be difficultly attainable with such a forcing, but we have succeeded to simulate approximately steady state regimes for the values $\alpha = 0.05$, 0.15, 0.4, 0.6, 0.8, where $\gamma(t)$ attained a constant value.

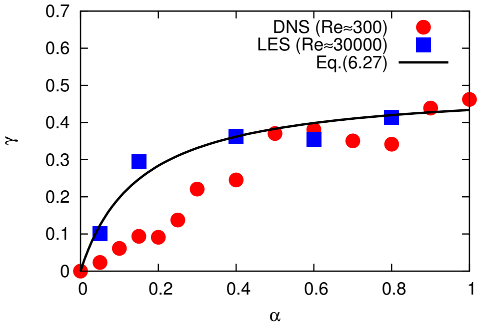

FIGURE 6.11: Energy ratio $\gamma = E_T/E_P$ plotted as a function of α at $c_T = 0$ and $c_P = 0.04$: comparison between DNS (Re $\approx$ 300), LES (Re $\approx$ 30000) and Eq.(6.27) (with $\lambda = 0.5$ and $d_T/c_\Pi = 0.15$).

The results of these LES calculations are compared to the DNS results in Fig.6.11. It is observed that the swirl indicator γ increases more rapidly for small values of α when Re is higher. We have not enough data to confirm this trend, but simulations are still running (July 18th). If other values of α confirm the sharper transition towards three-dimensionality, the values of c_Π and λ in the pressure model and the value of d_T in the dissipation model might need adjustment to correctly reproduce this. For $\lambda = 0.5$ and $d_T/c_\Pi = 0.15$, Fig.6.11 shows that the relation (6.27) fits well the data produced by LES. This shows that (6.27) tends to the asymptotic value $E_T/E_P \approx 0.5$ for large α. This is equivalent to the energy distribution in homogeneous isotropic turbulence at stationary state ($E_r = E_z = E_\theta$). It seems that the different value, $\lambda = 1.5$ observed in the DNS, can be due to the limited Reynolds number.

6.7 Summary

A continuous change of dimension, from axisymmetric to three-dimensions was introduced in the system of equations. The result is a flow which develops an almost periodic azimuthal pattern of the kinetic energy, with a frequency inversely proportional to α.

Both the kinetic energy and velocity-gradient statistics show a clear transition. The energy model from Chapter 5 is adapted to this case by modelling the pressure-strain correlation term. The functional dependence of the swirl indicator γ as a function of the dimensionality α can be understood, using this model, as a balance between pressure distribution, forcing, and dissipation.

CHAPITRE 7

Conclusions and Perspectives

7.1 Conclusions

The objective of the present thesis was to contribute to a better understanding of axisymmetric turbulence. The main questions that were addressed are :

1. Are the theoretical predictions on axisymmetric turbulence, derived for the inviscid and unforced dynamics, valid in a more realistic context ?
2. What are the characteristics of the 2D2C-2D3C (swirling to non-swirling) transition in the framework of axisymmetric turbulence ?
3. When we introduce a non-integer dimension, how different is the case of axisymmetric turbulence from three-dimensional turbulence ? And how can we characterize this transitional cross-over ?

Strictly axisymmetric turbulence does not exist. However the theoretical results [6, 85, 22] were derived for this case and puzzling agreement was observed between the theory and experimental results of three-dimensional turbulence where only the mean-field was axisymmetric [21]. As in the work by Qu *et al.* [7, 9], we therefore used direct numerical simulations to understand the properties of strictly axisymmetric turbulence, and to characterize the common features with two- and three-dimensional turbulence.

The numerical tools we used for this were a fully spectral code [8] and a pseudo-spectral code [66, 67]. Both codes were modified in order to obtain the results presented in the previous chapters. The spectral code was modified in order to change the axial boundary condition from periodic to wall-bounded, by changing the expansion basis in the axial direction. The pseudo-spectral code was modified in order to allow for a non-integer dimension. All numerical details were presented in Chapter 3.

The results associated with the three questions above were presented in Chapters 4-6, respectively and will here be briefly summarized.

1. In the case of axisymmetric flow in a closed cylindrical vessel, in the case of spectral forcing at an intermediate wave-number, large-scale structures are observed and the associated predicted relations between the stream function and the vorticity are observed in the bulk of the flow. These structures are however not stable and do not last for more than several eddy turnover times. The destabilization may be caused by the spectral forcing. The toroidal flow does not show clear structures for the case considered.

   When the flow is set into movement by counter-rotating top and bottom discs, the toroidal component of the flow is more important than for the case of isotropic forcing. Again large-scale structures are observed and the associated functional relationships among $\overline{\psi}$, $\overline{\sigma}$ and $\overline{\xi}$ are observed at a Reynolds number of several thousands.

The presence of coherent structures and functional relationships showing that they are solutions of the Euler equations is shown for the first time in strictly axisymmetric forced turbulence.

2. This importance of the type of forcing on the toroidal dynamics motivates to look at the dependence of the toroidal forcing in a systematic way. For this we simulated more than 150 cases using the fully spectral code, where the poloidal and toroidal energy levels were controlled by the forcing parameters c_P and c_T, resulting in different values of the swirling strength $\gamma = E_T/E_P$. It is observed that in this system the swirling transition is a sharp bifurcation between swirling and non-swirling states, where the non-swirling state is characterized by a poloidal inverse energy cascade. To understand this bifurcation, a statistical model based on large scale dynamics is proposed, with model coefficients fitted from DNS data. The model reproduces well the bifurcation behavior, showing that the energy balance in axisymmetric turbulence can be well approximated by its large-scale dynamics.
3. These interesting observations trigger the question of how close the dynamics are to realistic flows, where the axisymmetry is, at best, only partial. The introduction of a non-integer dimension shows that the purely axisymmetric state is a singular limit and that only little variation in the azimuthal direction is sufficient to break the 2D2C dynamics. The simulations in this chapter are modelled, again, by an ODE model mimicking the dynamics of the toroidal and poloidal energy components. The new term, representing the pressure-strain redistribution of energy, allows to explain the dependence of the swirling level γ on the dimensionality parameter α which we introduced into the system.

These observations logically trigger new questions discussed as perspectives in the following.

7.2 Perspectives

Some open questions and random ideas are summarized here.

1. Given the success in describing the transitions in Chapters 5 and 6, one can ask what other types of flows can be described, on a global level, by simple ODE models such as the ones derived in this thesis.
2. We used a Rotta-type model in Chapter 6 to represent the return to isotropy of turbulence, but a free constant λ, in this model determined the isotropic state to which the flow tends to return. How is this value of λ determined as a function of the dimension, the geometry and the Reynolds number ?
3. Are the observed transitions in the current setting robust enough to be observed at very high Reynolds numbers ? Our simulations were limited by RAM and time constraints. Some evidence using LES was obtained in Chapter 6 that the dimensional cross-over is still observable for higher Reynolds numbers, but this should be checked in a more detailed way.
4. Furthermore, we have not attempted a simultaneous parameter-scan of α and γ (dimensionality and swirling strength). The model has shown that the swirl transition is far less abrupt for partially three-dimensional flows than for the purely axisymmetric case. This can be assessed in simulations to predict whether a swirling transition can possibly be observed in experiments.

5. Can the observed dynamics be compared to turbulence in magnetically confined fusion plasmas ? Indeed, in reactors of the tokamak type, the toroidal magnetic field reduces strongly the variations in the toroidal direction and this system is therefore perhaps the real system which is the closest to axisymmetric turbulence. Does the swirling transition exist in such systems, and if it does, what are the consequences for plasma confinement ?

Appendices

Annexe A

Mathematical Demonstration of Orthogonality and Completeness of the Basis $\mathbf{B}_{qn}$

We consider a cylinder of radius R and height H as fluid domain for an axisymmetric flow. In order to set the no-penetration boundary condition on the two ends of the cylinder, we have chosen the expansion method

$$\begin{aligned} \mathbf{u}(r,z,t) &= \sum_{q,n>0}^{\pm\lambda} C_{qn}(t)\mathbf{B}_{qn}(r,z) \\ &= \sum_{q,n>0}^{\pm\lambda} C_{qn}(t) I_{qn}^{-\frac{1}{2}} \begin{pmatrix} -k_n\gamma_q J_1(\gamma_q r)\cos(k_n z) \\ \lambda_{qn}\gamma_q J_1(\gamma_q r)\sin(k_n z) \\ \gamma_q^2 J_0(\gamma_q r)\sin(k_n z) \end{pmatrix}, \end{aligned} \tag{A.1}$$

where $k_n = n\pi/H$ with $n = 1, 2, 3, ...,$ γ_q is the qth strictly positive root of $J_1(Rx) = 0$, $\lambda_{qn} = \pm\sqrt{\gamma_q^2 + k_n^2}$, and I_{qn} is the normalization constant. The demonstration will use the inner product defined by Eq.(3.3).

A.1 Orthogonality

The demonstration of orthogonality consists in showing that the inner product of $\mathbf{B}_{qn}$ between different q or n or λ_{qn} of opposite signs reduces to zero. The inner product of $\mathbf{B}_{q_1n_1}$ and $\mathbf{B}_{q_2n_2}$ writes

$$\begin{aligned} \langle \mathbf{B}_{q_1n_1}, \mathbf{B}_{q_2n_2} \rangle = & I_{q_1n_1}^{-1/2} I_{q_2n_2}^{-1/2} \frac{1}{V} \int_{z=0}^{H}\int_{\theta=0}^{2\pi}\int_{r=0}^{R} r\mathrm{d}r\mathrm{d}\theta\mathrm{d}z \\ & [k_{n_1}k_{n_2}\gamma_{q_1}\gamma_{q_2} J_1(\gamma_{q_1}r)J_1(\gamma_{q_2}r)\cos(k_{n_1}z)\cos(k_{n_2}z) \\ & +\lambda_{q_1n_1}\lambda_{q_2n_2}\gamma_{q_1}\gamma_{q_2} J_1(\gamma_{q_1}r)J_1(\gamma_{q_2}r)\sin(k_{n_1}z)\sin(k_{n_2}z) \\ & + \gamma_{q_1}^2\gamma_{q_2}^2 J_0(\gamma_{q_1}r)J_0(\gamma_{q_2}r)\sin(k_{n_1}z)\sin(k_{n_2}z)] \,. \end{aligned} \tag{A.2}$$

1. $n_1 \neq n_2$. One can derive :

$$\begin{cases} \displaystyle\int \cos\left(\frac{n_1\pi}{H}z\right)\cos\left(\frac{n_2\pi}{H}z\right)\mathrm{d}z = \frac{H}{2\pi}\left[\frac{1}{n_1-n_2}\sin\left(\frac{(n_1-n_2)\pi}{H}z\right) + \frac{1}{n1+n2}\sin\left(\frac{(n_1+n_2)\pi}{H}z\right)\right] \\ \displaystyle\int \sin\left(\frac{n_1\pi}{H}z\right)\sin\left(\frac{n_2\pi}{H}z\right)\mathrm{d}z = \frac{H}{2\pi}\left[\frac{1}{n_1-n_2}\sin\left(\frac{(n_1-n_2)\pi}{H}z\right) - \frac{1}{n1+n2}\sin\left(\frac{(n_1+n_2)\pi}{H}z\right)\right] \end{cases},$$

$$\Longrightarrow \begin{cases} \displaystyle\int_0^H \cos\left(\frac{n_1\pi}{H}z\right)\cos\left(\frac{n_2\pi}{H}z\right)\mathrm{d}z = 0 \\ \displaystyle\int_0^H \sin\left(\frac{n_1\pi}{H}z\right)\sin\left(\frac{n_2\pi}{H}z\right)\mathrm{d}z = 0. \end{cases},$$

$$\Longrightarrow \langle \mathbf{B}_{q_1n_1}, \mathbf{B}_{q_2n_2}\rangle = 0. \tag{A.3}$$

2. $q_1 \neq q_2$. Recalling $J_1(\gamma_q R) = 0$, one obtains the following result :

$$\begin{cases} \displaystyle\int J_1(\gamma_{q_1}r)J_1(\gamma_{q_2}r)r\mathrm{d}r = \frac{r}{\gamma_{q_1}^2-\gamma_{q_2}^2}\left[\gamma_{q_2}J_1(\gamma_{q_1}r)J_0(\gamma_{q_2}r) - \gamma_{q_1}J_0(\gamma_{q_1}r)J_1(\gamma_{q_2}r)\right] \\ \displaystyle\int J_0(\gamma_{q_1}r)J_0(\gamma_{q_2}r)r\mathrm{d}r = \frac{r}{\gamma_{q_1}^2-\gamma_{q_2}^2}\left[\gamma_{q_1}J_1(\gamma_{q_1}r)J_0(\gamma_{q_2}r) - \gamma_{q_2}J_0(\gamma_{q_1}r)J_1(\gamma_{q_2}r)\right] \end{cases},$$

$$\Longrightarrow \begin{cases} \displaystyle\int_0^R J_1(\gamma_{q_1}r)J_1(\gamma_{q_2}r)r\mathrm{d}r = 0 \\ \displaystyle\int_0^R J_0(\gamma_{q_1}r)J_0(\gamma_{q_2}r)r\mathrm{d}r = 0. \end{cases},$$

$$\Longrightarrow \langle \mathbf{B}_{q_1n_1}, \mathbf{B}_{q_2n_2}\rangle = 0. \tag{A.4}$$

3. $n_1 = n_2 = n$, $q_1 = q_2 = q$, but $\lambda_{q_1n_1} = |\lambda_{qn}|$ and $\lambda_{q_2n_2} = -|\lambda_{qn}|$. In this case the inner product (A.2) becomes

$$\begin{aligned} \langle \mathbf{B}_{q_1n_1}, \mathbf{B}_{q_2n_2}\rangle =& I_{qn}^{-1}\frac{1}{V}\int_{z=0}^{H}\int_{\theta=0}^{2\pi}\int_{r=0}^{R} r\mathrm{d}r\mathrm{d}\theta\mathrm{d}z\,(\\ & k_n^2\gamma_q^2J_1^2(\gamma_q r)\cos^2(k_n z) - \lambda_{qn}^2\gamma_q^2J_1^2(\gamma_q r)\sin^2(k_n z) + \gamma_q^4J_0^2(\gamma_q r)\sin^2(k_n z) \\ &). \end{aligned} \tag{A.5}$$

After some algebra using the following identities :

$$\begin{aligned} &\int_0^R J_1^2(\gamma_q r)r\mathrm{d}r = \frac{R^2}{2}J_0^2(\gamma_q R), \\ &\int_0^R J_0^2(\gamma_q r)r\mathrm{d}r = \frac{R^2}{2}J_0^2(\gamma_q R), \\ &\int_0^H \cos^2\left(\frac{n\pi}{H}z\right)\mathrm{d}z = \frac{H}{2}, \\ &\int_0^H \sin^2\left(\frac{n\pi}{H}z\right)\mathrm{d}z = \frac{H}{2}, \end{aligned} \tag{A.6}$$

one gets

$$\begin{aligned}\langle \mathbf{B}_{q_1n_1}, \mathbf{B}_{q_2n_2}\rangle &= \frac{\gamma_q^2 J_0^2(\gamma_q R)}{2I_{qn}}\left(k_n^2 - \lambda_{qn}^2 + \gamma_q^2\right)\\ &= 0,\end{aligned} \tag{A.7}$$

since $\lambda_{qn}^2 = k_n^2 + \gamma_q^2$.

By now the orthogonality of the basis $\mathbf{B}_{qn}$ has been demonstrated, and the expression of the normalization constant I_{qn} can be obtained by considering the case where $n_1 = n_2 = n$, $q_1 = q_2 = q$ and $\lambda_{q_1n_1} = \lambda_{q_2n_2}$:

$$\begin{aligned}&\langle \mathbf{B}_{q_1n_1}, \mathbf{B}_{q_2n_2}\rangle = \frac{\gamma_q^2 J_0^2(\gamma_q R)}{2I_{qn}}\left(k_n^2 + \lambda_{qn}^2 + \gamma_q^2\right) = 1,\\ \Longrightarrow & I_{qn} = \lambda_{qn}^2\gamma_q^2 J_0^2(\gamma_q R).\end{aligned} \tag{A.8}$$

A.2 Completeness

The basis $\mathbf{B}_{qn}$ being proved orthonormal, the expansion coefficient C_{qn} can be obtained by

$$C_{qn} = \frac{1}{V}\int_V \mathbf{u}\cdot\mathbf{B}_{qn} r\mathrm{d}r\mathrm{d}\theta\mathrm{d}z, \tag{A.9}$$

with V the volume of the domain $V = \pi R^2 H$. Remind that the dynamics of an axisymmetric system can be characterized by the scalar fields (ψ, u_θ), with ψ the stream function within the poloidal plane and u_θ the azimuthal component of the velocity field. In this section, we are going to prove that this basis is indeed complete for an axisymmetric turbulent field $(\psi(r,z), u_\theta(r,z))$ with Dirichlet boundary conditions :

$$\begin{aligned}&\psi(0,z) = \psi(R,z) = 0, \qquad u_\theta(0,z) = u_\theta(R,z) = 0,\\ &\psi(r,0) = \psi(r,H) = 0, \qquad u_\theta(r,0) = u_\theta(r,H) = 0.\end{aligned} \tag{A.10}$$

For simplicity of interpretation, we consider here the scalar field ψ/r instead of ψ directly. We first assume that the two variables r and z of ψ/r can be treated separately :

$$\psi(r,z) = rR_1(r)Z_1(z). \tag{A.11}$$

Knowing that the radial and axial components of $\mathbf{u}$ can be expressed as

$$\begin{aligned}u_r &= -\frac{1}{r}\frac{\partial\psi}{\partial z},\\ u_z &= \frac{1}{r}\frac{\partial\psi}{\partial r},\end{aligned} \tag{A.12}$$

we obtain the expressions of u_r and u_z as a function of R_1 and Z_1 :

$$\begin{cases} u_r(r,z) = -R_1(r)Z_1'(z),\\ u_z(r,z) = \left[\dfrac{1}{r}R_1(r) + R_1'(r)\right]Z_1(z).\end{cases} \tag{A.13}$$

Since u_r has to be zero at $r = 0$, we have $R_1(0) = 0$. Moreover, with the boundary condition $\psi(R,z) = 0$, $R_1(r)$ is also imposed to be zero at $r = R$. This implies that the function $R_1(r)$ can be expanded by using 1st-order Bessel functions of the first kind $J_1(\gamma_p r)$ with $J_1(\gamma_p R) = 0$. These functions form an orthogonal and complete basis for any function defined on $[0, R]$ and are equal to 0 at both ends :

$$\begin{aligned} R_1(r) &= \sum_p^{+\infty} \alpha_p J_1(\gamma_p r), \\ \alpha_p &= \frac{2}{R^2 J_0^2(\gamma_p R)} \int_0^R R_1(r) J_1(\gamma_p r) r \mathrm{d}r. \end{aligned} \tag{A.14}$$

Using such basis functions, ψ, u_r and u_z can be rewritten as

$$\psi(r,z) = r \sum_p^{+\infty} \alpha_p J_1(\gamma_p r) Z_1(z), \tag{A.15}$$

$$u_r(r,z) = -\sum_p^{+\infty} \alpha_p J_1(\gamma_p r) Z_1'(z), \tag{A.16}$$

$$u_z(r,z) = \sum_p^{+\infty} \left[\frac{1}{r} \alpha_p J_1(\gamma_p r) + \alpha_p J_1'(\gamma_p r) \right] Z_1(z) \tag{A.17}$$

$$= \sum_p^{+\infty} \alpha_p \gamma_p J_0(\gamma_p r) Z_1(z). \tag{A.18}$$

Similarly, u_θ can be separated into two parts concerning respectively r and z, and a decomposition of the r part into a series of $J_1(\gamma_p r)$ is adequate :

$$\begin{aligned} u_\theta &= R_2(r) Z_2(z) = \sum_p^{+\infty} \beta_p J_1(\gamma_p r) Z_2(z), \\ \beta_p &= \frac{2}{R^2 J_0^2(\gamma_p R)} \int_0^R R_2(r) J_1(\gamma_p r) r \mathrm{d}r. \end{aligned} \tag{A.19}$$

We can then decompose the velocity field $\mathbf{u}$ by calculating the coefficients C_{qn} :

$$\begin{aligned} C_{qn} &= \frac{1}{V I_{qn}^{1/2}} \int_V \mathbf{u} \cdot \mathbf{B}_{qn} r \mathrm{d}r \mathrm{d}\theta \mathrm{d}z \\ &= \frac{1}{V I_{qn}^{1/2}} \int_V \begin{pmatrix} -\sum_p^{+\infty} \alpha_p J_1(\gamma_p r) Z_1'(z) \\ \sum_p^{+\infty} \beta_p J_1(\gamma_p r) Z_2(z) \\ \sum_p^{+\infty} \alpha_p \gamma_p J_0(\gamma_p r) Z_1(z) \end{pmatrix} \cdot \begin{pmatrix} -k_n \gamma_q J_1(\gamma_q r) \cos(k_n z) \\ \lambda_{qn} \gamma_q J_1(\gamma_q r) \sin(k_n z) \\ \gamma_q^2 J_0(\gamma_q r) \sin(k_n z) \end{pmatrix} r \mathrm{d}r \mathrm{d}\theta \mathrm{d}z \\ &= \frac{1}{V I_{qn}^{1/2}} \int_V \left(\sum_p^{+\infty} \alpha_p J_1(\gamma_p r) Z_1'(z) k_n \gamma_q J_1(\gamma_q r) \cos(k_n z) \right. \\ &+ \sum_p^{+\infty} \beta_p J_1(\gamma_p r) Z_2(z) \lambda_{qn} \gamma_q J_1(\gamma_q r) \sin(k_n z) \\ &+ \left. \sum_p^{+\infty} \alpha_p \gamma_p J_0(\gamma_p r) Z_1(z) \gamma_q^2 J_0(\gamma_q r) \sin(k_n z) \right) r \mathrm{d}r \mathrm{d}\theta \mathrm{d}z. \end{aligned} \tag{A.20}$$

Due to the orthogonality of Bessel functions of the first kind, the integrals $\int_0^R J_1(\gamma_p r)J_1(\gamma_q r) r\mathrm{d}r$ and $\int_0^R J_0(\gamma_p r)J_0(\gamma_q r) r\mathrm{d}r$ are equal to 0 when $p \neq q$. Thus the expression of C_{qn} can be simplified as

$$\begin{aligned} C_{qn} &= \frac{1}{VI_{qn}^{1/2}} \int_V \big(\alpha_q J_1(\gamma_q r)Z_1'(z)k_n\gamma_q J_1(\gamma_q r)\cos(k_n z) \\ &+ \beta_q J_1(\gamma_q r)Z_2(z)\lambda_{qn}\gamma_q J_1(\gamma_q r)\sin(k_n z) \\ &+ \alpha_q\gamma_q J_0(\gamma_q r)Z_1(z)\gamma_q^2 J_0(\gamma_q r)\sin(k_n z)\big)\, r\mathrm{d}r\mathrm{d}\theta\mathrm{d}z \\ &= \frac{R^2 J_0^2(\gamma_q R)\gamma_q\ 2\pi}{2VI_{qn}^{1/2}} \int_0^H \big[\alpha_q k_n Z_1'(z)\cos(k_n z) + \beta_q\lambda_{qn}Z_2(z)\sin(k_n z) + \alpha_q\gamma_q^2 Z_1(z)\sin(k_n z)\big]\,\mathrm{d}z. \end{aligned} \tag{A.21}$$

Using integration by parts, one obtains

$$\int_0^H Z_1'(z)\cos(k_n z)\mathrm{d}z = [Z_1(z)\cos(k_n z)]\Big|_{z=0}^{z=H} + \int_0^H k_n Z_1(z)\sin(k_n z)\mathrm{d}z. \tag{A.22}$$

Recall that Z_1 vanishes at the two ends of the cylinder : $Z_1(0) = Z_1(H) = 0$. This leads to

$$\int_0^H Z_1'(z)\cos(k_n z)\mathrm{d}z = \int_0^H k_n Z_1(z)\sin(k_n z)\mathrm{d}z. \tag{A.23}$$

Then the expression of C_{qn} can be recombined yielding

$$\begin{aligned} C_{qn} &= \frac{J_0^2(\gamma_q R)\gamma_q}{HI_{qn}^{1/2}} \int_0^H \big[\alpha_q k_n^2 Z_1(z)\sin(k_n z) + \beta_q\lambda_{qn}Z_2(z)\sin(k_n z) + \alpha_q\gamma_q^2 Z_1(z)\sin(k_n z)\big]\,\mathrm{d}z \\ &= \frac{J_0^2(\gamma_q R)\gamma_q}{HI_{qn}^{1/2}} \int_0^H \big[\beta_q\lambda_{qn}Z_2(z)\sin(k_n z) + \alpha_q\lambda_{qn}^2 Z_1(z)\sin(k_n z)\big]\,\mathrm{d}z. \end{aligned} \tag{A.24}$$

In order to verify whether the basis is complete, the usual method is to recompose the expanded fields and to compare them with their initial expressions to see if there is a loss of information. We verify first the scalar field ψ. Using the basis $\mathbf{B}_{qn}$, one has

$$u_r(r,z) = -\sum_{q,n>0}^{\pm\lambda} C_{qn}I_{qn}^{-\frac{1}{2}} k_n\gamma_q J_1(\gamma_q r)\cos(k_n z), \tag{A.25}$$

$$\begin{aligned} \psi(r,z) &= \int -r u_r(r,z)\mathrm{d}z \\ &= \int r \sum_{n>0,q}^{\pm\lambda} C_{qn}I_{qn}^{-\frac{1}{2}} k_n\gamma_q J_1(\gamma_q r)\cos(k_n z)\mathrm{d}z \\ &= r \sum_{n>0,q}^{\pm\lambda} C_{qn}I_{qn}^{-\frac{1}{2}} \gamma_q J_1(\gamma_q r)\sin(k_n z). \end{aligned} \tag{A.26}$$

We then substitute (A.24) into (A.26) to get

$$\begin{aligned}
\psi(r,z) &= r\sum_{n>0,q}^{\pm\lambda} C_{qn} I_{qn}^{-\frac{1}{2}}\gamma_q J_1(\gamma_q r)\sin(k_n z)\mathrm{d}z \\
&= r\sum_{n>0,q}^{\pm\lambda}\frac{J_0^2(\gamma_q R)\gamma_q^2}{HI_{qn}}\int_0^H\left[\beta_q\lambda_{qn}Z_2(z')\sin(k_nz')+\alpha_q\lambda_{qn}^2Z_1(z')\sin(k_nz')\right]\mathrm{d}z' J_1(\gamma_q r)\sin(k_n z) \\
&= r\sum_{n>0,q}^{+\lambda}\frac{J_0^2(\gamma_q R)\gamma_q^2}{HI_{qn}}\int_0^H\left[\beta_q\lambda_{qn}Z_2(z')\sin(k_nz')+\alpha_q\lambda_{qn}^2Z_1(z')\sin(k_nz')\right]\mathrm{d}z' J_1(\gamma_q r)\sin(k_n z) \\
&+ r\sum_{n>0,q}^{-\lambda}\frac{J_0^2(\gamma_q R)\gamma_q^2}{HI_{qn}}\int_0^H\left[\beta_q\lambda_{qn}Z_2(z')\sin(k_nz')+\alpha_q\lambda_{qn}^2Z_1(z')\sin(k_nz')\right]\mathrm{d}z' J_1(\gamma_q r)\sin(k_n z) \\
&= 2r\sum_{n>0,q}\frac{J_0^2(\gamma_q R)\gamma_q^2}{HI_{qn}}\left[\int_0^H\alpha_q\lambda_{qn}^2Z_1(z')\sin(k_nz')\mathrm{d}z'\right]J_1(\gamma_q r)\sin(k_n z) \\
&= r\sum_q\alpha_q J_1(\gamma_q r)\left[\sum_{n>0}\frac{2}{H}\int_0^H Z_1(z')\sin(k_nz')\mathrm{d}z'\sin(k_nz)\right].
\end{aligned} \tag{A.27}$$

By comparing with (A.15), we now have to prove

$$\sum_{n>0}\frac{2}{H}\int_0^H Z_1(z')\sin(k_nz')\mathrm{d}z'\sin(k_nz) = Z_1(z). \tag{A.28}$$

In fact, since Z_1 equals 0 at $z=0$ and H, we can extend it from the interval $[0,H]$ to $[-H,H]$ to form an odd function. Then the extended Z_1 can be decomposed into a sum of Fourier series over $[-H,H]$ with a period of $2H$:

$$Z_1(z) = \sum_{n=1}^{+\infty}\left(a_n\cos(\frac{2n\pi z}{2H})+b_n\sin(\frac{2n\pi z}{2H})\right)+\frac{a_0}{2}, \tag{A.29}$$

$$a_n = \frac{2}{2H}\int_{-H}^H Z_1(z)\cos(\frac{2n\pi z}{2H})\mathrm{d}z, \quad n=0,1,2\ldots \tag{A.30}$$

$$b_n = \frac{2}{2H}\int_{-H}^H Z_1(z)\sin(\frac{2n\pi z}{2H})\mathrm{d}z, \quad n=1,2\ldots \tag{A.31}$$

As Z_1 is now an odd function, we have $a_n=0$, and Z_1 depends only on sine functions :

$$\begin{aligned}
Z_1(z) &= \sum_{n=1}^{+\infty} b_n\sin(\frac{2n\pi z}{2H}) \\
&= \sum_{n=1}^{+\infty} b_n\sin(\frac{n\pi z}{H}),
\end{aligned} \tag{A.32}$$

$$\begin{aligned}
b_n &= \frac{2}{2H}\int_{-H}^H Z_1(z)\sin(\frac{2n\pi z}{2H})\mathrm{d}z \\
&= \frac{1}{H}\int_{-H}^H Z_1(z)\sin(\frac{n\pi z}{H})\mathrm{d}z \\
&= \frac{2}{H}\int_0^H Z_1(z)\sin(\frac{n\pi z}{H})\mathrm{d}z, \quad n=1,2\ldots
\end{aligned} \tag{A.33}$$

which leads to

$$Z_1(z) = \sum_{n=1}^{+\infty} \frac{2}{H} \int_0^H Z_1(z') \sin(\frac{n\pi z'}{H}) \mathrm{d}z' \sin(\frac{n\pi z}{H}). \tag{A.34}$$

Then (A.28) is proved, meaning that the decomposition and recomposition via the basis $\mathbf{B}_{qn}$ keeps all information of the scalar field ψ. It should be noticed that both $+\lambda$ and $-\lambda$ modes are considered in the demonstration, explaining their compulsory coexistence in forming the basis. By a similar interpretation, it is not difficult to demonstrate that the scalar field u_θ suffers no information loss through the expansion using $\mathbf{B}_{qn}$. One remark is that the k_n in the basis is defined as $n\pi/H$, which is in fact $2n\pi/(2H)$ and is indeed the wave-number in the z direction for the extended odd domain. This also means that by using a spectral method using this basis, we are actually simulating the evolution of the whole odd ψ field defined over $[-H, H]$. After the advancement of each time step, what we obtain is still an odd field with boundary conditions $\psi(r, 0) = \psi(r, H) = \psi(r, -H) = 0$, which is a consequence imposed by the properties of sine functions, and which is desirable in our case.

In conclusion, the basis $\mathbf{B}_{qn}$ is complete for incompressible axisymmetric velocity fields with boundary conditions :

$$\begin{aligned} u_\theta(0, z) &= 0, \quad u_\theta(R, z) = 0, \\ u_\theta(r, 0) &= 0, \quad u_\theta(r, H) = 0, \\ \psi(0, z) &= 0, \quad \psi(R, z) = 0, \\ \psi(r, 0) &= 0, \quad \psi(r, H) = 0. \end{aligned}$$

Annexe B

Modal Expression of Statistical Quantities in the FSM

In this appendix we give the expressions of the principal integral quantities, as a function of the expansion coefficients C_{qn} used in our fully spectral code. These quantities are the kinetic energy E, the first two non-zero moments of the angular momentum I_1 and I_2, the circulation H_0 and the helicity H_1. By substituting the expansion of $\mathbf{u}$ Eq.(3.16b) and $\boldsymbol{\omega}$ Eq.(3.16c) in the definition of the quantities of interest, one can derive their analytical expressions as a function of C_{qn} :

The total kinetic energy

$$\begin{aligned}
E =&\frac{1}{V}\int_V \frac{1}{2}\mathbf{u}^2 \mathrm{d}V \\
=&\frac{1}{2V}\int_{z=0}^{H}\int_{\theta=0}^{2\pi}\int_{r=0}^{R}\sum_{q_1n_1}^{\pm\lambda}\sum_{q_2n_2}^{\pm\lambda} C_{q_1n_1}C_{q_2n_2}I_{q_1n_1}^{-\frac{1}{2}}I_{q_2n_2}^{-\frac{1}{2}}\mathbf{B}_{q_1n_1}\cdot\mathbf{B}_{q_2n_2} r\mathrm{d}r\mathrm{d}\theta\mathrm{d}z \\
=&\frac{1}{2V}\int_{z=0}^{H}\int_{\theta=0}^{2\pi}\int_{r=0}^{R}\sum_{qn} I_{qn}^{-1}\left(C_{qn}^{+\lambda}\mathbf{B}_{qn}^{+\lambda}+C_{qn}^{-\lambda}\mathbf{B}_{qn}^{-\lambda}\right)\cdot\left(C_{qn}^{+\lambda}\mathbf{B}_{qn}^{+\lambda}+C_{qn}^{-\lambda}\mathbf{B}_{qn}^{-\lambda}\right) r\mathrm{d}r\mathrm{d}\theta\mathrm{d}z \\
=&\frac{1}{2V}\int_{z=0}^{H}\int_{\theta=0}^{2\pi}\int_{r=0}^{R}\sum_{qn}^{+\lambda} C_{qn}^2 I_{qn}^{-1}\mathbf{B}_{qn}\cdot\mathbf{B}_{qn} r\mathrm{d}r\mathrm{d}\theta\mathrm{d}z + \frac{1}{2V}\int_{z=0}^{H}\int_{\theta=0}^{2\pi}\int_{r=0}^{R}\sum_{qn}^{-\lambda} C_{qn}^2 I_{qn}^{-1}\mathbf{B}_{qn}\cdot\mathbf{B}_{qn} r\mathrm{d}r\mathrm{d}\theta\mathrm{d}z \\
+&\frac{1}{V}\int_{z=0}^{H}\int_{\theta=0}^{2\pi}\int_{r=0}^{R}\sum_{qn} C_{qn}^{+\lambda}C_{qn}^{-\lambda}I_{qn}^{-1}\mathbf{B}_{qn}^{+\lambda}\cdot\mathbf{B}_{qn}^{-\lambda} r\mathrm{d}r\mathrm{d}\theta\mathrm{d}z \\
=&\frac{1}{2}\sum_{qn}^{\pm\lambda} C_{qn}^2 \frac{1}{V}\int_{z=0}^{H}\int_{\theta=0}^{2\pi}\int_{r=0}^{R} I_{qn}^{-1}\mathbf{B}_{qn}\cdot\mathbf{B}_{qn} r\mathrm{d}r\mathrm{d}\theta\mathrm{d}z \\
+&\sum_{qn} C_{qn}^{+\lambda}C_{qn}^{-\lambda}I_{qn}^{-1}\frac{1}{V}\int_{z=0}^{H}\int_{\theta=0}^{2\pi}\int_{r=0}^{R}\mathbf{B}_{qn}^{+\lambda}\cdot\mathbf{B}_{qn}^{-\lambda} r\mathrm{d}r\mathrm{d}\theta\mathrm{d}z \\
=&\frac{1}{2}\sum_{qn}^{\pm\lambda} C_{qn}^2,
\end{aligned} \tag{B.1}$$

The angular momentum

$$
\begin{aligned}
I_1 =& \frac{1}{V}\int_V \sigma \mathrm{d}V = \frac{1}{V}\int_{z=0}^{H}\int_{\theta=0}^{2\pi}\int_{r=0}^{R} u_\theta r^2 \mathrm{d}r\mathrm{d}\theta\mathrm{d}z \\
=& \frac{1}{V}\int_{z=0}^{H}\int_{\theta=0}^{2\pi}\int_{r=0}^{R}\sum_{qn}^{\pm\lambda} C_{qn} I_{qn}^{-\frac{1}{2}}\lambda_{qn}\gamma_q J_1(\gamma_q r)\sin(k_n z) r^2 \mathrm{d}r\mathrm{d}\theta\mathrm{d}z \\
=& \frac{2\pi}{\pi R^2 H}\sum_{q,\text{odd } n}^{\pm\lambda} C_{qn} I_{qn}^{-\frac{1}{2}}\lambda_{qn}\gamma_q \int_{r=0}^{R} r^2 J_1(\gamma_q r)\mathrm{d}r \int_{z=0}^{H}\sin(k_n z)\mathrm{d}z \\
=& \frac{2}{R^2 H}\sum_{q,\text{odd } n}^{\pm\lambda} C_{qn} I_{qn}^{-\frac{1}{2}}\lambda_{qn}\gamma_q \left[-\frac{R^2}{\gamma_q}J_0(\gamma_q R)\right]\frac{2H}{n\pi} \\
=& \frac{4}{\pi}\sum_{q,\text{odd } n}^{\pm\lambda} -\frac{C_{qn}\lambda_{qn}J_0(\gamma_q R)}{n\gamma_q|\lambda_{qn}J_0(\gamma_q R)|} \\
=& \frac{4}{\pi}\sum_{q,\text{odd } n}\frac{(C_{qn}^{-\lambda}-C_{qn}^{+\lambda})J_0(\gamma_q R)}{n\gamma_q|J_0(\gamma_q R)|},
\end{aligned}
\tag{B.2}
$$

The variance of the angular momentum

$$
\begin{aligned}
I_2 =& \frac{1}{V}\int_V \sigma^2 \mathrm{d}V = \frac{1}{V}\int_{z=0}^{H}\int_{\theta=0}^{2\pi}\int_{r=0}^{R} u_\theta^2 r^3 \mathrm{d}r\mathrm{d}\theta\mathrm{d}z \\
=& \frac{2\pi}{V}\int_{z=0}^{H}\int_{r=0}^{R}\sum_{q_1 n_1}^{\pm\lambda}\sum_{q_2 n_2}^{\pm\lambda} C_{q_1 n_1}C_{q_2 n_2} I_{q_1 n_1}^{-\frac{1}{2}} I_{q_2 n_2}^{-\frac{1}{2}}\lambda_{q_1 n_1}\lambda_{q_2 n_2}\gamma_{q_1}\gamma_{q_2} J_1(\gamma_{q_1} r)J_1(\gamma_{q_2} r)\sin(k_{n_1} z)\sin(k_{n_2} z) r^3 \mathrm{d}r\mathrm{d}z \\
=& \frac{2\pi}{V}\sum_{q_1=q_2=q,n}\left(C_{qn}^{+\lambda}-C_{qn}^{-\lambda}\right)\left(C_{qn}^{+\lambda}-C_{qn}^{-\lambda}\right)\lambda_{qn}^2 I_{qn}^{-1}\gamma_q^2\int_{z=0}^{H}\int_{r=0}^{R} J_1^2(\gamma_q r)\sin^2(k_n z) r^3 \mathrm{d}r\mathrm{d}z \\
&+ \frac{2\pi}{V}\sum_{q_1\neq q_2,n}\left(C_{q_1 n}^{+\lambda}-C_{q_1 n}^{-\lambda}\right)\left(C_{q_2 n}^{+\lambda}-C_{q_2 n}^{-\lambda}\right)|\lambda_{q_1 n}\lambda_{q_2 n}| I_{q_1 n}^{-\frac{1}{2}} I_{q_2 n}^{-\frac{1}{2}}\gamma_{q_1}\gamma_{q_2} \\
&\int_{z=0}^{H}\int_{r=0}^{R} J_1(\gamma_{q_1} r)J_1(\gamma_{q_2} r)\sin(k_n z)\sin(k_n z) r^3 \mathrm{d}r\mathrm{d}z \\
=& \frac{2\pi}{\pi R^2 H}\sum_{q_1=q_2=q,n}\frac{\left(C_{qn}^{+\lambda}-C_{qn}^{-\lambda}\right)^2\lambda_{qn}^2\gamma_q^2}{I_{qn}}\frac{R^4}{6}J_0^2(\gamma_q R)\frac{H}{2} \\
&+ \frac{2\pi}{\pi R^2 H}\sum_{q_1\neq q_2,n}\frac{\left(C_{q_1 n}^{+\lambda}-C_{q_1 n}^{-\lambda}\right)\left(C_{q_2 n}^{+\lambda}-C_{q_2 n}^{-\lambda}\right)|\lambda_{q_1 n}\lambda_{q_2 n}|\gamma_{q_1}\gamma_{q_2}}{I_{q_1 n}^{\frac{1}{2}} I_{q_2 n}^{\frac{1}{2}}}\frac{4R^2\gamma_{q_1}\gamma_{q_2}}{(\gamma_{q_1}^2-\gamma_{q_2}^2)^2}J_0(\gamma_{q_1} a)J_0(\gamma_{q_2} a)\frac{H}{2} \\
=& \sum_{q_1=q_2=q,n}\frac{R^2\left(C_{qn}^{+\lambda}-C_{qn}^{-\lambda}\right)^2}{6} + \sum_{q_1\neq q_2,n}\frac{4\gamma_{q_1}\gamma_{q_2}\left(C_{q_1 n}^{+\lambda}-C_{q_1 n}^{-\lambda}\right)\left(C_{q_2 n}^{+\lambda}-C_{q_2 n}^{-\lambda}\right)J_0(\gamma_{q_1} a)J_0(\gamma_{q_2} a)}{(\gamma_{q_1}^2-\gamma_{q_2}^2)^2|J_0(\gamma_{q_1} a)J_0(\gamma_{q_2} a)|},
\end{aligned}
\tag{B.3}
$$

The circulation

$$
\begin{aligned}
H_0 =& \frac{1}{V}\int_V \xi \mathrm{d}V = \frac{1}{V}\int_{z=0}^{H}\int_{\theta=0}^{2\pi}\int_{r=0}^{R}\omega_\theta \mathrm{d}r\mathrm{d}\theta\mathrm{d}z \\
=& \frac{2\pi}{V}\sum_{qn}^{\pm\lambda} C_{qn} I_{qn}^{-\frac{1}{2}}\lambda_{qn}^2\gamma_q \int_{z=0}^{H}\int_{r=0}^{R} J_1(\gamma_q r)\sin(k_n z)\mathrm{d}r\mathrm{d}z \\
=& \frac{2\pi}{V}\sum_{q,\mathrm{odd}\ n}^{\pm\lambda} C_{qn} I_{qn}^{-\frac{1}{2}}\lambda_{qn}^2\gamma_q \int_{r=0}^{R} J_1(\gamma_q r)\mathrm{d}r \int_{z=0}^{H}\sin(k_n z)\mathrm{d}z \\
=& \frac{2\pi}{\pi R^2 H}\sum_{q,\mathrm{odd}\ n}^{\pm\lambda} C_{qn} I_{qn}^{-\frac{1}{2}}\lambda_{qn}^2\gamma_q \frac{1-J_0(\gamma_q R)}{\gamma_q}\frac{2H}{n\pi} \\
=& \frac{4}{\pi R^2}\sum_{q,\mathrm{odd}\ n}^{\pm\lambda} \frac{C_{qn}|\lambda_{qn}|(1-J_0(\gamma_q R))}{n\gamma_q|J_0(\gamma_q R)|},
\end{aligned}
\tag{B.4}
$$

The helicity

$$
\begin{aligned}
H_1 =& \frac{1}{V}\int_V \xi\sigma \mathrm{d}V = \frac{1}{V}\int_{z=0}^{H}\int_{\theta=0}^{2\pi}\int_{r=0}^{R}\omega_\theta u_\theta r\mathrm{d}r\mathrm{d}\theta\mathrm{d}z \\
=& \frac{2\pi}{V}\sum_{q_1n_1}^{\pm\lambda}\sum_{q_2n_2}^{\pm\lambda} C_{q_1n_1}C_{q_2n_2} I_{q_1n_1}^{-\frac{1}{2}} I_{q_2n_2}^{-\frac{1}{2}}\lambda_{q_1n_1}^2\lambda_{q_2n_2}\gamma_{q_1}\gamma_{q_2}\int_{r=0}^{R} J_1(\gamma_{q_1}r)J_1(\gamma_{q_2}r)r\mathrm{d}r\int_{z=0}^{H}\sin(k_{n_1}z)\sin(k_{n_2}z)\mathrm{d}z \\
=& \frac{2\pi}{V}\sum_{qn}(C_{qn}^{+\lambda}+C_{qn}^{-\lambda})(C_{qn}^{+\lambda}-C_{qn}^{-\lambda})|\lambda_{qn}^3|I_{qn}^{-1}\gamma_q^2\int_{r=0}^{R} J_1^2(\gamma_q r)r\mathrm{d}r\int_{z=0}^{H}\sin(k_n z)\mathrm{d}z \\
=& \frac{2\pi}{V}\sum_{qn}(C_{qn}^{+\lambda}+C_{qn}^{-\lambda})(C_{qn}^{+\lambda}-C_{qn}^{-\lambda})|\lambda_{qn}^3|I_{qn}^{-1}\gamma_q^2\frac{R^2}{2}J_0^2(\gamma_q R)\frac{H}{2} \\
=& \sum_{qn}\frac{(C_{qn}^{+\lambda}+C_{qn}^{-\lambda})(C_{qn}^{+\lambda}-C_{qn}^{-\lambda})|\lambda_{qn}|}{2} \\
=& \frac{1}{2}\sum_{qn}([C_{qn}^{+\lambda}]^2-[C_{qn}^{-\lambda}]^2)|\lambda_{qn}| \\
=& \frac{1}{2}\sum_{qn}([C_{qn}^{+\lambda}]^2\lambda_{qn}^{+}+[C_{qn}^{-\lambda}]^2\lambda_{qn}^{-}) \\
=& \frac{1}{2}\sum_{qn}^{\pm\lambda} C_{qn}^2\lambda_{qn}.
\end{aligned}
\tag{B.5}
$$

These modal expressions give us the possibility to analyze the contributions of different modes on the principal statistical quantities. For instance, one can observe that only odd n modes contribute to the angular momentum I_0 and to the circulation H_0, and that the helicity H_1 can be separated into two parts consisting respectively of positive and negative λ modes. Such a decomposition was used in [9] to investigate the individual dynamics of different types of helical modes (see also Alexakis [74]). Generic expressions can also be derived for the enstrophy $Z = \frac{1}{V}\int_V \left(\boldsymbol{\omega}^2/2\right)\mathrm{d}V$, the poloidal kinetic energy $E_P = \frac{1}{V}\int_V \left[(u_r^2+u_z^2)/2\right]\mathrm{d}V$, the toroidal kinetic energy $E_T = \frac{1}{V}\int_V \left(u_\theta^2/2\right)\mathrm{d}V$, *etc.*

ANNEXE C

Calculation of ψ in the Axisymmetric PSM

As shown by Eq.(2.41), there exist relationships between ψ, u_r and u_z when the flow is axisymmetric. By knowing u_r and u_z, one can hence derive the ψ field. Due to the no-penetration condition, u_r equals zero on the lateral boundary and can therefore be decomposed by Bessel functions of the first kind. We then choose to obtain ψ from u_r, and for simplicity, we pick $J_1(\gamma_q r)$ to decompose the r direction and $\cos(k_n z)$ in the z direction where γ_q is the qth root of $J_1(Rx) = 0$ and $k_n = (n\pi)/H$ with $n = 0, 1, 2, ...$ u_r is thus decomposed as

$$u_r(r,z) = \sum_{qn} \hat{u}_{r,qn} J_1(\gamma_q r)\cos(k_n z), \tag{C.1}$$

and because $u_r = -(1/r)\partial_z \psi$, one has

$$\psi(r,z) = -\int r u_r(r,z)\mathrm{d}z = -r\sum_{q,n=0} \hat{u}_{r,qn} J_1(\gamma_q r) z - r\sum_{q,n>0} \hat{u}_{r,qn} J_1(\gamma_q r)\frac{\sin(k_n z)}{k_n}. \tag{C.2}$$

Special emphasis should be given to the definition of the domain. Whereas $(\bar{r}, \bar{z}) \in [-1,1] \times [-1,1]$ for Chebyshev polynomials, the decomposition above requires $(r,z) \in [0,R] \times [0,H]$. $\bar{u}_r(\bar{r},\bar{z})$ should first be rescaled to $u_r(r,z)$ in physical space, and $\hat{u}_r$ coefficients are calculated by

$$\hat{u}_{r,qn} = \begin{cases} \dfrac{2}{HR^2 J_0^2(\gamma_q R)} \displaystyle\int_0^H \mathrm{d}z \int_0^R u_r(r,z) J_1(\gamma_q r) r\mathrm{d}r & \text{for } n = 0, \\ \dfrac{4}{HR^2 J_0^2(\gamma_q R)} \displaystyle\int_0^H \cos(k_n z)\mathrm{d}z \int_0^R u_r(r,z) J_1(\gamma_q r) r\mathrm{d}r & \text{for } n = 1, 2, ... \end{cases} \tag{C.3}$$

The Gauss quadrature is again used to numerically calculate the integrals. As the data obtained by this PSM fall on the Gauss-Lobatto collocation points designed for Chebyshev polynomials on both r and z directions, we have used the Gauss-Chebyshev quadrature method based on Gauss-Lobatto collocation points.

This decomposition method will be applied to calculate not only the ψ field for comparison with that obtained by the FSM as a verification (where radial slip is allowed on vertical ends), but also ψ fields with realistic wall boundaries to extract functional relationships between ψ, σ and ξ. Further, this quadrature method is also used to calculate the kinetic energy E, the angular momentum I_1, its variance I_2, the circulation H_0 and the helicity H_1 through their original definitions by direct integration in physical space. In fact, because there may be energy forcing in the form of disc rotation, u_θ can be non-zero on top and bottom of the cylinder. Thus the basis $\mathbf{B}_{qn}$ engaged in the FSM is no longer complete for such cases, and the statistical quantities can no longer be calculated through their expression of modal sums.

Annexe D

Calculation of Integrals in the Non-axisymmetric PSM

D.1 Volume-averaging in the non-axisymmetric PSM

The volum–average of a variable $g(r,\theta,z)$ within a cylindrical domain writes

$$\langle g\rangle = \frac{1}{V}\int_{z=-\frac{H}{2}}^{\frac{H}{2}}\int_{\theta=0}^{2\pi}\int_{r=0}^{R} g(r,\theta,z) r\mathrm{d}r\mathrm{d}\theta\mathrm{d}z, \tag{D.1}$$

with R the radius, H the height and V the volume of the cylinder. Usually, the azimuthal extent ranges from 0 to 2π and the volume equals $\pi R^2 H$. But when the axisymmetry constraint is gradually relaxed, yielding systems with periodicity greater than 2π, the calculation differs. Indeed, in such cases the azimuthal periodicity is $2\pi/\alpha$, with α the control parameter of the axisymmetry level, accounting for a volume of

$$V = \int_{z=-\frac{H}{2}}^{\frac{H}{2}}\int_{\theta=0}^{\frac{2\pi}{\alpha}}\int_{r=0}^{R} r\mathrm{d}r\mathrm{d}\theta\mathrm{d}z = \frac{\pi R^2 H}{\alpha}. \tag{D.2}$$

As explained in Section 3.2.2, however, the azimuthal extent of $\theta \in [0, 2\pi/\alpha]$ should be mapped to $\bar{\theta} \in [0, 2\pi]$, and the integrals are thus calculated within the mapped domain. We recall the introduction of the parameter α :

$$r\theta = L_{\mathrm{t}}\overline{r\theta} = L_{\mathrm{t}}\bar{r}\bar{\theta} = \frac{L_{\mathrm{t}}}{R}R\bar{r}\bar{\theta} = \frac{1}{\alpha}r\bar{\theta}. \tag{D.3}$$

Hence, the infinitesimal increment in the azimuthal direction $r\mathrm{d}\theta$ changes into $(r/\alpha)\mathrm{d}\bar{\theta}$, and consequently, the volume average of g is calculated as

$$\begin{aligned}\langle g\rangle =&\frac{1}{V}\int_{z=-\frac{H}{2}}^{\frac{H}{2}}\int_{\theta=0}^{\frac{2\pi}{\alpha}}\int_{r=0}^{R} g(r,\theta,z) r\mathrm{d}r\mathrm{d}\theta\mathrm{d}z\\ =&\frac{\alpha}{\pi R^2 H}\int_{z=-\frac{H}{2}}^{\frac{H}{2}}\int_{\bar{\theta}=0}^{2\pi}\int_{r=0}^{R} g(r,\bar{\theta},z) r\mathrm{d}r\frac{1}{\alpha}\mathrm{d}\bar{\theta}\mathrm{d}z\\ =&\frac{1}{\pi R^2 H}\int_{z=-\frac{H}{2}}^{\frac{H}{2}}\int_{\bar{\theta}=0}^{2\pi}\int_{r=0}^{R} g(r,\bar{\theta},z) r\mathrm{d}r\mathrm{d}\bar{\theta}\mathrm{d}z,\end{aligned} \tag{D.4}$$

which has almost the same form as that in integer dimensions. Otherwise, using the normalization principle $r = R\bar{r}$ and $z = (H/2)\bar{z}$, the volume average can also be calculated by

$$\begin{aligned}\langle g\rangle =&\frac{1}{\overline{V}}\int_{D} g(\bar{r},\bar{\theta},\bar{z})\mathrm{d}\overline{V}\\ =&\frac{1}{2\pi}\int_{\bar{z}=-1}^{1}\int_{\bar{\theta}=0}^{2\pi}\int_{\bar{r}=0}^{1} g(\bar{r},\bar{\theta},\bar{z})\bar{r}\mathrm{d}\bar{r}\mathrm{d}\bar{\theta}\mathrm{d}\bar{z},\end{aligned} \tag{D.5}$$

with $\overline{V}$ the dimensionless volume and D the mapped domain.

D.2 Dissipation rates in non-axisymmetric PSM simulations

Since the basis $\mathbf{B}_{qn}$ is not rigorously complete for flows forced by rotating discs, the energy dissipation rate ε cannot be calculated through its modal summation form either, and should be analysed in another way. We consider the governing equation of the kinetic energy which writes

$$\frac{1}{\overline{V}}\int_{\mathrm{D}} \bar{\mathbf{u}}\cdot\left(\frac{\partial \bar{\mathbf{u}}}{\partial \bar{t}} + (\bar{\mathbf{u}}\cdot\nabla)\,\bar{\mathbf{u}}\right)\mathrm{d}\overline{V} = \frac{1}{\overline{V}}\int_{\mathrm{D}} \bar{\mathbf{u}}\cdot\left(-\frac{1}{\rho}\nabla\bar{p} + \nu\nabla^2\bar{\mathbf{u}}\right)\mathrm{d}\overline{V}, \tag{D.6}$$

where $\overline{V}$ is the normalized volume of the computational domain. In order to calculate the energy dissipation, one should compute the integral of $\bar{\mathbf{u}}\cdot\nabla^2\bar{\mathbf{u}}$ over the whole domain including wall boundaries. $\bar{\mathbf{u}}\cdot\nabla^2\bar{\mathbf{u}}$ can be rewritten as

$$\begin{aligned}\bar{\mathbf{u}}\cdot\nabla^2\bar{\mathbf{u}} &= \bar{\mathbf{u}}\cdot[\nabla(\nabla\cdot\bar{\mathbf{u}}) - \nabla\times\nabla\times\bar{\mathbf{u}}]\\ &= -\bar{\mathbf{u}}\cdot(\nabla\times\nabla\times\bar{\mathbf{u}})\\ &= \nabla\cdot(\bar{\mathbf{u}}\times(\nabla\times\bar{\mathbf{u}})) - (\nabla\times\bar{\mathbf{u}})^2\,.\end{aligned} \tag{D.7}$$

One can remark that $-(\nabla\times\bar{\mathbf{u}})^2$ is always negative and thus contributes to the dissipation. The volume integrals of $\nabla\cdot(\bar{\mathbf{u}}\times(\nabla\times\bar{\mathbf{u}}))$ can be written as

$$\frac{1}{\overline{V}}\int_{\mathrm{D}}\nabla\cdot(\bar{\mathbf{u}}\times(\nabla\times\bar{\mathbf{u}}))\,\mathrm{d}\overline{V} = \frac{1}{\overline{V}}\oint_{\partial\mathrm{D}}(\bar{\mathbf{u}}\times(\nabla\times\bar{\mathbf{u}}))\cdot\mathbf{n}\mathrm{d}\overline{S}, \tag{D.8}$$

and

$$\bar{\mathbf{u}}\times(\nabla\times\bar{\mathbf{u}}) = \begin{pmatrix} \dfrac{\bar{u}_\theta^2}{\bar{r}} + \bar{u}_\theta\dfrac{\partial\bar{u}_\theta}{\partial\bar{r}} - \dfrac{\bar{u}_\theta}{\bar{r}}\alpha\dfrac{\partial\bar{u}_r}{\partial\bar{\theta}} - \bar{u}_z\dfrac{\partial\bar{u}_r}{\partial\bar{z}} + \bar{u}_z\dfrac{\partial\bar{u}_z}{\partial\bar{r}}\\ \dfrac{\bar{u}_z}{\bar{r}}\alpha\dfrac{\partial\bar{u}_z}{\partial\bar{\theta}} - \bar{u}_z\dfrac{\partial\bar{u}_\theta}{\partial\bar{z}} - \dfrac{\bar{u}_r\bar{u}_\theta}{\bar{r}} - \bar{u}_r\dfrac{\partial\bar{u}_\theta}{\partial\bar{r}} + \dfrac{\bar{u}_r}{\bar{r}}\alpha\dfrac{\partial\bar{u}_r}{\partial\bar{\theta}}\\ \bar{u}_r\dfrac{\partial\bar{u}_r}{\partial\bar{z}} - \bar{u}_r\dfrac{\partial\bar{u}_z}{\partial\bar{r}} - \dfrac{\bar{u}_\theta}{\bar{r}}\alpha\dfrac{\partial\bar{u}_z}{\partial\bar{\theta}} + \bar{u}_\theta\dfrac{\partial\bar{u}_\theta}{\partial\bar{z}} \end{pmatrix}. \tag{D.9}$$

With the no-penetration and no-slip condition, $(\bar{\mathbf{u}}\times(\nabla\times\bar{\mathbf{u}}))\cdot\mathbf{n}$ is zero on wall boundaries except $\bar{u}_\theta\partial_{\bar{z}}\bar{u}_\theta$ on the top and the bottom of the cylinder due to the disc rotation. Thus, one has

$$\frac{1}{\overline{V}}\int_{\mathrm{D}}\nabla\cdot(\bar{\mathbf{u}}\times(\nabla\times\bar{\mathbf{u}}))\,\mathrm{d}\overline{V} = \frac{1}{\overline{V}}\oint_{\mathrm{top}}\bar{u}_\theta\frac{\partial\bar{u}_\theta}{\partial\bar{z}}\mathrm{d}\overline{S} - \frac{1}{\overline{V}}\oint_{\mathrm{bottom}}\bar{u}_\theta\frac{\partial\bar{u}_\theta}{\partial\bar{z}}\mathrm{d}\overline{S}, \tag{D.10}$$

which corresponds to the energy injection. Otherwise, if disc rotation is switched off, this term vanishes and has no contribution.

In conclusion, the expression of the energy dissipation takes the form

$$\bar{\varepsilon}_E = \frac{1}{\overline{V}}\int_{\mathrm{D}}\nu(\nabla\times\bar{\mathbf{u}})^2\mathrm{d}\overline{V}. \tag{D.11}$$

By a similar way, one can deduce that the enstrophy dissipation rate takes the form

$$\bar{\varepsilon}_Z = \frac{1}{\overline{V}}\int_{\mathrm{D}}\nu(\nabla\times\bar{\boldsymbol{\omega}})^2\mathrm{d}\overline{V}. \tag{D.12}$$

The calculation of ε_E and ε_Z introduced in this appendix corresponds more generally to cylindrical flows, and the axisymmetric case is only a special situation. Thus these methods will be used to calculate ε_E and ε_Z in Section 4.2 where axisymmetric flows are simulated by the PSM with mechanical forcing, and the obtained ε_E and ε_Z will be used to test the quality of the mesh resolution. Dissipation rates of different energy components of non-axisymmetric flows in Chapter 6 are also calculated in this way.

Annexe E

Details for Axisymmetric Modelling

E.1 Governing equations for poloidal and toroidal energy components

To obtain the governing equations for the poloidal and toroidal energy components :

$$\begin{aligned} E_P &\equiv \frac{1}{V}\int_V \frac{1}{2}(u_r^2+u_z^2)\mathrm{d}V, \\ E_T &\equiv \frac{1}{V}\int_V \frac{1}{2}(u_\theta^2)\mathrm{d}V, \end{aligned} \tag{E.1}$$

one starts with the forced axisymmetric Navier-Stokes equation for the three velocity components under cylindrical coordinates

$$\frac{\partial u_r}{\partial t}+u_r\frac{\partial u_r}{\partial r}+u_z\frac{\partial u_r}{\partial z}-\frac{u_\theta^2}{r}=-\frac{1}{\rho}\frac{\partial p}{\partial r}+\nu\left(\frac{\partial^2 u_r}{\partial r^2}+\frac{1}{r}\frac{\partial u_r}{\partial r}+\frac{\partial^2 u_r}{\partial z^2}-\frac{u_r}{r^2}\right)+f_r, \tag{E.2a}$$

$$\frac{\partial u_\theta}{\partial t}+u_r\frac{\partial u_\theta}{\partial r}+u_z\frac{\partial u_\theta}{\partial z}+\frac{u_r u_\theta}{r}=\nu\left(\frac{\partial^2 u_\theta}{\partial r^2}+\frac{1}{r}\frac{\partial u_\theta}{\partial r}+\frac{\partial^2 u_\theta}{\partial z^2}-\frac{u_\theta}{r^2}\right)+f_\theta, \tag{E.2b}$$

$$\frac{\partial u_z}{\partial t}+u_r\frac{\partial u_z}{\partial r}+u_z\frac{\partial u_z}{\partial z}=-\frac{1}{\rho}\frac{\partial p}{\partial z}+\nu\left(\frac{\partial^2 u_z}{\partial r^2}+\frac{1}{r}\frac{\partial u_z}{\partial r}+\frac{\partial^2 u_z}{\partial z^2}\right)+f_z, \tag{E.2c}$$

and focuses on the nonlinear terms and pressure terms. To deduce the energy governing equations, one multiplies Eq.(E.2a) by u_r, Eq.(E.2b) by u_θ and Eq.(E.2c) by u_z, and sums up the r and z components to express the poloidal energy component. By applying the volume-integration to the obtained equations, one can write the forced governing equations for E_P and E_T :

$$\begin{aligned} \frac{\partial E_P}{\partial t}+\frac{1}{V}\int_V(\nabla\cdot\mathbf{J}_P-\frac{u_r u_\theta^2}{r})\mathrm{d}V &= -\varepsilon_P+F_P, \\ \frac{\partial E_T}{\partial t}+\frac{1}{V}\int_V(\nabla\cdot\mathbf{J}_T+\frac{u_r u_\theta^2}{r})\mathrm{d}V &= -\varepsilon_T+F_T, \end{aligned} \tag{E.3}$$

where ε_P and ε_T are viscous dissipation rates in corresponding directions, and F_P and F_T are energy forcing powers. We especially focus on the second terms (integral forms of the transfer terms) and the disappearance of the pressure terms in Eq.(E.3).

Transfer terms

After the procedure described above, the poloidal transfer term appears to be

$$\begin{aligned}
&u_r^2\frac{\partial u_r}{\partial r}+u_ru_z\frac{\partial u_r}{\partial z}-\frac{u_ru_\theta^2}{r}+u_ru_z\frac{\partial u_z}{\partial r}+u_z^2\frac{\partial u_z}{\partial z}\\
=&u_r\frac{\partial}{\partial r}\left[\frac{1}{2}(u_r^2+u_z^2)\right]+u_z\frac{\partial}{\partial z}\left[\frac{1}{2}(u_r^2+u_z^2)\right]-\frac{u_ru_\theta^2}{r}\\
=&\frac{\partial}{\partial r}\left[\frac{u_r}{2}(u_r^2+u_z^2)\right]-\frac{1}{2}(u_r^2+u_z^2)\frac{\partial u_r}{\partial r}+\frac{\partial}{\partial z}\left[\frac{u_z}{2}(u_r^2+u_z^2)\right]-\frac{1}{2}(u_r^2+u_z^2)\frac{\partial u_z}{\partial z}\\
=&\left(\frac{\partial}{\partial r}\left[\frac{u_r}{2}(u_r^2+u_z^2)\right]+\frac{\partial}{\partial z}\left[\frac{u_z}{2}(u_r^2+u_z^2)\right]+\frac{1}{r}\left[\frac{u_r}{2}(u_r^2+u_z^2)\right]\right)\\
&-\frac{1}{2}(u_r^2+u_z^2)\left(\frac{\partial u_r}{\partial r}+\frac{\partial u_z}{\partial z}+\frac{u_r}{r}\right)-\frac{u_ru_\theta^2}{r}\\
=&\nabla\cdot\mathbf{J}_P-\frac{1}{2}(u_r^2+u_z^2)\nabla\cdot\mathbf{u}-\frac{u_ru_\theta^2}{r}\\
=&\nabla\cdot\mathbf{J}_P-\frac{u_ru_\theta^2}{r},
\end{aligned}\tag{E.4}$$

with $\mathbf{J}_P=(u_r(u_r^2+u_z^2)/2,\mathcal{J}_\mathcal{A},u_z(u_r^2+u_z^2)/2)$ where $\mathcal{J}_\mathcal{A}$ is an arbitrary variable. By analogy, the toroidal transfer term rewrites as

$$u_ru_\theta\frac{\partial u_\theta}{\partial r}+u_zu_\theta\frac{\partial u_\theta}{\partial z}+\frac{u_ru_\theta^2}{r}=\nabla\cdot\mathbf{J}_T+\frac{u_ru_\theta^2}{r},\tag{E.5}$$

with $\mathbf{J}_T=(u_ru_\theta^2/2,\mathcal{J}_\mathcal{B},u_zu_\theta^2/2)$ where $\mathcal{J}_\mathcal{B}$ is another arbitrary variable. With the no-penetration boundary condition, one can easily show that

$$\begin{aligned}
\frac{1}{V}\int_V\nabla\cdot\mathbf{J}_P\mathrm{d}V=\frac{1}{V}\oint_{\partial D}\mathbf{J}_P\cdot\mathbf{n}\mathrm{d}S=0,\\
\frac{1}{V}\int_V\nabla\cdot\mathbf{J}_T\mathrm{d}V=\frac{1}{V}\oint_{\partial D}\mathbf{J}_T\cdot\mathbf{n}\mathrm{d}S=0.
\end{aligned}\tag{E.6}$$

This means that the remaining $\langle u_ru_\theta^2/r\rangle$ is finally responsible for the energy redistribution between toroidal and poloidal directions :

$$T=\frac{1}{V}\int_V\frac{u_ru_\theta^2}{r}\mathrm{d}V=\langle\frac{u_\theta^2u_r}{r}\rangle.\tag{E.7}$$

A positive T designates an energy transfer from the toroidal direction to the poloidal direction and *vice versa.*

Pressure terms

The toroidal pressure term does not exist in axisymmetric flows. Similarly, through the method of integration by parts, one can deduce that the poloidal pressure term disappears after volume-averaging. We drop the negative sign and the density ρ for simplicity :

$$\begin{aligned}
u_r\frac{\partial p}{\partial r}+u_z\frac{\partial p}{\partial z}&=\frac{\partial(u_rp)}{\partial r}-p\frac{\partial u_r}{\partial r}+\frac{\partial(u_zp)}{\partial z}-p\frac{\partial u_z}{\partial z}-p\frac{u_r}{r}+p\frac{u_r}{r}\\
&=\underbrace{\frac{\partial(u_rp)}{\partial r}}_{(1)}+\underbrace{\frac{\partial(u_zp)}{\partial z}}_{(2)}+\underbrace{\frac{u_rp}{r}}_{(3)}-\underbrace{p\nabla\cdot\mathbf{u}}_{\text{vanishes}}.
\end{aligned}\tag{E.8}$$

- With the boundary conditions $u_z(z=0)=0$ and $u_z(z=H)=0$, the volume-integration of Term (2) is shown to vanish :

$$\frac{1}{V}\int_{z=0}^{H}\int_{\theta=0}^{2\pi}\int_{r=0}^{R}\frac{\partial(u_z p)}{\partial z}r\mathrm{d}r\mathrm{d}\theta\mathrm{d}z = \frac{1}{V}\int_{\theta=0}^{2\pi}\int_{r=0}^{R}(u_z p)\Big|_{z=0}^{z=H} r\mathrm{d}r\mathrm{d}\theta \\ = 0. \tag{E.9}$$

- With the boundary condition $u_r(r=R)=0$, the volume-integration of the combination of terms (1) and (3) also equals 0 :

$$\begin{aligned}\frac{1}{V}\int_{z=0}^{H}\int_{\theta=0}^{2\pi}\int_{r=0}^{R}\left(\frac{\partial(u_r p)}{\partial r}+\frac{u_r p}{r}\right)r\mathrm{d}r\mathrm{d}\theta\mathrm{d}z &= \frac{1}{V}\int_{z=0}^{H}\int_{\theta=0}^{2\pi}\int_{r=0}^{R}\frac{\partial(r u_r p)}{\partial r}\mathrm{d}r\mathrm{d}\theta\mathrm{d}z \\ &= \frac{1}{V}\int_{z=0}^{H}\int_{\theta=0}^{2\pi}(r u_r p)\Big|_{r=0}^{r=R}\mathrm{d}\theta\mathrm{d}z \\ &= 0.\end{aligned} \tag{E.10}$$

This shows that the pressure has no influence on the toroidal-to-poloidal energy redistribution. But if one treats separately the radial and axial energy components, one remarks that the pressure is indeed an active factor to reallocate energy between the r and z directions, since the volume-averaged results $\langle u_r p/r\rangle$ and $\langle u_z p/z\rangle$ are not 0. In Fig.E.1, we show the ratio of radial to axial energy as a function of γ. It is observed that the ratio does not change much over the range $0<\gamma<4$.

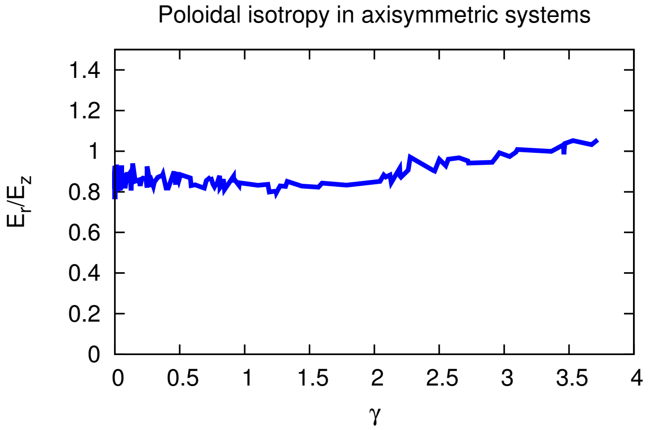

FIGURE E.1: Ratio of E_r/E_z. The energy isotropization between the radial and axial directions can be observed : as γ increased, the ratio is stabilized around 1 though it has a slight rising tendency for large γ.

E.2 Dynamic equation of the toroidal-to-poloidal transfer

In this appendix we derive the model for the toroidal-to-poloidal transfer term $\langle u_r u_\theta^2/r\rangle$. The idea is to derive the transport equation of $u_r u_\theta^2$ from the Navier-Stokes equations. By manipulating the radial and azimuthal components of the Navier-Stokes equations, an equation for $u_r u_\theta^2$ can be derived. Since our object is a pure transfer term, we consider the Euler equations that rule out the dissipation and forcing effects. We start with

$$\frac{\partial u_r}{\partial t}+u_r\frac{\partial u_r}{\partial r}+u_z\frac{\partial u_r}{\partial z}-\frac{u_\theta^2}{r}=-\frac{1}{\rho}\frac{\partial p}{\partial r}, \tag{E.11a}$$

$$\frac{\partial u_\theta}{\partial t}+u_r\frac{\partial u_\theta}{\partial r}+u_z\frac{\partial u_\theta}{\partial z}+\frac{u_r u_\theta}{r}=0. \tag{E.11b}$$

We multiply Eq.(E.11a) by u_θ^2 and Eq.(E.11b) by $2u_r u_\theta$, and obtain

$$u_\theta^2\frac{\partial u_r}{\partial t}+u_\theta^2 u_r\frac{\partial u_r}{\partial r}+u_\theta^2 u_z\frac{\partial u_r}{\partial z}-\frac{u_\theta^4}{r}=-\frac{u_\theta^2}{\rho}\frac{\partial p}{\partial r}, \tag{E.12a}$$

$$2u_r u_\theta\frac{\partial u_\theta}{\partial t}+2u_r^2 u_\theta\frac{\partial u_\theta}{\partial r}+2u_r u_\theta u_z\frac{\partial u_\theta}{\partial z}+\frac{2u_r^2 u_\theta^2}{r}=0. \tag{E.12b}$$

The summation of these two equations gives

$$\frac{\partial(u_r u_\theta^2)}{\partial t}+\underbrace{u_\theta^2 u_r\frac{\partial u_r}{\partial r}}_{(1)}+\underbrace{u_\theta^2 u_z\frac{\partial u_r}{\partial z}}_{(2)}+\underbrace{2u_r^2 u_\theta\frac{\partial u_\theta}{\partial r}}_{(3)}+\underbrace{2u_r u_\theta u_z\frac{\partial u_\theta}{\partial z}}_{(4)}-\frac{u_\theta^4}{r}+\frac{2u_r^2 u_\theta^2}{r}=-\frac{u_\theta^2}{\rho}\frac{\partial p}{\partial r}. \tag{E.13}$$

Further simplifications are :

- for Term (1) :

$$u_\theta^2 u_r\frac{\partial u_r}{\partial r}=\frac{1}{r}\frac{\partial(r u_r^2 u_\theta^2)}{\partial r}-\frac{u_\theta^2 u_r^2}{r}-\underbrace{u_r^2\frac{\partial u_\theta^2}{\partial r}}_{(3)}-u_\theta^2 u_r\frac{\partial u_r}{\partial r}; \tag{E.14}$$

- for Term (2) :

$$u_\theta^2 u_z\frac{\partial u_r}{\partial z}=\frac{\partial(u_r u_\theta^2 u_z)}{\partial z}-\underbrace{u_r u_z\frac{\partial u_\theta^2}{\partial z}}_{(4)}-u_\theta^2 u_r\frac{\partial u_z}{\partial z}. \tag{E.15}$$

Then Eq.(E.13) becomes

$$\frac{\partial(u_r u_\theta^2)}{\partial t}+\frac{1}{r}\frac{\partial(r u_r^2 u_\theta^2)}{\partial r}+\frac{\partial(u_r u_\theta^2 u_z)}{\partial z}-u_\theta^2 u_r\frac{\partial u_r}{\partial r}-u_\theta^2 u_r\frac{\partial u_z}{\partial z}-\frac{u_\theta^4}{r}+\frac{u_r^2 u_\theta^2}{r}=-\frac{u_\theta^2}{\rho}\frac{\partial p}{\partial r}. \tag{E.16}$$

Using the incompressibility condition

$$\begin{aligned}&\frac{\partial u_r}{\partial r}+\frac{u_r}{r}+\frac{\partial u_z}{\partial z}=0,\\ \Longleftrightarrow\ &u_\theta^2 u_r\frac{\partial u_r}{\partial r}+\frac{u_r^2 u_\theta^2}{r}+u_\theta^2 u_r\frac{\partial u_z}{\partial z}=0,\end{aligned} \tag{E.17}$$

Eq.(E.16) can be simplified as

$$\frac{\partial(u_r u_\theta^2)}{\partial t}+\frac{1}{r}\frac{\partial(r u_r^2 u_\theta^2)}{\partial r}+\frac{\partial(u_r u_\theta^2 u_z)}{\partial z}-\frac{u_\theta^4}{r}+\frac{2u_r^2 u_\theta^2}{r}=-\frac{u_\theta^2}{\rho}\frac{\partial p}{\partial r}. \tag{E.18}$$

We then perform the volume-average of Eq.(E.18). With the boundary condition $u_\theta=0$ on all boundaries and given the fact that $u_\theta=0$ on the axis, we find

$$\begin{aligned}\frac{1}{V}\int_V\frac{1}{r}\frac{\partial(r u_r^2 u_\theta^2)}{\partial r}r\mathrm{d}r\mathrm{d}z\mathrm{d}\theta&=\frac{1}{V}\int_V\frac{\partial(r u_r^2 u_\theta^2)}{\partial r}\mathrm{d}r\mathrm{d}z\mathrm{d}\theta\\ &=\frac{1}{V}\int_\theta\int_z(r u_r^2 u_\theta^2)\Big|_{r=0}^{r=R}\mathrm{d}z\mathrm{d}\theta\\ &=0,\end{aligned} \tag{E.19a}$$

$$\begin{aligned}\frac{1}{V}\int_V \frac{\partial(u_r u_\theta^2 u_z)}{\partial z} r\mathrm{d}r\mathrm{d}z\mathrm{d}\theta &= \frac{1}{V}\int_\theta\int_r (u_r u_\theta^2 u_z)\Big|_{z=H}^{z=0} r\mathrm{d}r\mathrm{d}\theta \\ &= 0.\end{aligned} \tag{E.19b}$$

As a result, we have

$$\begin{aligned}&\frac{\partial}{\partial t}\left(\frac{1}{V}\int_V u_r u_\theta^2 \mathrm{d}V\right) = \frac{1}{V}\int_V \frac{u_\theta^4}{r}\mathrm{d}V - \frac{1}{V}\int_V \frac{2u_r^2 u_\theta^2}{r}\mathrm{d}V - \frac{1}{V}\int_V \frac{u_\theta^2}{\rho}\frac{\partial p}{\partial r}\mathrm{d}V, \\ \Longleftrightarrow &\frac{\partial\langle u_r u_\theta^2\rangle}{\partial t} = \langle\frac{u_\theta^4}{r}\rangle - \langle\frac{2u_r^2 u_\theta^2}{r}\rangle - \langle\frac{u_\theta^2}{\rho}\frac{\partial p}{\partial r}\rangle.\end{aligned} \tag{E.20}$$

Bibliographie

[1] Lars Onsager. Statistical hydrodynamics. *Il Nuovo Cimento (1943-1954)*, 6(2) :279–287, 1949. (Cited on pages 1 and 8.)

[2] Jonathan Miller. Statistical mechanics of Euler equations in two dimensions. *Physical Review Letters*, 65(17) :2137, 1990. (Cited on pages 1, 11 and 12.)

[3] Raoul Robert and Joel Sommeria. Statistical equilibrium states for two-dimensional flows. *Journal of Fluid Mechanics*, 229 :291–310, 1991. (Cited on pages 1, 11 and 12.)

[4] Freddy Bouchet and Antoine Venaille. Statistical mechanics of two-dimensional and geophysical flows. *Physics reports*, 515(5) :227–295, 2012. (Cited on page 1.)

[5] Freddy Bouchet and Thierry Dumont. Emergence of jupiter's vortices and jets from random initial conditions. *arXiv preprint cond-mat/0305206*, 2003. (Cited on page 2.)

[6] Nicolas Leprovost, Bérengère. Dubrulle, and Pierre-Henri Chavanis. Dynamics and thermodynamics of axisymmetric flows : Theory. *Physical Review E*, 73(4) :046308, 2006. (Cited on pages 2, 14, 15, 37, 64 and 89.)

[7] Bo Qu, Wouter JT Bos, and Aurore Naso. Direct numerical simulation of axisymmetric turbulence. *Physical Review Fluids*, 2(9) :094608, 2017. (Cited on pages 2, 4, 13, 18, 27, 29, 34, 35, 45, 61, 64, 65 and 89.)

[8] Bo Qu. *Numerical simulation of axisymmetric turbulence.* PhD thesis, Lyon, 2017. (Cited on pages 2, 3, 13, 18, 27, 28, 29, 30, 34, 35, 45, 51, 52, 58, 59, 61 and 89.)

[9] Bo Qu, Aurore Naso, and Wouter JT Bos. Cascades of energy and helicity in axisymmetric turbulence. *Physical Review Fluids*, 3(1) :014607, 2018. (Cited on pages 2, 4, 13, 18, 27, 29, 34, 35, 45, 51, 61, 64, 65, 68, 89 and 105.)

[10] Hudong Chen, Xiaowen Shan, and David Montgomery. Galerkin approximations for dissipative magnetohydrodynamics. *Physical Review A*, 42(10) :6158, 1990. (Cited on pages 2 and 28.)

[11] Éric Séverac, Sébastien Poncet, Éric Serre, and Marie-Pierre Chauve. Large eddy simulation and measurements of turbulent enclosed rotor-stator flows. *Physics of Fluids*, 19(8) :085113, 2007. (Cited on page 3.)

[12] Stephen B. Pope. Turbulent flows. 2011. (Cited on page 4.)

[13] Darryl D. Holm, Jerrold E. Marsden, Tudor Ratiu, and Alan Weinstein. Nonlinear stability of fluid and plasma equilibria. *Physics Reports*, 123(1-2) :1–116, 1985. (Cited on page 7.)

[14] Dieter Biskamp. *Magnetohydrodynamic turbulence.* Cambridge University Press, 2003. (Cited on page 7.)

[15] Gustav Kirchhoff. Lectures on mathematical physics, mechanics. *Teubner, Leipzig*, 1877. (Cited on page 7.)

[16] Glenn Joyce and David Montgomery. Negative temperature states for the two-dimensional guiding-centre plasma. *Journal of Plasma Physics*, 10(01) :107–121, 1973. (Cited on page 8.)

[17] David Montgomery, William H. Matthaeus, W. Troy Stribling, Daniel Martinez, and Sean Oughton. Relaxation in two dimensions and the "sinh-Poisson" equation. *Physics of Fluids A : Fluid Dynamics*, 4(1) :3–6, 1992. (Cited on page 10.)

[18] Pierre-Henri Chavanis. Coarse-grained distributions and superstatistics. *Physica A : Statistical Mechanics and its Applications*, 359 :177–212, 2006. (Cited on page 12.)

[19] Pierre-Henri Chavanis and Joel Sommeria. Classification of self-organized vortices in two-dimensional turbulence : the case of a bounded domain. *Journal of Fluid Mechanics*, 314 :267–297, 1996. (Cited on page 12.)

[20] Florent Ravelet, Louis Marié, Arnaud Chiffaudel, and François Daviaud. Multistability and memory effect in a highly turbulent flow : Experimental evidence for a global bifurcation. *Physical review letters*, 93(16) :164501, 2004. (Cited on pages 13, 17, 53 and 54.)

[21] Romain Monchaux, Florent Ravelet, Bérengère Dubrulle, Arnaud Chiffaudel, and François Daviaud. Properties of steady states in turbulent axisymmetric flows. *Physical review letters*, 96(12) :124502, 2006. (Cited on pages 13, 17, 45, 46, 53, 54, 55, 56, 58 and 89.)

[22] Aurore Naso, Simon Thalabard, Gilles Collette, Pierre-Henri Chavanis, and Bérengère Dubrulle. Statistical mechanics of Beltrami flows in axisymmetric geometry : equilibria and bifurcations. *Journal of Statistical Mechanics : Theory and Experiment*, 2010(06) :P06019, 2010. (Cited on pages 17, 46, 53, 64 and 89.)

[23] Eric Herbert, François Daviaud, Bérengère Dubrulle, Sergey Nazarenko, and Aurore Naso. Dual non-Kolmogorov cascades in a von Kármán flow. *EPL (Europhysics Letters)*, 100(4) :44003, 2012. (Cited on pages 17, 50, 57 and 61.)

[24] Shuojun Li, David Montgomery, and Wesley B Jones. Inverse cascades of angular momentum. *Journal of plasma physics*, 56(3) :615–639, 1996. (Cited on page 18.)

[25] Hua Xia, David Byrne, Gregory Falkovich, and Michael Shats. Upscale energy transfer in thick turbulent fluid layers. *Nature Physics*, 7(4) :321, 2011. (Cited on pages 18 and 20.)

[26] Alexandros Alexakis and Luca Biferale. Cascades and transitions in turbulent flows. *Physics Reports*, 2018. (Cited on pages 18 and 63.)

[27] Annick Pouquet, Duane Rosenberg, Julia E. Stawarz, and Raffaele Marino. Helicity dynamics, inverse, and bidirectional cascades in fluid and magnetohydrodynamic turbulence : a brief review. *Earth and Space Science*, 6(3) :351–369, 2019. (Cited on page 18.)

[28] Antonio Celani, Stefano Musacchio, and Dario Vincenzi. Turbulence in more than two and less than three dimensions. *Physical review letters*, 104(18) :184506, 2010. (Cited on pages 19, 20 and 63.)

[29] Santiago Jose Benavides and Alexandros Alexakis. Critical transitions in thin layer turbulence. *Journal of Fluid Mechanics*, 822 :364–385, 2017. (Cited on pages 19 and 63.)

[30] Joel Sommeria. Experimental study of the two-dimensional inverse energy cascade in a square box. *Journal of fluid mechanics*, 170 :139–168, 1986. (Cited on page 20.)

[31] Jan-Bert Flór and Gertijan Jan F. van Heijst. An experimental study of dipolar vortex structures in a stratified fluid. *Journal of Fluid Mechanics*, 279 :101–133, 1994. (Cited on page 20.)

[32] Michael Shats, David Byrne, and Hua Xia. Turbulence decay rate as a measure of flow dimensionality. *Physical review letters*, 105(26) :264501, 2010. (Cited on page 20.)

[33] Kenneth G. Wilson and Michael E. Fisher. Critical exponents in 3.99 dimensions. *Physical Review Letters*, 28(4) :240, 1972. (Cited on page 21.)

[34] Kenneth G. Wilson and John Kogut. The renormalization group and the ε expansion. *Physics reports*, 12(2) :75–199, 1974. (Cited on page 21.)

[35] Carlos Guido Bollini and Juan José Giambiagi. Dimensional renormalization : The number of dimensions as a regularizing parameter. *Il Nuovo Cimento B (1971-1996)*, 12(1) :20–26, 1972. (Cited on page 21.)

[36] Gerard t Hooft and Martinus J.G. Veltman. Regularization and renormalization of gauge fields. *Nuclear Physics B*, 44(1) :189–213, 1972. (Cited on page 21.)

[37] Kenneth G. Wilson. Quantum field-theory models in less than 4 dimensions. *Physical Review D*, 7(10) :2911, 1973. (Cited on page 21.)

[38] C Palmer and Paul N. Stavrinou. Equations of motion in a non-integer-dimensional space. *Journal of Physics A : Mathematical and General*, 37(27) :6987, 2004. (Cited on page 21.)

[39] Vasily E. Tarasov. Vector calculus in non-integer dimensional space and its applications to fractal media. *Communications in Nonlinear Science and Numerical Simulation*, 20(2) :360–374, 2015. (Cited on page 21.)

[40] Uriel Frisch, Marcel Lesieur, and Pierre Louis Sulem. Crossover dimensions for fully developed turbulence. *Physical Review Letters*, 37(14) :895, 1976. (Cited on pages 21 and 63.)

[41] Jean-Daniel Fournier and Uriel Frisch. d-dimensional turbulence. *Physical Review A*, 17(2) :747, 1978. (Cited on page 21.)

[42] Uriel Frisch, Anna Pomyalov, Itamar Procaccia, and Samriddhi Sankar Ray. Turbulence in noninteger dimensions by fractal fourier decimation. *Physical review letters*, 108(7) :074501, 2012. (Cited on page 21.)

[43] Samriddhi Sankar Ray. Thermalized solutions, statistical mechanics and turbulence : An overview of some recent results. *Pramana*, 84(3) :395–407, 2015. (Cited on page 22.)

[44] Victor Yakhot and Steven A Orszag. Renormalization group analysis of turbulence. i. basic theory. *Journal of scientific computing*, 1(1) :3–51, 1986. (Cited on page 22.)

[45] Paolo Giuliani, Mogens H. Jensen, and Victor Yakhot. Critical “dimension” in shell model turbulence. *Physical Review E*, 65(3) :036305, 2002. (Cited on page 22.)

[46] Evgenii Borisovich Gledzer. System of hydrodynamic type admitting two quadratic integrals of motion. In *Sov. Phys. Dokl.*, volume 18, pages 216–217, 1973. (Cited on page 22.)

[47] Michio Yamada and Koji Ohkitani. The inertial subrange and non-positive Lyapunov exponents in fully-developed turbulence. *Progress of Theoretical Physics*, 79(6) :1265–1268, 1988. (Cited on page 22.)

[48] Joseph Smagorinsky. General circulation experiments with the primitive equations : I. the basic experiment. *Monthly weather review*, 91(3) :99–164, 1963. (Cited on page 24.)

[49] Barrett Baldwin and Harvard Lomax. Thin-layer approximation and algebraic model for separated turbulent flows. In *16th aerospace sciences meeting*, page 257, 1978. (Cited on page 24.)

[50] Andrey Nikolaevich Kolmogoroff. The equations of turbulent motion in an incompressible fluid. *Izv. Akad. Nauk SSSR S*, 61 :1–2, 1942. (Cited on page 25.)

[51] Ludwig Prandtl. Über ein neues formelsystem fur die ausgebildete turbulenz. nach. ges. wiss. göttingen, math. *Phys. Kl*, pages 6–18, 1945. (Cited on page 25.)

[52] Tsan-Hsing Shih. Fundamentals in turbulence modeling. *Lecture series*, 9, 1999. (Cited on page 25.)

[53] Hendrik Tennekes, John Leask Lumley, Jonh L. Lumley, et al. *A first course in turbulence*. MIT press, 1972. (Cited on page 25.)

[54] Paul A. Durbin. Near-wall turbulence closure modeling without "damping functions". *Theoretical and Computational Fluid Dynamics*, 3(1) :1–13, 1991. (Cited on page 25.)

[55] Philippe Spalart and Steven Allmaras. A one-equation turbulence model for aerodynamic flows. In *30th aerospace sciences meeting and exhibit*, page 439, 1992. (Cited on page 25.)

[56] Charles G. Speziale. Analytical methods for the development of reynolds-stress closures in turbulence. *Annual review of fluid mechanics*, 23(1) :107–157, 1991. (Cited on page 25.)

[57] Kemal Hanjalić and Brian E. Launder. A Reynolds stress model of turbulence and its application to thin shear flows. *Journal of fluid Mechanics*, 52(4) :609–638, 1972. (Cited on pages 25 and 70.)

[58] Shuojun Li, David Montgomery, and Wesley B Jones. Two-dimensional turbulence with rigid circular walls. *Theoretical and computational fluid dynamics*, 9(3-4) :167–181, 1997. (Cited on pages 28, 36 and 65.)

[59] David Montgomery, Leaf Turner, and George Vahala. Three-dimensional magnetohydrodynamic turbulence in cylindrical geometry. *The Physics of Fluids*, 21(5) :757–764, 1978. (Cited on page 28.)

[60] Xiaowen Shan, David Montgomery, and Hudong Chen. Nonlinear magnetohydrodynamics by Galerkin-method computation. *Physical Review A*, 44(10) :6800, 1991. (Cited on page 28.)

[61] Subrahmanyan Chandrasekhar and Philip C. Kendall. On force-free magnetic fields. *The Astrophysical Journal*, 126 :457, 1957. (Cited on page 28.)

[62] Zensho Yoshida and Yoshikazu Giga. Remarks on spectra of operator rot. *Mathematische Zeitschrift*, 204(1) :235–245, 1990. (Cited on page 30.)

[63] Zensho Yoshida. Discrete eigenstates of plasmas described by the Chandrasekhar-Kendall functions. *Progress of theoretical physics*, 86(1) :45–55, 1991. (Cited on page 30.)

[64] Zensho Yoshida. Eigenfunction expansions associated with the curl derivatives in cylindrical geometries : completeness of Chandrasekhar–Kendall eigenfunctions. *Journal of mathematical physics*, 33(4) :1252–1256, 1992. (Cited on page 30.)

[65] Yukio Kaneda, Takashi Ishihara, Mitsuo Yokokawa, Ken'ichi Itakura, and Atsuya Uno. Energy dissipation rate and energy spectrum in high resolution direct numerical simulations of turbulence in a periodic box. *Physics of Fluids*, 15(2) :L21–L24, 2003. (Cited on pages 34 and 65.)

[66] Isabelle Raspo, Sandrine Hugues, Eric Serre, Anthony Randriamampianina, and Patrick Bontoux. A spectral projection method for the simulation of complex three-dimensional rotating flows. *Computers & fluids*, 31(4) :745–767, 2002. (Cited on pages 37, 38, 39 and 89.)

[67] Noele Peres, Sébastien Poncet, and Eric Serre. A 3D pseudospectral method for cylindrical coordinates. application to the simulations of rotating cavity flows. *Journal of Computational Physics*, 231(19) :6290–6305, 2012. (Cited on pages 37, 86 and 89.)

[68] Eric Serre and Patrick Bontoux. Vortex breakdown in a three-dimensional swirling flow. *Journal of fluid mechanics*, 459 :347–370, 2002. (Cited on page 39.)

[69] Lewis Fry Richardson. *Weather prediction by numerical process*. Cambridge University Press, 2007. (Cited on page 46.)

[70] Andrey Nikolaevich Kolmogorov. The local structure of turbulence in incompressible viscous fluid for very large Reynolds numbers. In *Dokl. Akad. Nauk SSSR*, volume 30, pages 299–303, 1941. (Cited on page 47.)

[71] A Brissaud, Uriel Frisch, Jacques Leorat, Marcel Lesieur, and Alain Mazure. Helicity cascades in fully developed isotropic turbulence. *The Physics of Fluids*, 16(8) :1366–1367, 1973. (Cited on pages 48 and 51.)

[72] Qiaoning Chen, Shiyi Chen, and Gregory L. Eyink. The joint cascade of energy and helicity in three-dimensional turbulence. *Physics of Fluids*, 15(2) :361–374, 2003. (Cited on pages 49 and 50.)

[73] Vadim Borue and Steven Alan Orszag. Spectra in helical three-dimensional homogeneous isotropic turbulence. *Physical Review E*, 55(6) :7005, 1997. (Cited on page 49.)

[74] Alexandros Alexakis. Helically decomposed turbulence. *Journal of Fluid Mechanics*, 812 :752–770, 2017. (Cited on pages 50 and 105.)

[75] Luca Biferale, Stefano Musacchio, and Federico Toschi. Inverse energy cascade in three-dimensional isotropic turbulence. *Physical review letters*, 108(16) :164501, 2012. (Cited on pages 50, 57 and 61.)

[76] Jean-François Pinton and Raúl Labbé. Correction to the taylor hypothesis in swirling flows. *Journal de Physique II*, 4(9) :1461–1468, 1994. (Cited on page 50.)

[77] Giovanni Zocchi, Patrick Tabeling, Jean Maurer, and Hervé Willaime. Measurement of the scaling of the dissipation at high Reynolds numbers. *Physical Review E*, 50(5) :3693, 1994. (Cited on page 50.)

[78] Sergey Nazarenko and J-P Laval. Non-local two-dimensional turbulence and Batchelor's regime for passive scalars. *Journal of Fluid Mechanics*, 408 :301–321, 2000. (Cited on page 51.)

[79] Pierre-Philippe Cortet, Severine Atis, Arnaud Chiffaudel, François Daviaud, Bérengère Dubrulle, and Florent Ravelet. Experimental study of the von Kármán flow from Re= 10^2 to 10^6 : spontaneous symmetry breaking and turbulent bifurcations. In *Advances in Turbulence XII*, pages 59–62. Springer, 2009. (Cited on page 53.)

[80] Alberto de la Torre and Javier Burguete. Slow dynamics in a turbulent von Kármán swirling flow. *Physical review letters*, 99(5) :054101, 2007. (Cited on page 54.)

[81] Osborne Reynolds. An experimental investigation of the circumstances which determine whether the motion of water shall be direct or sinuous, and of the law of resistance in parallel channels. *Philosophical Transactions of the Royal society of London*, (174) :935–982, 1883. (Cited on page 63.)

[82] Benjamin Favier, Céline Guervilly, and Edgar Knobloch. Subcritical turbulent condensate in rapidly rotating Rayleigh–Bénard convection. *Journal of Fluid Mechanics*, 864, 2019. (Cited on page 63.)

[83] Peter Alan Davidson. *Turbulence in rotating, stratified and electrically conducting fluids*. Cambridge University Press, 2013. (Cited on page 63.)

[84] Pierre Sagaut and Cambon Claude. *Homogeneous Turbulence Dynamics*. Cambridge University Press, 2008. (Cited on page 64.)

[85] Aurore Naso, Romain Monchaux, Pierre-Henri Chavanis, and Bérengère Dubrulle. Statistical mechanics of Beltrami flows in axisymmetric geometry : Theory reexamined. *Physical Review E*, 81(6) :066318, 2010. (Cited on pages 64 and 89.)

[86] Kamran Mohseni. Statistical equilibrium theory for axisymmetric flows : Kelvin's variational principle and an explanation for the vortex ring pinch-off process. *Phys. Fluids*, 13(7) :1924–1931, 2001. (Cited on page 68.)

[87] Chjan C. Lim. Coherent structures in an energy-enstrophy theory for axisymmetric flows. *Phys. Fluids*, 15(2) :478–487, 2003. (Cited on page 68.)

[88] Gertijan Jan F. van Heijst, Herman J.H. Clercx, and David Molenaar. The effects of solid boundaries on confined two-dimensional turbulence. *J. Fluid Mech.*, 554 :411, 2006. (Cited on page 68.)

[89] Brian E. Launder and Alan Morse. Numerical prediction of axisymmetric free shear flows with a Reynolds stress closure. In *Turbulent shear flows I*, pages 279–294. Springer, 1979. (Cited on page 70.)

[90] Carlos Rosales and Charles Meneveau. Linear forcing in numerical simulations of isotropic turbulence : Physical space implementations and convergence properties. *Physics of fluids*, 17(9) :095106, 2005. (Cited on page 76.)

[91] Thomas S. Lundgren. Linearly forced isotropic turbulence. *Annual Research Briefs-2003*, page 461, 2003. (Cited on page 76.)

[92] Eric Séverac and Eric Serre. A spectral vanishing viscosity for the LES of turbulent flows within rotating cavities. *Journal of Computational Physics*, 226(2) :1234–1255, 2007. (Cited on pages 77 and 86.)

[93] Olivier Czarny, Hector Iacovides, and Brian E. Launder. Precessing vortex structures in turbulent flow within rotor-stator disc cavities. *Flow, Turbulence and Combustion*, 69(1) :51–61, 2002. (Cited on page 77.)

[94] Tim Craft, Hector Iacovides, Brian E. Launder, and Athanasios Zacharos. Some swirling-flow challenges for turbulent CFD. *Flow, Turbulence and Combustion*, 80(4) :419–434, 2008. (Cited on page 77.)

[95] Julius Christian Rotta. Statistische theorie nichthomogener turbulenz. *Zeitschrift für Physik*, 129(6) :547–572, 1951. (Cited on page 81.)

dernière page de la thèse

AUTORISATION DE SOUTENANCE

Vu les dispositions de l'arrêté du 25 mai 2016,

Vu la demande du directeur de thèse

Monsieur W. BOS

et les rapports de

M. A. ALEXAKIS
Chargé de Recherche CNRS - Laboratoire de Physique - Ecole Normale Supérieure
24 rue Lhomond - 75005 Paris

et de

M. J-P. LAVAL
Directeur de Recherche CNRS - Laboratoire de Mécanique des Fluides de Lille
Kampé de Fériet, CNRS FRE 2017 - boulevard Paul Langevin - 59655 Villeneuve d'Ascq

Monsieur QIN Zecong

est autorisé à soutenir une thèse pour l'obtention du grade de **DOCTEUR**

Ecole doctorale MECANIQUE, ENERGETIQUE, GENIE CIVIL ET ACOUSTIQUE

Fait à Ecully, le 11 septembre 2019

P/Le directeur de l'E.C.L.
Le directeur des Etudes

ECOLE CENTRALE LYON
Service Scolarité
ECULLY

Grégory VIAL